LESION DETECTION IN MR MAMMOGRAPHY: NMITR MAPS, DYNAMIC AND MORPHOLOGICAL DESCRIPTORS

by

Gökhan Ertaş

B.S., in Electronics Engineering, Erciyes University, 1999
M.S., in Biomedical Engineering, Boğaziçi University, 2001

Submitted to the Institute of Biomedical Engineering
in partial fulfillment of the requirements
for the degree of
Doctor
of
Philosophy

Boğaziçi University
September 2007

LESION DETECTION IN MR MAMMOGRAPHY: NMITR MAPS, DYNAMIC AND MORPHOLOGICAL DESCRIPTORS

APPROVED BY:

Assoc. Prof. Dr. Halil Özcan Gülçür ……………………………
(Thesis Advisor)

Prof. Dr. Yekta Ülgen ……………………………

Prof. Dr. Mehtap Tunacı ……………………………

Prof. Dr. İrşadi Aksun ……………………………

Assoc. Prof. Dr. Albert Güveniş ……………………………

DATE OF APPROVAL: September 18, 2007

ACKNOWLEDGMENTS

This thesis is the result of four years of work during which I have been accompanied and supported by many people. It is now my great pleasure to take this opportunity to thank them. My sincerest thanks and appreciation goes to my supervisor Assoc. Prof. Dr. H. Özcan Gülçür. I thank him for his advice, invaluable time, input and mentorship which has made this study enjoyable and also a learning experience that, is unsurpassed by any means. My gratitude cannot be realistically expressed and extended in any form or words. Additional thanks for allowing me the opportunity to attend international conferences and inevitably see so many parts of the world through encouragement and financial support. I would like to thank Prof. Dr. Mehtap Tunacı, Istanbul University, Department of Radiology, for patiently giving me her time during extensive discussions and providing me with valuable comments and motivations. I am also indebted to Dr. Memduh Dursun, Istanbul University, Department of Radiology, for his extensive counseling and help during both collection and interpretation of breast MRI data. I would also like to thank to Asst.Prof.Dr. Onur Osman, Istanbul Commerce University, for giving me the inspiration to come up with new solutions to the technical problems during the processing of breast MR images. I would like to express my thanks to the members of the thesis committee, Prof. Dr. Yekta Ülgen, Assoc. Prof. Dr. Albert Güveniş and Prof. Dr. İrsadi Aksun for their careful reading and helpful suggestions on my thesis, for its being more comprehensive. I also thank to Research Foundation of Boğaziçi University for supporting the project 04X1043 during this PhD study.

One of the most important persons who has been with me in every moment of my PhD is my wife Gülay. I would like to thank her for the many sacrifices she has made to support me in undertaking my doctoral studies. By providing her steadfast support in hard times, she has once again shown the true affection and dedication she has always had towards me. I would also like to thank my son Sinan for his perpetual love that helped me in coming out of many frustrating moments during my PhD research.

ABSTRACT

LESION DETECTION IN MR MAMMOGRAPHY: NMITR MAPS, DYNAMIC AND MORPHOLOGICAL DESCRIPTORS

In this thesis, algorithms, methods and techniques for dynamic contrast-enhanced magnetic resonance mammography (DCE-MRM) have been investigated to maximize sensitivity, specificity and reproducibility of breast cancer diagnoses. A novel lesion localization method that uses cellular neural networks (CNNs) was developed. The breast region was segmented from pre-contrast images using four specifically designed CNNs. A 3D normalized maximum intensity-time ratio (nMITR) map of the segmented breast was generated using a moving mask of 3×3 voxels on the dynamic images. This map was converted into a binary form and processed with a fuzzy CNN consisting of three layers of 11×11 cells to segment out lesions from the surrounding tissues and to filter-out deceptive enhancements. A set of decision rules based on volume and 3D eccentricity of the suspicious regions were applied to minimize false-positive detections. The system was tested on a dataset consisting of 7020 MR mammograms in 1170 slices from 39 patients with 37 malignant and 39 benign mass lesions and was found to perform well with false-positive detections of 0.34/lesion, 0.10/slice and 0.67/case at a maximum detection sensitivity of 99%.

Enhancement and morphological descriptors of breast lesions derived from 3D nMITR maps were also studied for malignancy detection. The mean, the maximum value, the standard deviation and the entropy were the enhancement features found to have high significance ($P < 0.001$) and diagnostic accuracy (0.86-0.97). nMITR-entropy had the best performance. Among the morphological descriptors studied, 3D convexity, complexity and extent were found to have higher diagnostic accuracies (ranging between 0.70-0.81) and better performance than their 2D versions. Contact surface area ratio was found to be the most significant and accurate descriptor (75% sensitivity, 88% specificity, 89% PPV and 74% NPV).

The results demonstrate that nMITR maps inherently suppress enhancements due to normal parenchyma and blood vessels that surround lesions and have natural tolerance to small field homogeneities and thus are very effective for lesion localization and malignancy detection.

Keywords: Breast cancer, MR mammography, lesion localization, malignancy detection, normalized maximum intensity-time ratio, cellular neural network.

ÖZET

MR MAMOGRAFİDE LEZYON BELİRLENMESİ: NMITR HARİTALARI, DEVİNGEN VE BİÇİMSEL TANIMLAYICILAR

Bu tez çalışmasında, devingen zıtlığı-çoğaltılmış manyetik rezonans mamografi verilerini çözümleyelecek, tanı duyarlılığını, belirliliğini ve yinelenebilirliğini olabildiğince arttıran algoritmalar, yöntemler ve teknikler araştırılmıştır. Hücresel sinir ağı (HSA) yapıları kullanan çok özel bir lezyon saptama yöntemi geliştirmiştir. Özel tasarımlanmış dört HSA kullanılarak meme alanı kesimlendi. Elde edilen meme bölgesi için devingen görüntüler üzerinde kayan 3×3 voksel boyutlarında bir maske kullanılarak üç boyutlu normalleştirilmiş en fazla yoğunluk-zaman oranı haritası elde edildi. Bu harita ikili biçime dönüştürüldü ve 11×11'lik hücrelerden oluşan, üç katmanlı, bulanık bir HSA ile lezyonları çevreleyen dokulardan kesimlemek ve aldatıcı tutulumları elemek üzere işlendi. Yanlış pozitif saptamaları azaltmak için şüpheli bölgelerin hacim ve üç boyutlu dışmerkezlilik özelliklerinden çıkartılan bir dizi karar kuralları uygulandı. Sistem 39 hastaya ait, 37 kötü huylu ve 39 iyi huylu kütle lezyonu bulunan, 1170 adet kesitten oluşan, 7020 adet MR mammogram üzerinde test edildi ve en fazla %99 tanı duyarlılığında her bir lezyon için 0.34, kesit için 0.1 ve vaka için 0.67 yanlış pozitif saptama olmak üzere oldukça başarılı olduğu bulundu.

Üç boyutlu normalleştirilmiş en fazla yoğunluk-zaman oranı haritalarından elde edilen meme lezyonlarının morfolojik ve tutulum betimleyicilerinin kanserin saptanmasına yönelik değerliliği araştırıldı. Ortalama, en fazla değer, standart sapma ve dağınım tutulum özelliklerinin yüksek anlamlı ($P < 0.001$) ve tanım doğruluklu (0.86-0.97) olduğu bulundu. En fazla yoğunluk-zaman oranı dağınımı nicel tanı için en iyi başarıma sahip bulundu. Çalışılan morfolojik betimleyicilerden üç boyutlu dışbükeylik, normalize edilmiş karmaşıklık ve kaplam özelliklerinin tanı doğruluklarının (0.70 ila 0.81 arasında değişen) iki boyutlu uyarlamalarına göre daha yüksek performansa sahip olduğu saptandı. Dokunma yüzey alanı oranının, anlamı ve doğruluğu en yüksek olan özellik olduğu saptandı (tanı duyarlılığı %75, belirlliği %88, pozitif kestirim %89 ve negative kestirim %74).

Elde edilen sonuçlar, normalleştirilmiş en fazla yoğunluk-zaman oranı görüntülerinin doğal olarak lezyonları çevreleyen normal meme dokularını ve kan damarları tutulumlarını bastırdığı ve bu nedenle de lezyon saptamada ve kanser belirlemede çok etkin olduklarını göstermiştir.

Anahtar Sözcükler: Meme kanseri, MR mamografi, lezyon yerinin saptanması, habislik belirleme, normalleştirilmiş en büyük yoğunluk zaman oranı, hücresel sinir ağı.

TABLE OF CONTENTS

LIST OF FIGURES

LIST OF TABLES

LIST OF ABBREVIATIONS

AUC	Area under the ROC curve
BIRADS	Breast imaging reporting and data system
CAD	Computer-aided diagnosis
CNN	Cellular neural network
CNR	Contrast-to-noise ratio
DCE-MRM	Dynamic contrast-enhanced MR mammography
DICOM	Digital imaging and communications in medicine
DCIS	Ductal carcinoma in situ
DTPA	Diethylaminopentaacetic acid
Fat Sat	Fat saturation
FCM	Fuzzy c-means
FFDM	Full field digital mammography
FLASH	Fast low angle shot
FN	False-negative
FOV	Field of view
FP	False-positive
Gd	Gadolinium
GE	Gradient echo
LCIS	Lobular carcinoma in situ
MII	The maximum intensity image
MIP	The maximum intensity projection
MITR	The maximum intensity-time ratio
MR	Magnetic resonance
MRI	MR imaging

MRM	MR mammography
nMITR	Normalized maximum intensity time ratio
NIR	Near infrared
NPV	Negative predictive value
PPV	Positive predictive value
ROC	Receiver operating characteristic
ROI	Region of interest
SE	Spin echo
SNR	Signal to noise ratio
TIC	Time intensity curve
TN	True-negative
TP	True-positive
VOI	Volume of interest

LIST OF SYMBOLS

a	Extreme of the sloped portion of the membership function
a_v	Total area of the six faces of a voxel
A	Area of the lesion in representative slice
A_c	Contact surface area
$\mathbf{A}$	The feedback matrix of the CNN
$\mathbf{B}$	The control matrix of the CNN
B	Strength of main magnetic field
b	The bias of the CNN
B_s	Set of voxels of the breast region estimated by the CNN segmentation
B_r	Set of voxels delineated by the expert
c	Extreme of the sloped portion of the membership function
$C_{i,j}$	Cell located in the (i, j)-th position of a 2D image
$C_{i,j,k}$	Cell located in the (i, j,k)-th position of a 3D image
C_r	Set of voxels delineated by manual correction of the segmentation
C_s	Set of voxels within the breast region estimated by the CNN segmentation
C_{FP}	Cost of false-positive decision
C_{FN}	Cost of false-negative decision
C_{TN}	Cost of true-negative decision
C_{TP}	Cost of true-positive decision
CNN_E	2D binary morhological image erosion CNN
CNN_L	3D lesion detection CNN
CNN_O	2D binary morhological image closing CNN
CNN_R	2D binary morhological image reconstruction CNN

CNN_T	2D gray-level thresholding CNN
$Convexity^{3D}$	3D Convexity
$Convexity$	2D Convexity
$CSAR$	3D Contact surface area ratio
d_f	Distance between the greatest foci of the ellipsoid bounding the lesion
d_m	Major axis length of the ellipsoid bounding the lesion
DA	Diagnostic accuracy
e	Entropy of the nMITR
Ecc	3D Eccentricity
$Eccentricity$	2D Eccentricity
$Eccentricity^{3D}$	3D Eccentricity
$Extent^{3D}$	3D Extent
$Extent$	2D Extent
$E_{\Re}(i)$	Relative enhancement of the *i*–th post-contrast image within $\Re$
$f_{i,j,k}$	Indicator function
FP_{slice}	False-positive rate per slice
FP_{lesion}	False-positive rate per lesion
FP_{case}	False-positive rate per case
$FPVF$	False-positive volume fraction
$g = (g_i, g_j, g_k)$	Centroid of a lesion
I_{pre}	Pre-contrast image
$\tilde{I}_{pre}$	Normalized pre-contrast image
$I_{\Re}(0)$	Average intensity of the pre-contrast image within $\Re$
$I_{\Re}(\nu)$	Average intensity of the *v*–th post-contrast image within $\Re$

ISI	Initial signal increase
$J(Se,Sp)$	Optimality function
k	Kurtosis of the nMITR
$\max\{SE_{\Re}\}$	The maximum enhancement rate within an ROI
$\max\{E_{\Re}\}$	The maximum enhancement rate of an ROI
M	Image height
MCR	Misclassification rate
n	Number of voxels that composes a lesion
$n_{\Re}$	Total number of voxels within region $\Re$
$\overline{nComp_j}$	Average normalized complexity calculated over the slices in the j-th view
$nComplexity$	2D Normalized complexity
$nComplexity^{3D}$	3D Normalized complexity
$nMITR_{\Re}$	nMITR value of an ROI
N	Number of distinct nMITR values
N	Image width
$N_{i,j}$	r-neighborhood of the cell $C_{i,j}$
$N_{i,j,k}$	r-neighborhood of the cell $C_{i,j,k}$
NPV	Negative predictive value
$\boldsymbol{\eta}$	Normalized second order central moment matrix
μ	The mean value
$\mu_f(s,a,c)$	Spline-based membership function of normal tissues
$\mu_l(s,a,c)$	Spline-based membership function of a potential lesion
$\mu_{p_i p_j p_k}$	Central moment
O	Image depth

p	Perimeter of the lesion boundary in representative slice
p_i	Moment order in the i-th direction
$p(j)$	Probability of the j-th nMITR value
P	Expected prevalence of malignancy in the study dataset
$P(i,j,k)$	3D binary nMITR map
PPV	Positive predictive value
$\Pr(s)$	the probability of the occurrence of s
Pr_{Benign}	Probability of benign lesions in the study dataset
Pr_{Malign}	Probability of malignant lesions in the study dataset
PR	Segmentation precision
PSB	Post-initial signal behaviour
$Q(l,m,n)$	3D lesion detection template
$R(i,j,k)$	3D template matching result
$\Re$	Region of interest
r_x	Resolution of the imaging protocol in the x direction
r_y	Resolution of the imaging protocol in the y direction
r_z	Resolution of the imaging protocol in the z direction
RO	Relative overlap
s	Skewness of the nMITR
$S(i,j,k)$	3D nMITR map
sd	Standard deviation of the nMITR
$SE_{\Re}(v)$	Enhancement rate of the ROI at v-th time point
Se	Sensitivity
Sp	Specificity

$\hat{T}$	The optimal threshold value
$T_{\max}$	Time point when $\max\{SE_{\Re}\}$ is reached
T_1	Spin-lattice relaxation time
T_2	Spin-spin relaxation time
TE	Echo time
TH	Threshold
TR	Repetition time
$TPVF$	True-positive volume fraction
$\mathbf{u(t)}$	The input matrix of the CNN
V_L	Lesion volume
V_{CH}	Convex hull volume
V_{BB}	Volume of box bounding the lesion
w_j	Weight of the j-th view
$\mathbf{x(t)}$	The state matrix of the CNN
$\mathbf{y(t)}$	The output matrix of the CNN

1. INTRODUCTION

1.1 Breast Cancer

Breast cancer is the most commonly diagnosed and the second leading cause of cancer death among women after lung cancer. The chance of a women having invasive breast cancer at some time during her life is about 1 in 8. A number of factors have been identified that increase breast cancer risk. These include age at menarche, age at the first full-term pregnancy, age at menopause, presence or history of benign breast disease, positive family history of a first-degree relative with breast cancer, certain mutations in the BRCA1 or BRCA2 genes, use of hormone replacement therapy, ionizing radiation to the breast (particularly early in life), substantial alcohol consumption, and obesity or a higher body mass index [1, 2].

Precise imaging techniques are vital for early detection of cancer and localization of the suspicious lesions for biopsy. Although X-ray mammography is the conventional screening tool used to detect breast cancer in its early stages, Magnetic Resonance Mammography (MRM) is gaining increased acceptance as an adjunct tool in breast evaluations. Among the currently available breast imaging techniques such as X-ray mammography, high frequency breast ultrasound, positron emission tomography and scintimammography, MR mammography offers the highest sensitivity for invasive breast cancer [3]. An important advantage of MRM, beside absence of ionizing radiation is that lesion-obscuring overlapping structures and summation shadows are much less pronounced in comparison with X-ray mammography. This is because MRM does not require excessive breast compression during imaging. Moreover, with the help of contrast agents that reveal the state of angiogenesis, dynamic contrast enhanced MR mammography (DCE-MRM) provides important tissue information on cross-sectional morphology, as well as functional information on perfusion and capillary leakage and thus makes possible localization, visualization and assessments of the aggressiveness and multifocality of the breast lesions.

In order to accurately assess breast cancer with DCE-MRM, a large volume of image data acquired at high spatial and temporal resolutions must be analyzed. T_2-weighted images, pre and post-contrast T_1-weighted images and subtraction images created from the dynamic data must all be inspected by the radiologist slice by slice to localize lesions. This is a tedious and time consuming task, as suspected regions can be very small and there may be several deceptively enhanced healthy regions that need careful discrimination, such as blood vessels and normal parenchyma especially in case of premenopausal women. Once a lesion is localized, the radiologist must carefully evaluate its morphology and/or enhancement dynamics to detect malignancy. The major motivation behind this is the fact that typically, irregular morphology, irregular or spiculated margins, heterogeneous internal enhancements and rim enhancements are signs of malignancy, while smooth margins and homogenous internal enhancements are associated with benign lesions. Malignant lesions are characterized by faster and stronger enhancements than benign lesions, although some malignant lesions may produce enhancement only slowly or minimally, and a variety of benign lesions may produce enhancement rapidly with marked signal increase. These assessments are highly time-intensive, experience and observer dependent, especially when lesion volumes are considered. In the standard clinical practice, due to the enormous image data that must be processed and interpreted, a typical (manual) patient evaluation requires constant and diligent attention for periods exceeding 30 minutes. Clearly there is a great need for systems that automatically extract important diagnostic features of the image data and present them to the radiologists for decision support.

1.1.1 Lesion Localization

As stated previously, a major task in DCE-MRM interpretations is the discrimination of deceptively enhancing regions and the localization of lesions. Recently, computerized systems have been developed that provide color-coded parametric maps of enhancements to make visualization of suspiciously enhancing regions uncomplicated and to facilitate overall analysis [4, 5, 6, 7]. Since these systems rely on manual identification of lesions, they are still time-consuming, highly subjective and error-prone. Clearly, there is a great need for automated estimation of lesion volumes for assisting radiologists in their clinical breast evaluations. A number of computerized techniques have been developed for use in diagnostic breast imaging, such as for X-ray mammography [8, 9], sonography [10], tomosynthesis [11] and computed tomography [12]. To our knowledge, only Bian et al [13] reported a fully automated lesion localization technique for DCE-MRM. A more detailed literature survey concerning lesion localization is presented in Sections 4.1 and 5.1.

1.1.2 Malignancy Detection

Another major task in DCE-MRM interpretations is the detection of malignancy of the breast lesions based on their morphology and/or enhancement dynamics. The major motivation behind this is the fact that typically, irregular morphology, irregular or spiculated margins, heterogeneous internal enhancements and rim enhancements are signs of malignancy, while smooth margins and homogenous internal enhancements are associated with benign lesions [14]. During the past decade, the diagnostic significance of lesion morphology and qualitatively assessed morphological parameters have been studied [15, 16, 17]. These assessments are all highly time-intensive, experience and observer dependent, especially when lesion volumes are considered. Automated methods have been developed to automatically extract diagnostically useful information using delayed fat suppressed post-contrast images or subtraction images that are helpful to suppress less enhancing normal parenchyma that surround the lesions and to highlight avidly enhancing regions [18, 19, 20, 21].

For detection of malignancy, since there is an overlap between enhancement dynamics of benign and malignant lesion, additional diagnostic information is preferably obtained by tracking the progress of the time-intensity curves for manually positioned small 2D region of interests (ROIs) [22, 23, 24]. Utmost care is a must during the positioning of the ROI, since missing of a very small detail may result in poor specificity and sensitivity in the final diagnosis. In general, it is advantageous to place a region of interest over the early enhancing component of a lesion. If a larger ROI is used, necrotic components of the lesion may undesirably affect the evaluations. To make accurate decisions, familiarity with the TICs of malignant and benign lesions is also necessary. Automated enhancement analysis methods make use of a number of protocols and quantitative interpretation criteria such as maximum signal enhancement rates at specific times, time to maximum enhancement, wash-out ratio and maximum intensity-time ratio to improve diagnosis. [25-35].

Although the automated stated above make some improvements in lesion diagnosis, they require a great deal of experience to achieve reproducible results. In case enhancement curves and morphologies of benign and malignant lesions are visually similar, the performance of these methods is still poor and for better characterization, whole volumes of the localized lesions must be analyzed systematically. A more detailed survey on available malignancy detection methods is given in Sections 6.1 and 7.1.

1.1.3 Computer Assistance: Currently Available Software

Undoubtedly, there is a great need for software packages that facilitate extraction of important diagnostic features of the DCE-MRM image data and present them to the radiologist for decision support. A pioneering work toward this goal was carried out by Leach et al, who developed MRIW, a software to quantify contrast agent uptake in dynamic contrast-enhanced MR images [6]. In a recent software, reported by Subramanian et al. [36], the user is interactively allowed to specify a TIC that represents malignancy. MTDYNA (Mevis Inc, Bremen, Germany) and CADstream (Confirma Inc, Kirkland, WA) generate color parametric maps of relative changes in intensity of each pixel over time to identify areas of significant enhancement and supply details about regions that show significant enhancement. Although they provide considerable assistance to the radiologists, all of the above mentioned software packages also have serious limitations. A more detailed survey on available software packages is given in Section 8.1.

1.2 Rationale and Objectives

The major goal of this thesis is to investigate algorithms, methods and techniques to analyze DCE-MRM data that could be used to develop a standardized, reliable, efficient and accurate decision support system that minimizes processing time, minimizes the need for user intervention and experience, minimizes false-positive detections, miss-detections, intra- and inter-observer variability and maximizes detection sensitivity and reproducibility of the diagnoses. To achieve this goal, it is vital to develop an efficient lesion segmentation method to segment out the lesion from the surrounding tissues and to filter-out deceptive enhancements from normal parenchyma, due to blood vessels, fat etc., or due to field inhomogeneities. This step determines the accuracy of lesion localization and size measurement for staging purposes, and is also important for proper delineation of the lesion for malignancy detection. Development of quantitative methods to facilitate lesion localization and to improve malignancy detection and a software package that provides decision support based features extracted from simultaneous dynamic and morphologic measurements for clinical practice are also aimed.

1.3 Test Datasets

The algorithms, methods and techniques developed in this thesis have been tested using datasets prepared in cooperation with the Radiology Department of Istanbul University. The breast MR examinations were performed at the 1.5 Tesla scanner (Magnetom Symphony; Siemens Medical Systems, Erlangen, Germany) of this department. The scanner equipped with a gradient system having a maximum amplitude of 30 mT/m. A dedicated four-element phased-array receiver breast coil was used. Patients were positioned prone with the breast to be imaged in gentle compression within the coil to minimize motion artifacts. The nature of the imaging procedure was explained to all the patients and their consents were secured. A variant of spoiled gradient-echo imaging, T_1-weighted 3D fast low angle shot (FLASH, TR/TE 9.80/4.76 msec, flip angle 25^{o}, slice thickness 2.5 mm with no gap, 512×512 matrix, and 0.625×0.625 mm^2 imaging sequence was used. During and immediately after the bolus injection of contrast agent Gd-DTPA (0.1 mmol/kg body weight), one pre-contrast and five post-contrast high-resolution bilateral axial images were acquired per slice with a temporal resolution of approximately 88 seconds. Several breast lesions such as fibroadenomas, adenosis, mastitis, infected cysts and other benign changes, invasive carcinomas, ductal carcinoma in situ were studied. All cases were proved either by histopathological examination or by clinical follow-up. Dynamic 12-bit grayscale image sets were transferred from the MR scanner to a personnel computer in DICOM format for further analysis. nMITR maps were generated from the enhancement data and analyzed to extract important features, to automate lesion localization and to improve accuracy and reproducibility of malignancy detection.

1.4 Overview of the Thesis

The motivation, rationale and the objectives of the thesis are given in this introduction. Background information concerning breast physiology, breast diseases, benign and malignant changes, and breast cancer risk factors and a brief summary of currently available diagnostic breast imaging modalities is also presented are presented in Chapter 2. Fundamentals of dynamic contrast enhanced magnetic resonance mammography (DCE-MRM); hardware, contrast agents, imaging sequences, resolution considerations, lesion interpretation criteria, enhancement dynamics, multifactorial interpretation, computer assistance and quantitative methods are discussed in Chapter 3. Chapter 4 is on breast segmentation and lesion detection with cellular neural networks and 3D template matching. In this chapter, a fully automated 3D lesion detection system for bilateral, axial DCE-MR mammograms is introduced that does not require prior knowledge concerning breast anatomy such as chest wall flatness, prior mastectomy history. Extraction of the breast regions by a segmentation scheme based on cellular neural networks, lesion detection with a 3D template and the performance of the segmentation are discussed. Chapter 5 presents a novel computerized lesion localization technique for MR mammography based on 3D nMITR maps, multilayer cellular neural networks and fuzzy c-partitioning. Minimization of false-positive detections and a performance analysis are also given in this chapter.

In Chapter 6, a novel, fast volumetric lesion segmentation method that requires user interaction only during initialization is described that is based on the use of a small sampling mask that is moved through the entire volume of interest, voxel by voxel to obtain accurately samples, enhancement characteristics and an nMITR map of the tissues involved. Diagnostic relevance of statistical parameters extracted from the generated nMITR map is studied in detail. Chapter 7 is on malignancy assessment based on nMITR maps and morphological descriptors; 2D and 3D descriptors such as convexity, normalized complexity, extent and eccentricity and enclosed area to contact surface area ratio are discussed in this chapter. An interactive dynamic analysis and decision support software, *DynaMammoAnalyst,* for MR mammography is presented in Chapter 8. Chapter 9 gives general conclusions and recommendations for future work.

2. BACKGROUND

2.1 Introduction

Breast cancer is the most commonly diagnosed cancer and the second leading cause of cancer death among women. The only way today to find out for sure if a breast lump or abnormal tissue is cancer is by having a biopsy. A suspicious tissue is removed by a surgical excision or needle biopsy and is examined under a microscope by a pathologist who makes the diagnoses. Imaging techniques of the breast are therefore vital since they will allow early detection of cancer and localization of the suspicious lesion in the breast for a biopsy procedure.

To develop and improve breast cancer detection and consider imaging modalities, the physiology of the breast, risk factors, breast diseases and the way in which tumor development occurs should first be considered.

2.2 Breast Physiology

The breast (mammary gland) consists of 15 to 20 lobes with varying number of ducts and lobules (Figure 2.1). These structures are surrounded by collagenous connective tissue. A lobule contains approximately 30 terminal branches that form the parencyhmal part of the lobule. All terminal ducts open into a lactiferous duct that runs toward the nipple. The 15 to 20 main lactiferous ducts open in the nipple. The body of the gland is embedded in fatty tissue. It is supplied by a network of blood and lymph vessels and is supported in the subcutaneous fatty tissue by connective-tissue structures known as Cooper ligaments. These ligaments arise from the stromal tissue of the body of the gland and insert into the prepectoral fascia and the skin. The body of the gland, which can vary greatly in form, size and composition, converges toward the nipple, is generally symmetrical.

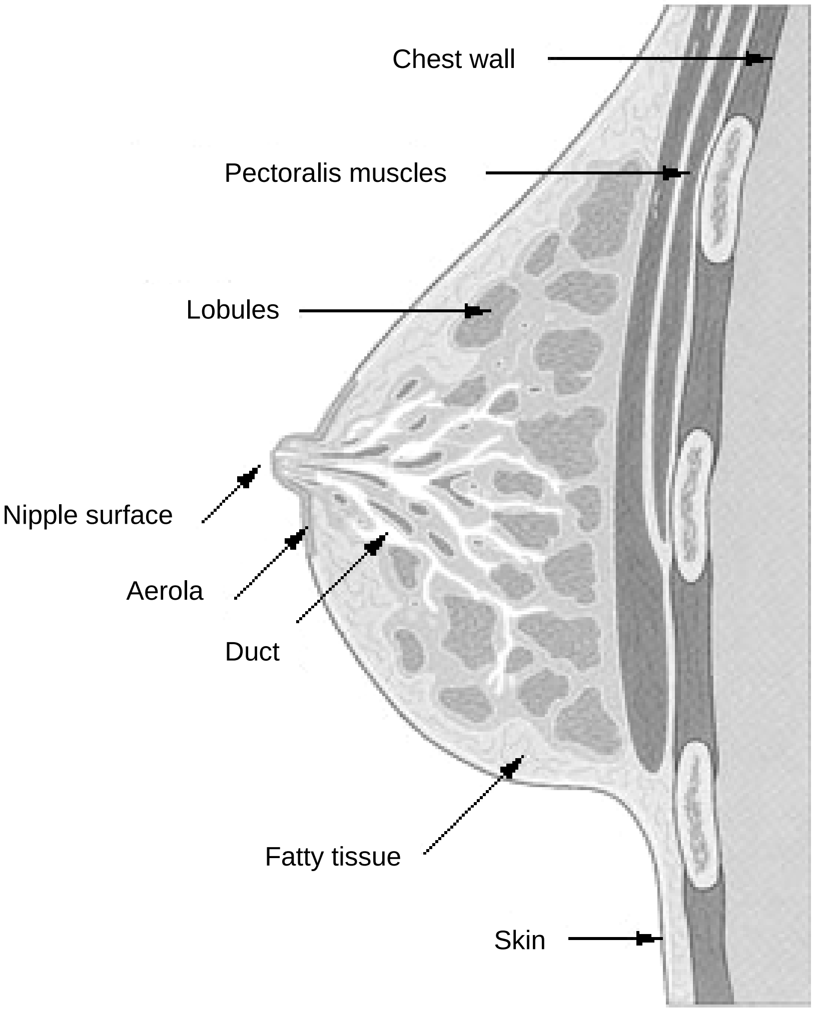

Figure 2.1 Schematic diagram of mammary gland [37].

The breast is affected by physiologic changes in morphology and function throughout life from menarche to menopause, and during each menstrual cycle. These changes are based on hormonal activity, mainly by prolactin, estrogen and progesterone. At menarche, the main events include development and growth of ductal and lobular units. At pregnancy, a remarkable rise of hormone levels induces growth and secretory activity of the breast. Postmenopausally, the breast undergoes involution characterized by atrophy of the parenchymal structures. The breast tissue is dense and parenchyma is rich in a young woman, with age, the fat content of the breast tissue increases as the woman ages [38].

2.3 Common Breast Diseases

2.3.1 Benign Changes

Most benign lesions can actually be regarded as aberrations of normal processes. It has been stated that “the borderline between a normal change and a disease should be more defined in relation to their clinical aspects than to histologic findings” [39].

Fibrocystic Change

Fibrocystic changes are related to regular and sometimes irregular, menstrual cycles with hormonal fluctuations. This disease is one of the most common benign conditions that affect more than 50 percent of women having palpably irregular breasts, cyclic pain, and tenderness. The mammary tissue, in response to the imbalanced estrogen and progesterone stimulation over time, undergoes a wide variety of morphologic changes. Changes occur in the ducts (cyst and ductal hyperplasia formation), lobules (adenosis -lobular hyperplasia- and sclerosing adenosis) and the stroma (fibrosis).

Cysts

Cysts usually occur in the terminal ductal lobular units associated with fibrocystic changes. They are locally distended peripherial ductal segments filled with fluid. Approximately half of all women 30 to 40 years and up develop fibrocystic changes in the breast that manifest themselves in single or multiple cysts of varying sizes. While simple cysts are always benign, complicated cysts can sometimes harbour malignancy. They become clinically important when the patient presents with pain or when a palpable findings require further diagnostic studies.

Ductal Hyperplasia

Ductal hyperplasia refers to epithelial proliferation in tissue with fibrocystic changes in the ductal system. It does not usually present as a palpable tumor. Monoclonal neoplastic proliferation within ducts already occupied by ordinary hyperplasia is termed as atypical ductal hyperplasia. It is close to ductal carcinoma in situ, but does not fulfill all the criteria. However, in the later stages, ductal carcinoma in situ and then invasive ductal cancer can occur as illustrated in Figure 2.2.

Adenosis

Adenosis refers to a spectrum of changes within the lobules beginning from the hyperplasia to the subsequent fibrosis and calcifications and can present as a mass.

Fibrosis

Fibrosis is an increase of fibrous connective tissue. The lobules in particular are reduced in number and in size. Focal fibrosis may present as a palpable mass.

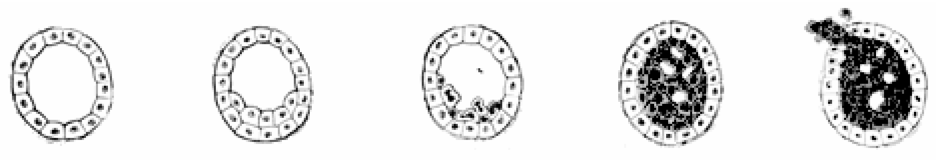

(a) (b) (c) (d) (e)

Figure 2.2 (a) Normal duct, (b) ductal hyperplasia, (c) ductal hyperplasia with atypia, (d) ductal carcinoma in situ, (e) invasive ductal cancer [40].

Benign Papillary Neoplasm and Changes

Intraductal Papilloma

Intraductal papilloma usually occurs within a major duct in the subareolar region with bloody or serous nipple discharges. They are characterized by small, usually less than 1-2 cm in size lesions. Papillomas associated with hemorrhage and cystic change may be larger than 4 cm. There may be multiple peripheral papillomas that involve groups of ducts. These are associated with an increased risk for local recurrence and subsequent development of breast carcinoma.

Radial Scar

Benign ductal hyperplasia, intraductal papilloma and/or sclerosing adenosis causes distortion of the ducts and ductules arranged in a radiating pattern referring to radial scar. Therefore radial scars are speculated masses or areas of architectural distortion, often with multiple long spicules and central areas of lucency.

Fibroepithelial Tumors

Fibroadenoma

Fibroadenomas consist of epithelial and fibrous tissues that surround branching and budding ducts. They are smooth, rubbery or hard lumps that move easily within the breast tissue. They are the most common solid benign breast tumors seen in women under the age of 35 years. Most fibroadenomas are 2-3 cm in size, but may reach to 6-7 cm. Very rarely ductal or lobular carcinoma in situ occurs within fibroadenomas. Invasive carcinoma has also been reported to arise in a fibroadenoma [41]. Thus, it is important to evaluate the surrounding tissue of fibroadenoma to determine the extent of disease for optimal treatment.

Phyllodes Tumor

Phyllodes tumor is the malignant equivalent of fibroadenoma in which the epithelial elements are benign, but the fibrous tissue is malignant. It varies in size from 1 cm to greater than 15 cm and occurs in about 1% of patients who have fibroadenoma for several years.

Benign and Malignant Epithelial and Nonepithelial Tumors

Hamartoma

Variable amounts of fat, glandular tissue and fibrous connective tissue may compose hamartoma, which is a circumscribed benign nodule.

2.3.2 Malignant Changes

Most malignant breast diseases originate in the ductal lobular units. These units are composed of the terminal duct and the lobules branching from them and are liable to disturbances in the complex processes of cell proliferation and differentiation. In the pre-invasive stage, the malignancy is confined within the ducts and lobules and the basement membrane is intact or only focally discontinuous. Conversion to invasive form is associated with stromal invasion.

Ductal Carcinoma in Situ (DCIS)

Ductal carcinoma in situ is a condition in which the cells lining the ducts are cancerous, but stay contained within the ducts without growing through into the surrounding breast tissue. It accounts for 3–5% of palpable breast lesions and usually presented as microcalcifications; the solid type may or may not be associated with calcifications. A variant is lobular carcinoma in situ (LCIS) which is a precursor lesion for invasive lobular carcinoma, but in most cases, it does not progress to the invasive stage. It is regarded as a marker of increased risk of either lobular or ductal carcinoma. It is always an incidental finding that does not form a palpable tumor or a specific mammographic finding.

Invasive Carcinoma

Invasive breast carcinoma differs from ductal carcinoma in situ by the presence of stromal invasion, through which tumor cells spread not only locally but also regionally and distantly via vascular lymphatic space. Tumor size is closely related to lymph node metastasis and prognosis. Seventy to 80% of all breast cancers are invasive ductal carcinoma. Approximately 15% of invasive carcinomas are lobular. Lobular carcinoma infiltrates in a diffuse manner without altering the surrounding tissue, which often leads to discrepancy between imaging findings and histologic tumor size. The remaining 5% are infiltrating lobular carcinomas such as papillary [64].

2.4 Stages in Lesion Growth

Originally, most solid tumors present as vascular tumor cell aggregates, which get nutrients by simple diffusion. This is called the prevascular phase and can last for up to several years. Growth beyond a tumor size of 1–2 mm requires formation of new micro vessels. During this process, the epithelial cells release so-called angiogenic factors that interact with endothelium of the surrounding capillaries. These newly formed endothelial cells arrange into loops and canalize to form new vessels. The new vessels may also originate from the host tissue, when the venules incorporate into the tumor. This is the beginning of the vascular phase of the tumor. In addition to tumor growth, angiogenesis is also necessary for metastatic spread in which tumor cells enter the vascular structures, spread within them to the target organs, implant and grow. This complex process involves numerous angiogenic factors such as vascular permeability factor, vascular endothelial growth factor and basic fibroblast growth factor. Therefore, the vessel architecture in malignant tumors is characterized by caliber fluctuations, irregular course, formation of sinusoids and arteriovenous shunts.

2.5 Breast Cancer Risk Factors

Factors that increase breast cancer risk include younger age at menarche, older age at first full-term pregnancy, older age at menopause, presence or history of benign breast disease, positive family history of a first-degree relative with breast cancer, certain mutations in the BRCA1 or BRCA2 genes, use of hormone replacement therapy, ionizing radiation to the breast (particularly early in life), substantial alcohol consumption, and obesity or a higher body mass index [1, 2].

2.6 Breast Imaging Techniques

It is important to detect and localize suspicious lesions early in their development stages and if malignancy is suspected, to perform biopsy. Various imaging techniques are in use for detecting and localizing breast abnormalities and for detection of malignancy. In breast examinations, the term “screening mammography” is used for imaging techniques employed for detecting abnormalities in the general population and the term "diagnostic mammography" used for imaging techniques used for localization of lesions and detection of malignancy. Importance of screening has been shown in a number of studies [42, 43, 44]. Various breast-imaging modalities are discussed below.

2.6.1 Conventional X-Ray Mammography

Due to its high sensitivity and cost-effectiveness, conventional X-Ray mammography has been the established technique for breast examinations; both for diagnostic and screening purposes. However, X-ray mammography has a number of disadvantages. It lacks contrast, its sensitivity is decreased in radiologically dense breasts, and differentiation between malignant and benign lesions is difficult and X-ray radiations are known to cause damage to the DNA of cells. It has been shown that the use of X-Ray mammography as the sole tool for breast examinations results in as much as 70% unnecessary biopsies and false-negative rates that may be as high as 34% [45, 46]. Recently, X-Ray mammography is challenged by other imaging modalities.

2.6.2 Digital X-Ray Imaging

Full field digital mammography provides high resolution, high contrast images with the lowest possible radiation dose to the patient. Recently, a technique known as *single energy X-Ray technique* or as *diffraction-enhanced imaging* is being developed where a single energy X-ray source is used to create significantly sharper, more detailed pictures of breast tissue. Another experimental technique under development is known as *tomosynthesis*. In this method, multiple images are acquired as the X-ray tube is moved in an arc above the stationary breast and digital detector. The total radiation dose required for imaging the entire breast is less than the dose used for a single film screen mammography. Tomosynthesis has the potential to improve the specificity of mammography by reducing the contribution of normal fibroglandular breast that mask presence of a lesion. This technique is claimed to be particularly advantageous for women with radiologically dense breasts. All these techniques have limitations similar to conventional X-ray Mammography especially during the diagnosis of detected lesions.

2.6.3 Ultrasound Imaging

Ultrasound is the most important adjunctive imaging modality. Its excellent accuracy in the diagnosis of cysts reduces the number of unnecessary biopsies. It can provide important information to confirm the presence of palpable carcinomas in radiodense tissue. The accuracy in detecting malignant process depends both on the surrounding tissue and on the lesion itself. Accuracy is limited for small carcinomas and in particular preinvasive carcinoma. For this reason, ultrasound should never be used to role out a malignant process without corresponding mammographic studies. Benign findings in the presence of mammographic or clinical signs of a suspected malignant process do not exclude malignancy [47]. In view of these restrictions, the known examiner-dependent accuracy and it high physician time requirements, ultrasound is also not a suitable modality.

2.6.4 Nuclear Imaging

Cancerous cells take up more glucose when compared with healthy cells. Hence, it is possible to trace cells that are over-active and consume excessive glucose using dedicated radioactive tracers. To detect breast tumors, nuclear imaging with 99mTc-Sestamibi as the tracer is generally used. Another imaging method for detecting breast tumors is positron emission tomography in which fluorodeoxyglucose is the tracer commonly used. Unfortunately, the signal-to-noise ratio in both of these imaging modalities is not sufficient enough to diagnose small tumors. Moreover, the instrumentations are expensive; therefore these techniques are currently used only in a few selected cases [48, 49].

2.6.5 Electical Impedance Imaging

Changes in cellular water content and cell membrane properties cause a significant change in tissue complex electrical impedance. This makes possible to visualize cancerous and pre-cancerous lesions by electrical impedance measurements. Such a system could be particularly effective in detecting breast tumors of women who have dense breast tissue and therefore are difficult to examine using conventional X-ray mammography. At present, this method is not suitable for use in clinical breast examinations [50, 51].

2.6.6 Optical Diffusion Imaging

Recently, there are increased interests in imaging systems that use light. Near infrared (NIR) is particularly attractive because it allows non-invasive probing of tissue oxygenation and metabolism. Tissue has a low absorbing window in the NIR and allows light penetration for several centimeters. The information obtained depends on the attenuation characteristics of the breast tissues and can be used to detect malignancy. Main advantages of these systems are the absence of ionizing radiation and the relatively low cost of instrumentation. These systems have not yet been developed enough for identifying small lesions and lesions situated deep in the breast parenchyma and cannot be used clinically.

2.6.7 Magnetic Resonance Imaging

Unlike mammography that uses low dose X-rays to image the breast, magnetic resonance imaging (MRI) uses powerful magnetic fields and radio waves to create images of the breast. The MRI system is able to switch magnetic fields and radio waves to achieve views in any plane and from any orientation while X-ray mammography requires re-orientation of the breast and mammography system for each view desired.

In the beginning of breast MRI, the use of spin-echo (SE) sequences were the only choice. They revealed good tissue contrast enabling good measurements of T_1 (spin-lattice relaxation time), T_2 (spin-spin relaxation time) and proton density values, but the low spatial and temporal resolution was a problem. Turbo spin-echo sequences were developed to shorten acquisition times. Because of hyper-intensity of the fat signal and insufficient diagnostic information provided, this type of sequences have found limited applications and have been only used with T_2-weighting in distinguishing liquid from solid content lesions [52].

Experimentation with SE sequences showed that malignant breast lesions have higher T_1 and T_2 values than normal breast tissues, but shorter T_1 and T_2 values than some benign breast lesions at 1.5 Tesla as listed in Table 2.1. The overlap in T_1 and T_2 values between benign and malignant breast lesions, sensitivity and specificity of the spin-echo sequences were not adequate for detection and diagnosis of malignancies until the development of dynamic contrast enhanced MR mammography (DCE-MRM) [54]. DCE-MRM is discussed in more detail in the next chapter.

Table 2.1
T_1 and T_2 values of the breast tissue at 1.5 Tesla [53].

Tissue	N samples	Mean T_1 ± Std.Dev.	Mean T_2 ± Std.Dev.
Fat	28	265 ± 2	58 ± 1
Normal Breast Tissue	23	796 ± 21	63 ± 4
Malignant Lesions	11	876 ± 29	75 ± 4
Benign Lesions	17	1049 ± 40	89 ± 8

3. FUNDAMENTALS OF DYNAMIC CONTRAST ENHANCED MR MAMMOGRAPHY

3.1 Introduction

For over 20 years, dynamic contrast-enhanced MR Mammogpraphy (DCE-MRM), or breast MRI, has been investigated as a method for breast cancer detection and diagnosis [55, 56, 57, 58, 59, 60, 61]. The technique consists of injecting a contrast-enhancing dye like material into the patient blood stream and using magnetic resonance imaging to monitor the way in which this material is taken up and cleared out by the tumor tissue. The ability to identify a mass in the breast requires that the mass have a different appearance (or a different contrast) from normal tissue. With DCE-MRM, the contrast between soft breast tissues is 10 to 100 times greater than that obtained with X-rays.

A typical exam consists of a series of 2 to 6 sequences, with each sequence lasting between 2 - 15 minutes. An “MRI sequence” is an acquisition of data that yields a specific image orientation and a specific type of image appearance or “contrast.” Indications of the imaging technique include differential diagnosis and characterization of lesions, detection of extent of carcinoma, mammographically dense breasts, evaluation of inflating carcinoma, post radiation complications and accepted as a gold standard in the pre-operative evaluation of multicentric and contralateral breast carcinomas [62, 63].

Studies among asymptomatic high-risk women report sensitivities to breast cancer between 71% and 100%. Reported specificities, however, have varied widely (37-99%) depending on techniques and criteria for cancer detection. In addition to these, it is not recommended for evaluating the dense breast of young patients (below the age of 35) in the absence of a significantly increased risk of malignancy, differentiation of microcalcifications, excluding malignancy in breast with signs of inflammation [64].

(a) (b)

Figure 3.1 (a) Bilateral breast coil, (b) position of a patient prone on the breast coil before placing in the magnet bore [67].

3.2 Technical Perspectives

3.2.1 Hardware

MR Mammography can be performed using any tomography equipment used for whole-body imaging. Usual field strengths are 0.5–1.5 Tesla. High-performance gradient coils with a minimum ascent velocity of 15 mT/m and dedicated surface coils permitting signal-to-noise ratio optimization and reducing slice thickness to < 3 mm are two fundamental requirements [65].

Since different coil designs results in different capabilities, care must be taken to choose the proper coil for the desired results [66]. A bilateral breast coil manufactured by Siemens is presented in Figure 3.1a. The patient is placed directly on the table (a) and the technologist has visual control of breast position through a transparent window as illustrated in Figure 3.1b.

It is important that the breasts are correctly placed within the coils, well centered and cushioned or slightly compressed, to diminish movement during the image acquisition. Compression should not be too marked, as it will distort the normal breast configuration, making the correct description of lesion localization and the comparison to other methods difficult. It is important that the patient is comfortable, with breast well positioned in the coil. This way the patient will be able to keep the same exact position, without any movement during the whole examination and the motion artifacts will be reduced.

3.2.2 Paramagnetic Contrast Agents

Although Gadolinium (Gd^{3+}) is the most frequently used paramagnetic contrast medium, it cannot be used as contrast medium in its free form because of its toxicity and tendency to form salts with few relaxation properties. Therefore, it is bound to a chelating molecule to obtain a non-toxic substance with better bio-distribution and solubility in water. Currently, there are four chelates authorized by the Federal Drug Administration in the USA. These are Gd–DTPA (Magnevist, Schering), Gd–DOTA (Dotarem, Guerbert) for ionic contrast media, Gd–HP-DO3A (Prohance, Bracco) and Gd–DTPA–BMA (Omniscan, Nycomed) for non-ionic contrast media. Among them, because of its inability to penetrate the cell membrane and its rapid spread in the vascular system exclusively in the extracellular compartment, Gd–DTPA is the most popular contrast agent for DCE-MRM and is injected to patients at various doses (0.1–0.2 mmol/kg). Its plasma half-life is about 90 min and it is excreted unaltered through the renal system without being metabolized [68]. The effect for various breast tissues is calculated by modifying the tissue relaxation time T_1 using Eq. 3.1 [69].

$$\frac{1}{T_1(c)} = \frac{1}{T_1(0)} + nX_1C \tag{3.1}$$

where $T_1(0)$ is baseline (i.e. precontrast) relaxation time, X_1 is relaxivity of Gd-DTPA for a given filed strength, C and n describe the molar concentration of the tissue compartment and the fraction of tissue volume accessible to contrast agent molecules respectively. The relaxivities of X_1 of Gd-DTPA are equal to 3.5 3.57 and 4.06 $(\text{mMs})^{-1}$ at 1.5, 1.0 and 0.5 Tesla respectively [70]. The published baseline (precontrast) nuclear magnetic resonance relaxation data for various tissues allow one to derive an empiric formula, as given in Eq. 3.2, for the magnetic field dependence of T_1 [71].

$$T_1(0) = aB^b \tag{3.2}$$

where *B* is the strength of main magnetic field in Tesla. The values accepted are as given in Table 3.1.

Table 3.1
a and *b* values for various breast tissue [71].

Tissue	*a*	*b*
Normal fibrous tissue	732.05	0.4203
Breast carcinoma	784.79	0.3999
Fibroadenoma	988.59	0.4669

3.2.3 Imaging Sequences

Among the pulse sequences tested for breast evaluations, gradient-echo (GE) sequences, with their short acquisition times and good spatial resolutions, are currently considered to be the most suitable for dynamic contrast enhanced breast MR studies [72]. These types of sequences are similar to spin-echo sequences, with two modifications: 1) use of a flip angle ($< 90^o$), rather than the 90^o pulse used in SE and 2) use of a gradient reversal, instead of a 180^o pulse to form an echo (a GE instead of a SE). These two modifications enable a substantial amount of longitudinal magnetization to remain in the direction of the static magnetic field, without being removed by either a 90^o or an 180^o pulse. This eliminates the need to wait to allow re-growth of the longitudinal magnetization and as a result, a complete image can be acquired in seconds instead of minutes.

Gradient echo imaging also has slightly different pulse sequence versions, termed “spoiled” and “unspoiled”. The “spoiled” version of gradient-echo imaging is commonly used in DCE-MRM. The term “spoiled” refers to the fact that no transverse magnetization remains just prior to the next repetition of the pulse sequence. This spoiling occurs naturally due to T_2* decay for long repetition times (greater than 100-200 ms). For shorter repetition times, steps are taken in spoiled gradient echo imaging after signal measurement and before the next repetition of the pulse sequence to ensure that no transverse magnetization remains. The signal for spoiled gradient-echo imaging is a function of repetition time *TR*, echo time *TE*, and flip angle θ given by [73].

$$S_{GEspoiled} = \rho \times \left(\frac{1-e^{-TR/T_1}}{1-\cos\theta e^{-TR/T_1}} \right) \sin\theta \times e^{-TE/T_2*} \tag{3.3}$$

In Eq. 3.3, ρ denotes spin density.

Note that T_2*, not T_2, governs the decay of transverse magnetization, the result of forming a gradient echo rather than a spin echo. In addition, the flip angle, θ, enters the formula in a slightly complicated way. The new parameter θ, in combination with *TR*, controls the T_1 weighting of the pulse sequence. Table 3.2 describes the *TR*, *TE*, and flip angle settings needed to weight spoiled gradient-echo imaging toward T_1, T_2*, or ρ. One common feature often overlooked in spoiled gradient-echo imaging is that to maximize SNR and contrast-to-noise ratio (CNR) between tissues, as *TR* is decreased (to reduce to imaging time), θ also should be decreased, while *TE* must be sufficient to provide on-phase fat and water signals.

Table 3.2
Settings of spoiled gradient echo pulse sequences for different weights [73].

Sequence Weighting	*TR* Setting	*TE* Setting	Flip Angle Setting
T_1	< 500msec.	as short as possible	15-90 ° depending on *TR*
T_2*	any setting	as long as possible up to 2*TR*/3 or 100msec.	10-30 °
ρ	< 50msec.	as short as possible	<10°

Fat has a very short T_1 relaxation rate, thus it returns a high signal on most T_1 weighted sequences. To evidence focal enhancing lesions, fat suppression is necessary. Fat saturation (Fat Sat) and subtraction are the two techniques applied for breast MRI. Fat Sat takes advantage of the difference in resonant frequencies between water and fat. A 90° RF pulse, tuned to the resonant frequency of fat is applied, flipping the bulk magnetic vector from fat into the transverse plane. Spoiler gradients are then applied to destroy the phase coherence of the signal. This saturation routine is followed immediately by the imaging sequence and the images will only show signal from the remaining water nuclei. Fat based nuclei will not produce a signal until there is time for significant T_1 based recovery (approx. 100 msec). The great attraction of the Fat Sat technique is that it only modifies the fat signal; all other contrast relationships and signal characteristics remain the same. However, fat suppression by subtraction of the pre-contrast image from the contrast images is particularly appropriate in the breast where the anatomy is prone to extreme magnetic field inhomogeneity even after patient shimming. Therefore, subtraction images from dynamic data of spoiled GE sequences allows improved lesion detection and is preferred in the clinical practice.

GE sequences with 2D acquisitions provide a limited number of images from the whole breast. However, volumetric acquisitions with 3D GE sequences allow proper coverage of the breast without any interslice gap. Therefore, these latter types of sequences give additional diagnostic information for both lesion localization and malignancy detection.

In breast evaluations, the most commonly used sequence is the 3D Fast Low Angle Shot (FLASH) sequence, a variant of spoiled gradient-echo imaging with T_1-weighting. The settings for typical FLASH sequences are given in Table 3.3. This sequence establishes a steady state longitudinal magnetization but destroys or spoils any residual transverse magnetization using spoiling gradients before a new radio-frequency pulse is applied (Figure 3.2).

Table 3.3
Settings for the 3D Fast Low Angle Shot (FLASH) sequence [64].

Sequence Weighting	*TR* Setting	*TE* Setting	Flip Angle Setting	Field Strength
T_1	12 msec.	5msec.	25°	1.5 Tesla
T_1	14 msec.	7msec.	25°	1.0 Tesla

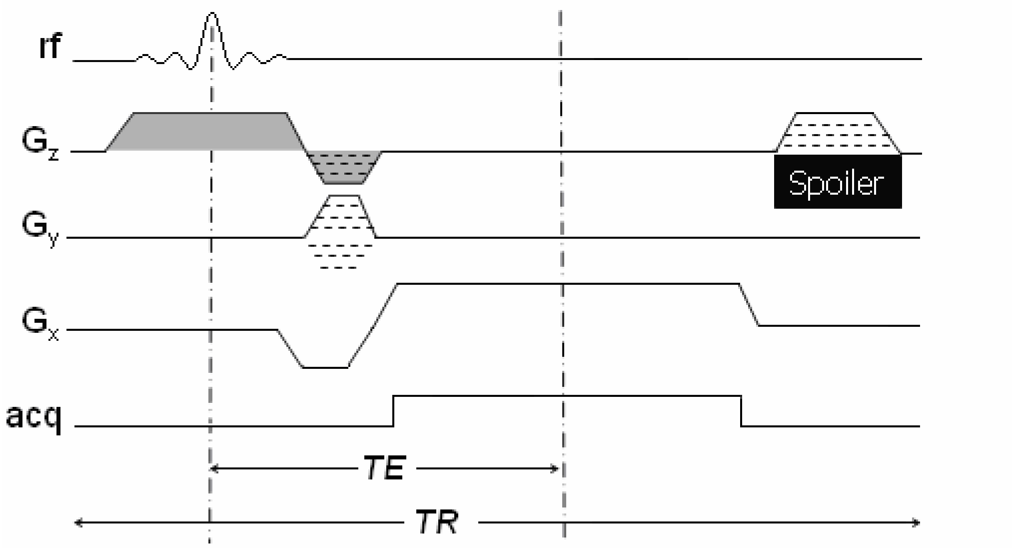

Figure 3.2 3D FLASH sequence diagram.

3.2.4 Spatial and Temporal Resolution Considerations

The spatial resolution is critical for detecting small malignant lesions. A thin slice thickness is desired to get as accurate information as possible, but this will lead to a loss of signal, as the imaged voxel is smaller, thus giving away less signal. However, because of the different sizes, forms and extent of lesions, it can be difficult to detect certain lesions due to the partial volume effect. For example in small lesions that are not completely covered by one separate slice (especially for malignancies growing in a duct-like pattern), or in a wide but thin invasive cancer in the plane of the slice. A slice thickness of 2 mm is desired, and should not exceed 4 mm, to make it possible to detect malignant lesions of 4-5 mm sizes.

The temporal resolution is very important in the evaluation of enhancement dynamics. Typically, a malignant lesion enhances strongly and early, combined with washout in the later phase. If long imaging times are used per acquisition, the possibility to discern a malignant from a benign lesion using dynamic parameters diminishes. The rim enhancement and inhomogeneities in malignant lesions can also be overlooked, as they often are discernible in early post contrast images; but for this evaluation, spatial resolution is the most crucial part.

3.3 Pitfalls

There are two groups of pitfalls: Technical and non-technical. Technical pitfalls relate to patient factors or machine factors that can influence interpretation of the MR mammograms. These include metallic artifacts, field inhomogeneities and patient movement. Especially breathing causes small movements even when examined in the desired prone position. It is extremely important to motivate the patient not to move at all during image acquisition. As the slice thickness preferably is 1-2 mm, every very minor movement or shifting of the body causes serious problems in post processing and evaluation. This can for example cause changes of slice position between image series making subtraction infeasible.

Non-technical pitfalls refer to misinterpretation of imaging findings in the absence of technical problems. These are physiological factors (menstrual cycle, pregnancy, and lactation), post-therapy changes (surgery, radiotherapy, and chemotherapy), histopathological correlation and criteria of malignancy (false positives and false negatives). Hormonally-induced enhancement may mimic disease. Surgery and radiotherapy induce morphological changes and enhancement within the breast. Chemotherapy may suppress enhancement and mask residual disease. Small lesions seen only on MRI may be difficult to locate in the pathological specimen. False positive results can arise from unfamiliarity with enhancement characteristics [74].

3.4 Lesion Interpretation Criteria

Interpretation criteria involves morphology and enhancement pattern of lesions extracted by time intensity curves.

3.4.1 Morphology

To improve differentiation between benign and malignant lesions the use of morphological criteria have been developed and reported from several sites. The criteria include shape, margin and enhancing pattern of the inspected region. While the form describes the shape of enhancing region (Figure 3.3), outer contours of a contrast enhancing region is described by margins (Figure 3.4). The contrast enhancement pattern describes the special distribution of contrast within the contrast enhancing region. The types of pattern are homogenous, inhomogeneous or septated (Figure 3.5). Another one is rim enhancement which is caused by stronger contrast uptake in tumor periphery in comparison to tumor center. Signal loss in tumor center is a sign of necrosis and fibrosis results in signal attenuation in tumor center [62].

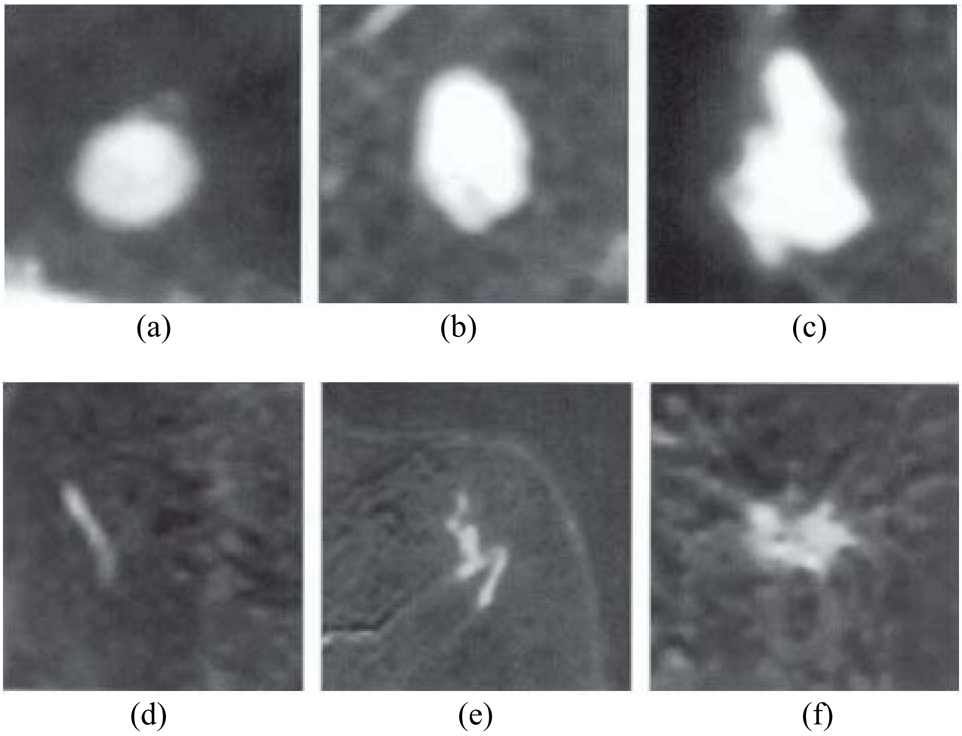
(a) (b) (c)

(d) (e) (f)

Figure 3.3 Subtraction images illustrating the various shapes of contrast-enhancing regions. (a) Round, (b) oval, (c) polygonal, (d) linear, (e) branching, (f) spiculated [62].

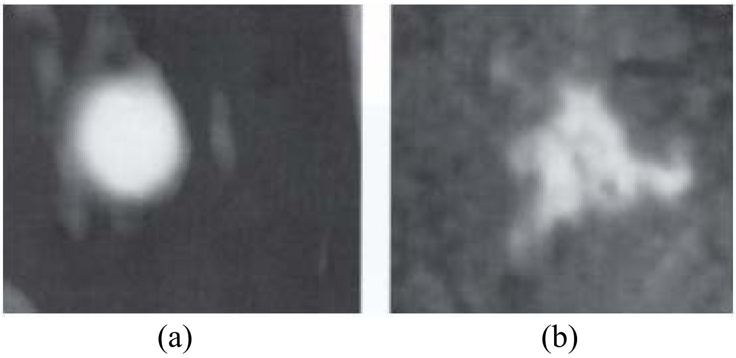
(a) (b)

Figure 3.4 Subtraction images illustrating margin differences. (a) Well defined, (b) indistinct [62].

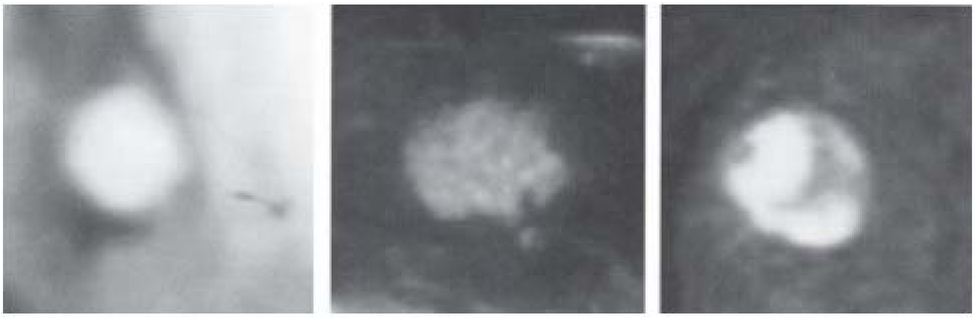

(a) (b) (c)

Figure 3.5 Subtraction images illustrating different contrast enhancement patterns. (a) Homogenous, (b) inhomogeneous, (c) septated [62].

Benign characteristics are well-defined margins and homogenous enhancement. On the contrary for rim enhancement, inhomogeneous internal pattern and irregular borders are considered typical malignant features. The analysis of shape and margin of a lesion and enhancement pattern can be of value in the differentiation, as for example fibrous strands occurring in fibroadenomas. There is however, overlap in benign and malignant features as there is with X-ray mammography. The positive and negative predictive values of various morphologic features encountered in MR imaging examinations of the breast are presented in Table 3.4. The use of scoring systems for classifying benign and malignant lesions have been advocated [24, 75].

Table 3.4
Positive predictive value of morphologic features [15].

Feature	% Positive predictive value
Smooth mass	5 - 17
Mass with nonenhancing internal septations	0 - 2
Ductal enhancement	24 - 85
Rim enhancement	40 - 86
Branching mass	32 - 84
Spiculated mass	80 - 91

3.4.2 Enhancement Dynamics

In addition to the variety of contrast enhanced GE imaging sequences used, there exists a plethora of qualitative and quantitative enhancement analysis methods that have been applied to imaging data in an attempt to differentiate benign from malignant breast lesions. Underlying all analytic methods is an assumption that benign and malignant tumors differ physiologically in such a manner that the kinetics of Gd-DTPA enhancement will differ between the pathologic entities and that these differences can be defined by DCE-MRM [76].

Angiogenesis is a crucial component in the development of various tumors and several other physiologic processes including wound healing, embryogenesis and growth of metastasis. Since it is a limiting factor for both tumor growth and metastases, it correlates with tumor aggressiveness. Physiological differences in breast tumors can thus be explained in terms of angiogenesis. In fact, a strong correlation between the initial enhancement of breast carcinomas and micro vascular densities has been observed in DCE-MRM [77, 78, 79]. It is important to mention that there are three major regions that enhance: breast lesions, ducts and blood vessels. In most cases, rapid enhancement suggests malignant lesions and gradual enhancement benign lesions. It is perfectly healthy for blood vessels to enhance.

There is some agreement regarding contrast enhancement dynamics, particularly in the positioning of the region-of-interest (ROI) and the analysis of the enhancement rate. After an enhancing lesion has been identified on subtracted images, its enhancement kinetics should be evaluated by identifying a ROI in the most enhancing part of the lesion. In clinical practice, the enhancement kinetics has been obtained by time intensity curves (TICs). The curve is plotted with signal intensity (*SI*) values directly or from computed signal enhancement (*SE*) rates using Eq. 3.4 [80].

$$SE(t) = \frac{SI(t) - SI_{pre}}{SI_{pre}} \tag{3.4}$$

where SI_{pre} and $SI(t)$ are the precontrast and post-contrast time varying intensity averages of positioned ROI. Additionally there are two well-known and accepted parameters: ISI (initial signal increase) and PSB (post-initial signal behavior), which are defined by Eqs. 3.5 and 3.6. A diagram for computing ISI and PSB is presented in Figure 3.6 [62].

$$ISI = \frac{SI_{\max 1-3\min} - SI_{pre}}{SI_{pre}} \times 100 \tag{3.5}$$

$$PSB = \frac{SI_{8\min} - SI_{\max 1-3\min}}{SI_{\max 1-3\min}} \times 100 \tag{3.6}$$

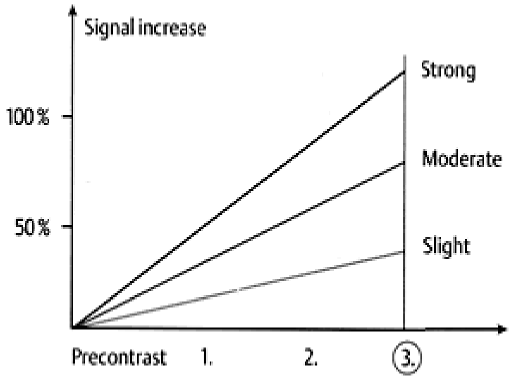

(a)

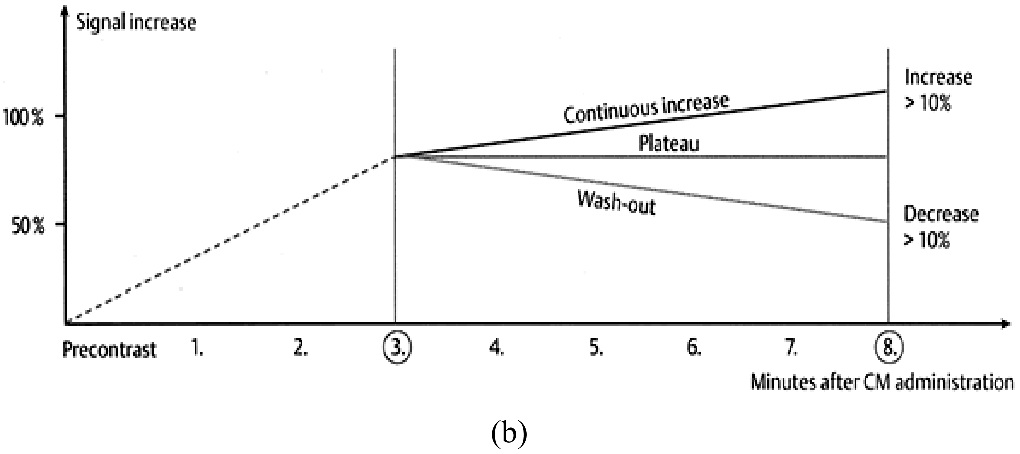

(b)

Figure 3.6 Diagram for determination of (a) initial signal increase and (b) post-initial signal behavior [60].

3.4.3 Multifactorial Interpretation

In clinical practice for the evaluation of the lesions, it is recommended to use MR mammography breast imaging reporting and data system (MRM-BIRADS) employing a multifactorial protocol in which each evaluation criteria receives a point value. Using the system presented in Table 3.5, findings with a total score of less than 3 points generally correspond to benign lesions, whereas a total score greater than 3 points indicates malignancy as seen in Table 3.6.

Table 3.5
Multifactorial evaluation protocol [62].

Criterion		Points
Form	Round	0
	Oval	0
	Polygonal	0
	Linear	0
	Branching	1
	Spiculated	1
Margins	Well defined	0
	Indistinct	1
Enhancing pattern	Homogenous	0
	Inhomogenous	1
	Septated	0
	Rim enhancement	2
Initial signal increase	< 50 %	0
	50 – 100 %	1
	> 100%	2
Postinitial signal behavior	Steady increase	0
	Plateau	1
	Wash-out	2

Table 3.6
Evaluation scores [62].

Total Score	0	1	2	3	4	5	6	7	8
Group	I Benign		II	III Questionable	IV		V Malignant		

3.5 Computer Assistance and Quantitative Methods in DCE-MRM

In order to accurately assess breast cancer with DCE-MRM, a large volume of image data, acquired at high spatial and temporal resolutions must be analyzed. T_2-weighted images, pre and post-contrast T_1-weighted images and subtraction images created from the dynamic data, must all be inspected by the radiologist slice by slice to localize lesions. This is a tedious and time consuming task, as suspected regions can be very small and there may be several deceptively enhanced healthy regions that need careful discrimination, such as blood vessels and normal parenchyma especially in case of premenopausal women. Once a lesion is localized, the radiologist must carefully evaluate its morphology and/or enhancement dynamics to detect malignancy. The major motivation behind this is the fact that typically, irregular morphology, irregular or spiculated margins, heterogeneous internal enhancements and rim enhancements are signs of malignancy, while smooth margins and homogenous internal enhancements are associated with benign lesions. Malignant lesions are characterized by faster and stronger enhancements than benign lesions, although some malignant lesions may produce enhancement only slowly or minimally, and a variety of benign lesions may produce enhancement rapidly with marked signal increase. These assessments are highly time-intensive, experience and observer dependent, especially when lesion volumes are considered. In the standard clinical practice, due to the enormous image data that must be processed and interpreted, a typical (manual) patient evaluation requires constant and diligent attention for periods exceeding 30 minutes. Clearly, there is a great need for systems that automatically extract important diagnostic features of the image data and present them to the radiologists for decision support.

Recently, a number of algorithms, methods and computerized systems have been developed to aid radiologists and several software packages that facilitate extraction of important diagnostic features and provide considerable assistance to the radiologists have been developed [6, 36]. Some of these software just provide color-coded parametric maps of enhancements to make visualization of suspiciously enhancing regions uncomplicated and to facilitate overall analysis [4-7] and rely on manual identification of lesions which make them time-consuming, highly subjective and error-prone. There are thus efforts reported in the literature to minimize the need for operator guidance in diagnostic evaluations; for X-ray mammography [8, 9], for sonography [10], for tomosynthesis [11] and for computed tomography [12]. To the best of our knowledge, there is one short abstract reported on a fully automated lesion localization technique for DCE-MRM [13]. A more detailed literature survey concerning lesion localization is presented in Sections 4.1 and 5.1.

During the past decade, the diagnostic significance of lesion morphology and qualitatively assessed morphological parameters have been studied [15-17] and automated methods have been developed to automatically extract diagnostically useful information using delayed fat suppressed post-contrast images or subtraction images that are helpful to suppress less enhancing normal parenchyma that surround the lesions and to highlight avidly enhancing regions [18-21]. For detection of malignancy, automated enhancement analysis methods that make use of a number of protocols and quantitative interpretation criteria such as maximum signal enhancement rates at specific times, time to maximum enhancement, wash-out ratio and maximum intensity-time ratio to improve diagnosis have been developed [15, 22-35]. A more detailed survey on available malignancy detection methods is given in Sections 6.1 and 7.1. A summary of the available software packages that facilitate extraction of important diagnostic features and provide considerable assistance to the radiologists is given in Section 8.1.

4. LESION LOCALIZATION WITH CELLULAR NEURAL NETWORKS AND 3D TEMPLATE MATCHING

4.1 Introduction

Breast cancer is the most commonly diagnosed and the second leading cause of cancer death among women. Although X-ray mammography is the conventional screening tool used to detect and diagnose breast cancer, due to it's ionizing nature and well-known limitations, especially on fibroglandular tissues, high-resolution, dynamic contrast-enhanced, magnetic resonance mammography (DCE-MRM) is gaining increased acceptance in breast evaluations [81, 82].

In DCE-MRM a radiologist first identifies enhancing regions and marks a region of interest (ROI) and then tries to detect and evaluate lesions according to their morphology, enhancement dynamics or both [15]. The acquired and constructed images for MRM are too many to be visually inspected by the radiologist; evaluation of these images is a time-consuming and experience-dependent process. Missing of a very small detail may result in poor specificity and sensitivity in the final diagnosis. Thus, automated systems that provide decision support to radiologists have been under development. These systems, in general, use features extracted from intensity changes between pre and post-contrast images. In a number of recent work reported in the literature, normalized maximum intensity-time ratio (*nMITR*) and features derived from it have been used in decision-making. A brief summary of these is presented below.

Szabo et al [16] used artificial neural networks to establish a diagnostic criterion. The MR features are morphology and enhancement dynamics of a number of 105 lesions. Lesion morphology was determined qualitatively. Enhancement dynamics were computed for manually drawn ROIs positioned over a tumor area that showed high contrast uptake at the early post-contrast stage. The performance of the proposed neural network model was found to be comparable to that of an expert radiologist with a diagnostic accuracy of 77%.

Liney et al [32] compared user-defined and semi-automated region of interests. A total number of 117 lesions were examined. Three types of analysis were performed: Whole lesion ROI, the most enhancing 9 voxel ROI and 10% threshold ROI. High significance was achieved when small semi-automated ROI approaches were used. However it was concluded that the significance of the ROI approaches was highly associated with the radiologists' experience. Gibbs et al [34] assessed the benefits of quantification of contrast enhancement in the differential diagnosis of sub-1cm breast lesions. In the beginning of the analysis, for each lesion an experienced radiologist drew ROI to encompass the whole lesion as closely as possible. With a logistic regression model they achieved a diagnostic accuracy of 92%. Kneeshaw et al [35] applied whole lesion ROI drawn by radiologist and most enhancing 9 voxel inside the whole ROI detected by a software to differentiate breast diseases associated with screening detected microcalcifications. 88 patients enrolled in the study. The highest sensitivity is 80% and obtained using 9-voxel ROI.

In the schemes discussed so far the ROI must be marked by an expert; clearly a time-consuming process. The advantages of automated ROI selection were explored by Kuhl et al [83]. They showed that an automated ROI is able to cut down the time needed for quantitative analysis while improving the reproducibility of quantitative enhancement values due to standardization of ROI analysis.

Tzacheva et al [20] analyzed two dimensional margin and shape features of masses segmented by operator-controlled intensity thresholding of post-contrast sagittal fat suppressed T_1-weighted breast images to diagnose malignancy. Deurloo et al [84] rated morphological and temporal features in and around the segmented breast lesion. The segmentation is automatic in three dimensions after a point in the lesion is designated manually on the MR image by a radiologist. It was concluded that computerized analysis has the potential to increase overall performance for clinically and mammographically occult lesions. Chen et al [85] presented a fuzzy c-means (FCM) clustering based method for 3D segmentation of lesions from contrast enhanced breast MR images. The algorithm consisted of lesion enhancement within a manually selected ROI, FCM clustering, lesion membership map generation, connected-component labeling, object selection and hole-filling.

In all the studies mentioned above, some kind of user interaction is necessary. The user must either mark a whole or partial ROI, or mark a single point inside a suspicious region, or give an intensity threshold value.

In the present study, we introduce a fully automated method that detects lesions in three dimensions without any human interaction. It should be noted that the objective in the present work is solely detection, not discrimination and that for reliable extraction of discriminating features in diagnosing malignancy, a more accurate segmentation than used here may be mandatory. A simplified flow chart of the process is presented in Figure 4.1.

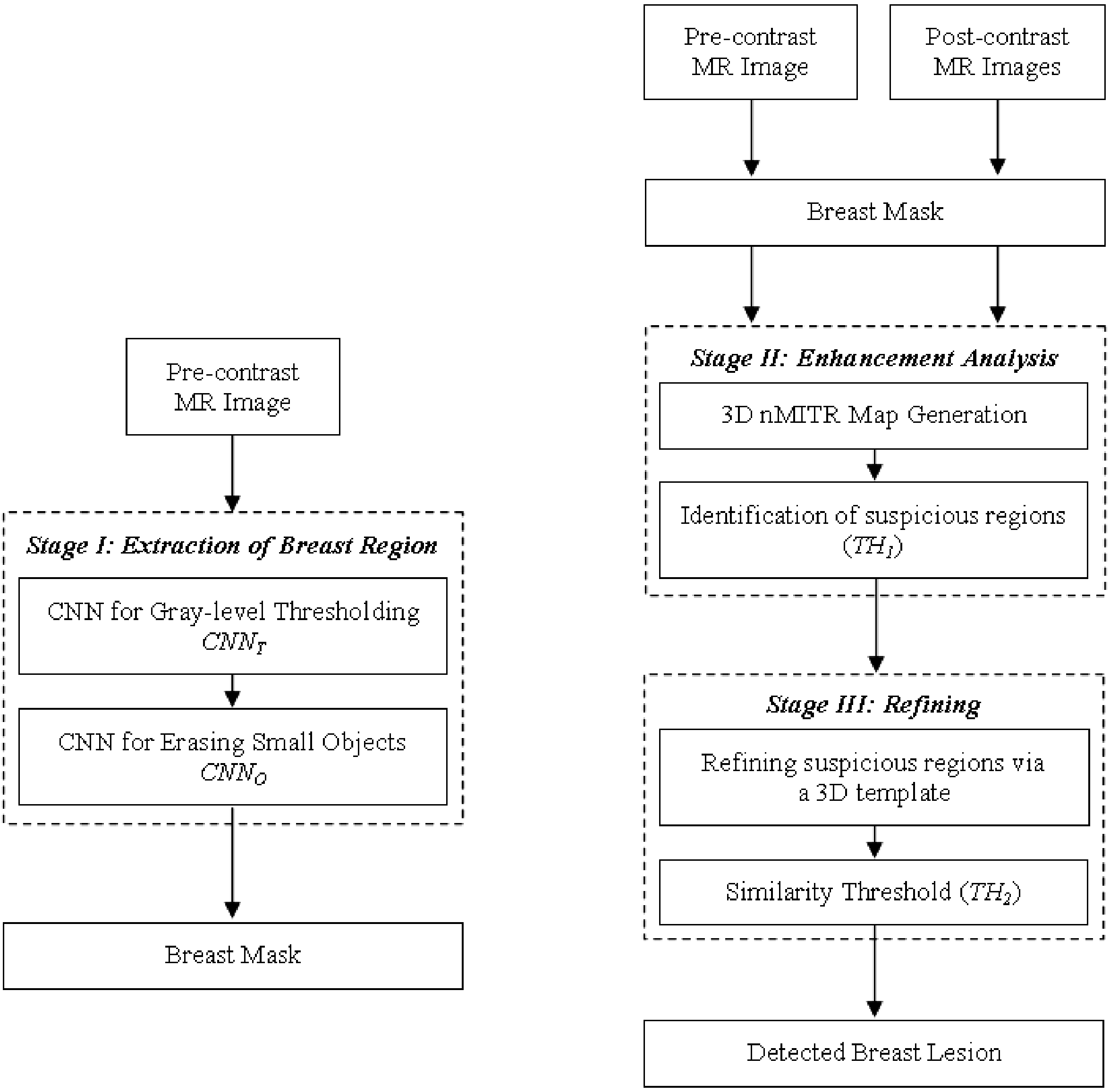

Figure 4.1 Simplified flowchart of the proposed breast lesion detection scheme.

4.2 Imaging Protocol

Magnetic resonance imaging is conducted on a 1.5 Tesla MR imager (Magnetom Symphony, Siemens Medical Systems, Erlangen, Germany) equipped with a gradient system having a maximum amplitude of 30 mT/m. Patients are placed in a prone position during the scan to minimize motion artifacts. A dedicated four-element phased-array receiver breast coil is used. The imaging sequence is a variant of spoiled gradient echo imaging sequence, 3D fast low angle shot (FLASH) (TR/TE 9.80/4.76 ms, flip angle 25 ^{o}, field of view 320×320 mm, matrix size 512×512, slice thickness 2.5 mm, $0.625\times0.625 mm^2$ resolution in x and y directions). Sequential axial images (One pre-contrast and five post-contrast) are obtained per slice, during and immediately after the bolus injection of contrast agent Gd-DTPA (0.1 mmol/kg body weight).

4.3 Patient Population and Image Dataset

The dataset analyzed in this study consists of 2064 CE-MR mammograms from 19 women (age: 32-83 years, mean age: 48.8 years) in 344 slices. 19 benign and 20 malignant lesions have been manually marked in the slices by two expert radiologists after mutual agreement (approximate lesion center is marked; the whole lesion contour is not delineated). The benign lesions are ten fibroadenomas, five adenosis, two mastitis, an abscess and an infected cyst. The malignant lesions are eleven invasive ductal carcinomas, five invasive papillary carcinomas, three invasive lobular carcinomas and a ductal carcinoma in situ. All these findings have been supported either by histopathological examination or by clinical follow-up. Dot like enhancements, smaller than 5 mm, have been left unmarked. The smallest lesion in the dataset is 0.14 cm^3 in volume and has a round shape; the largest lesion is 17.23 cm^3 in volume and has an irregular shape. Fourteen lesions are round and the remaining are ovoid or irregular.

All images are transferred in a DICOM format from the imaging device to a personnel computer for analysis. The analysis method described in this thesis is numerically implemented using Matlab 7.0 (The MathWorks, Inc., USA).

4.4 Breast Region Extraction using Cellular Neural Networks

During detection of lesions in axial breast MR images, regions that are out of interest such as thoracic cavity, lungs and heart must be carefully segmented out to reduce computational burden and to prevent false positive detections in the vicinity of these regions.

Air produces a near-zero MR signal so the breast-air boundary can be detected easily by simply searching a sharp increase in the signal. On the other hand, detection of the breast chest wall boundary is an ill-posed problem due to motion of the hearth and lungs. Hayton et al [86] proposed a technique that performs morphological operations (iterative morphological erosion followed by dilation) and graph search to find an approximate location of the chest wall on the pre-contrast images. Although it generates accurate results for certain patients, it requires a long process time and fails if the patient's chest is not flat. Twellmann et al [87] introduced a method that combines median filtering, gray-level based thresholding and morphological operations on pre-contrast images. Most probably, due to the thresholding technique that is used, breast tissue segmentation seems to fail in regions near the chest wall.

In this study, we introduce a segmentation approach that does not require prior information concerning breast anatomy such as chest wall flatness, prior mastectomy history. The method uses Cellular Neural Networks (CNNs) as an alternative way to perform morphological operations, a technique described previously by Yang et al [88] and Brugge et al [89]. Since CNNs can be implemented in hardware using special CNN chips, images can be processed in (almost) real-time; for example, Harrer et al report that a basic morphological operation can be completed within 1μs, independent of the image size and the structuring elements [90].

CNNs have been used for medical image processing previously by various investigators. Rekeczky et al [91] have shown feasibility of CNN based real-time feature extraction from echocardiographic images. Zarandy et al. [92] have used a CNN to analyze X-ray mammograms. Girodana et al [93] have proposed a CNN based technique for fast and accurate detection of craniofacial landmarks on X-ray images. Shitong et al [94] have studied automated white blood cell detection methods using microscopic blood images and showed that the CNN based method works better when compared with the existing two methods: threshold segmentation followed by mathematical morphology and the fuzzy logic method. A general review of of CNN-based medical imaging can be found in [95].

CNNs are locally interconnected cells arranged into arrays (regularly spaced positions) [96]. Let $C_{i,j}$ represent the cell located in the (i, j)-th position of a 2D $M \times N$ image and let $N_{i,j}$ represent the r-neighborhood of the cell $C_{i,j}$ and is defined by

$$N_{i,j} = \left\{ C_{l,m} \mid \max(|l-i|,|m-j|) \le r;\ 1 \le l \le M,\ 1 \le m \le N \right\} \tag{4.1a}$$

where r is a positive integer. The pixel intensity (the state) $x_t(i,j)$ at this location can be described by the following (discrete) state equations:

$$x_{t+1}(i,j) = \sum_{C_{l,m} \in N_{i,j}} A_{l,m} \times y_t(i+l, j+m) + \sum_{C_{l,m} \in N_{i,j}} B_{l,m} \times u(i+l, j+m) + b \tag{4.1b}$$

$$y_t(i,j) = 0.5 \times \left\{ \left| x_t(i,j) + 1 \right| - \left| x_t(i,j) - 1 \right| \right\} \tag{4.1c}$$

where $u(i,j)$ is the input, $x_t(i,j)$ and $y_t(i,j)$ are the state and the output of the cell $C_{i,j}$ at the t-th stage, respectively. $A_{l,m}$ and $B_{l,m}$ are the entries at the l,m-th neighborhood of the feedback and control templates A and B, centered at the location i,j. b is a constant bias parameter. The initial state and the input is assumed to have a magnitudes less than or equal to 1. Note that $|y_t(i,j)| \le 1$ for all $t \ge 0$. Since the initial state values of CNNs are bounded between -1 and +1, the pre-contrast image intensity values are normalized before use by

$$\tilde{I}_{pre} = \left(2 \times \frac{I_{pre} - \min(I_{pre})}{\max(I_{pre}) - \min(I_{pre})} \right) - 1 \tag{4.2}$$

where I_{pre} is the pre-contrast image, $\min(\cdot)$ and $\max(\cdot)$ denote the minimum and maximum operators.

In this study, we segment the breast region from the pre-contrast MR image by applying a CNN for gray-level thresholding (*CNN_T*) followed by another CNN (*CNN_O*) to erase small objects and smooth sharp corners. We use a modified version of the CNN of Chua et al [97] for thresholding and a modified version of the CNN of Zarandy et al [98] for removing small objects. The updated parameter values are given in Table 4.1. Note that although the bias *b* in Table 4.1 seems to remain the same for all the images, the actual threshold is not *static* because of normalization of the pre-contrast images. (The thresholding with the given parameters is equivalent to thresholding the image at 14% of the intensity range, i.e at $\min(I_{pre}) + 0.14 \times \left[\max(I_{pre}) - \min(I_{pre})\right]$). Note also that to remove certain horizontal artifacts that could cause false detections, *CNN_O* deliberately contains some "offset" and is therefore nonsymmetrical.

Table 4.1
Parameter values of the CNNs used.

	Input	Initial State	**A**	**B**	*b*
CNN_T CNN for Gray-level thresholding (r=1)	0	Normalized pre-contrast image	$\begin{bmatrix}0&0&0\\0&2&0\\0&0&0\end{bmatrix}$	$\begin{bmatrix}0&0&0\\0&0&0\\0&0&0\end{bmatrix}$	0.72
CNN_O CNN for erasing Small Objects (r=2)	0	Thresholded pre-contrast image	$\begin{bmatrix}0&0&0&0&0\\1&1&1&1&1\\1&1&0&1&1\\1&1&1&1&1\\0&0&0&0&0\end{bmatrix}$	$\begin{bmatrix}0&0&0&0&0\\0&0&0&0&0\\0&0&0&0&0\\0&0&0&0&0\\0&0&0&0&0\end{bmatrix}$	0

Stopping the CNNs

CNN_T: After each iteration of the CNN algorithm (1), the voxel values (normalized to have values between -1 to +1) change towards either +1 or -1, except those selected by the bias value. As the process stabilizes, this change will eventually go towards zero.

Therefore we stop when the total number of voxel intensity having values of either -1 or +1 do not change from iteration to iteration. Our experience shows that after about 10 iterations a stable state is reached.

CNN$_O$: In this case, the image to be processed is binary; therefore after each iteration we look whether there is any difference between the voxel intensities. If there is no difference after eight successive iterations we stop; we also stop if this creation cannot be met within 250 iterations.

4.5 Lesion Detection with a 3D Template

To detect lesions, MR mammograms are enhanced using contrast agents. Computerized enhancement analysis may be performed by using the enhancement rate of a tissue at a specific location. In this study, we use normalized maximum intensity-time ratio (*nMITR*) computed over the pre and post-contrast images using the following equations:

$$SE_{\Re}(\nu) = \frac{I_{\Re}(\nu) - I_{\Re}(0)}{I_{\Re}(0)} \times 100 \tag{4.3}$$

$$nMITR_{\Re} = \frac{\max\{SE_{\Re}\}}{T_{\max}} \tag{4.4}$$

In Eqs. 4.3, 4.4, $\Re$ denotes a region of interest (ROI), $I_{\Re}(\nu)$ and $I_{\Re}(0)$ are the mean intensity values of the ROI on the ν-th post-contrast and pre-contrast images, respectively ($\nu = 1, 2, \cdots, 5$). $SE_{\Re}(\nu)$ is the enhancement rate of the ROI at the ν-th time point; $\max\{SE_{\Re}\}$ is the maximum enhancement rate and T_{max} is the time in seconds when the maximum is reached [34].

For the segmented breast tissue, we generate a 3D nMITR map $S(i, j, k)$ using a moving ROI of 3×3 voxels. This map is passed through a threshold to identify suspicious enhancements and remove (falsely enhanced) fatty tissue, muscles, and parenchymal breast tissue ($TH_1 = 0.33$). This threshold value is chosen so that, after thresholding only tissue that has

1. 40% and higher maximum enhancement at 2 minutes (after contrast agent administration), or
2. 60% and higher maximum enhancement at 3 minutes (after contrast agent administration), or
3. 150% and higher maximum enhancement at 8 minutes (after contrast agent administration)

remains in the processed image. The 3D binary image obtained after the thresholding is given by:

$$P(i,j,k) = \mu\{S(i,j,k) - 0.33\} \tag{4.5}$$

where $\mu(\cdot)$ represents the unit step function.

In clinical practice, radiologists mentally make use of lesion anatomy for lesion detection. In this work, we use a similar approach with a 3D template that consists of three layers of 12×12 cells as as given in Eq. 4.6. Q represents the template in the middle layer; Q^+ and Q^- the templates in the top and the bottom layers with respect to the middle layer. It is assumed that the template entries are zero at undefined locations. Using this template it is possible to detect small lesions; if more layers are used the resolution might decrease. The thresholded map, *P*(*i,j,k*) is processed with this template using the following convolution operation given in Eq. 4.7.

$$Q^{+} = Q^{-} = \begin{bmatrix} 0 & 0 & 0 & 0 & 0 & 0 & 0 & 0 & 0 & 0 & 0 & 0 \\ 0 & 0 & 0 & 0 & 0 & 1 & 1 & 0 & 0 & 0 & 0 & 0 \\ 0 & 0 & 0 & 1 & 1 & 1 & 1 & 1 & 1 & 0 & 0 & 0 \\ 0 & 0 & 1 & 1 & 1 & 2 & 2 & 1 & 1 & 1 & 0 & 0 \\ 0 & 0 & 1 & 1 & 2 & 2 & 2 & 2 & 1 & 1 & 0 & 0 \\ 0 & 1 & 1 & 2 & 2 & 2 & 2 & 2 & 2 & 1 & 1 & 0 \\ 0 & 1 & 1 & 2 & 2 & 2 & 2 & 2 & 2 & 1 & 1 & 0 \\ 0 & 0 & 1 & 1 & 2 & 2 & 2 & 2 & 1 & 1 & 0 & 0 \\ 0 & 0 & 1 & 1 & 1 & 2 & 2 & 1 & 1 & 1 & 0 & 0 \\ 0 & 0 & 0 & 1 & 1 & 1 & 1 & 1 & 1 & 0 & 0 & 0 \\ 0 & 0 & 0 & 0 & 0 & 1 & 1 & 0 & 0 & 0 & 0 & 0 \\ 0 & 0 & 0 & 0 & 0 & 0 & 0 & 0 & 0 & 0 & 0 & 0 \end{bmatrix} \tag{4.6a}$$

$$Q = \begin{bmatrix} 0 & 0 & 0 & 0 & 0 & 1 & 1 & 0 & 0 & 0 & 0 & 0 \\ 0 & 0 & 0 & 1 & 1 & 1 & 1 & 1 & 1 & 0 & 0 & 0 \\ 0 & 0 & 1 & 1 & 1 & 2 & 2 & 1 & 1 & 1 & 0 & 0 \\ 0 & 1 & 1 & 1 & 2 & 2 & 2 & 2 & 1 & 1 & 1 & 0 \\ 0 & 1 & 1 & 2 & 2 & 2 & 2 & 2 & 2 & 1 & 1 & 0 \\ 1 & 1 & 2 & 2 & 2 & 2 & 2 & 2 & 2 & 2 & 1 & 1 \\ 1 & 1 & 2 & 2 & 2 & 2 & 2 & 2 & 2 & 2 & 1 & 1 \\ 0 & 1 & 1 & 2 & 2 & 2 & 2 & 2 & 2 & 1 & 1 & 0 \\ 0 & 1 & 1 & 1 & 2 & 2 & 2 & 2 & 1 & 1 & 1 & 0 \\ 0 & 0 & 1 & 1 & 1 & 2 & 2 & 1 & 1 & 1 & 0 & 0 \\ 0 & 0 & 0 & 1 & 1 & 1 & 1 & 1 & 1 & 0 & 0 & 0 \\ 0 & 0 & 0 & 0 & 0 & 1 & 1 & 0 & 0 & 0 & 0 & 0 \end{bmatrix} \tag{4.6b}$$

$$R(i,j,k) = \sum_{l=1}^{M} \sum_{m=1}^{N} \sum_{n=1}^{O} Q(l,m,n) \times P(i+l, j+m, k+n) \tag{4.7}$$

here M, N and O are the height, width and the depth of the projected image. At the end of the template processing, regions geometrically similar to the template become enhanced. To detect breast lesions, we pass the convolution result from a threshold that yields a similarity (to the template designed) of 47% ($TH_2 = 150$). A lower value will result in increased false positive detections due to enhanced blood vessels while higher values will result in missed lesions.

4.6 Performance Analysis

The success of lesion detection is very much dependent on proper segmentation of the breast. Two metrics, *RO* (relative overlap) and *MCR* (misclassification rate) are used to quantify the performance of breast segmentation. These metrics have been used before by Song et al to compare accuracy of different segmentation methods for brain MR images [99]. The relative overlap (also called segmentation precision in [100]) and misclassification rate are calculated using

$$RO = \frac{B_s \cap B_r}{B_s \cup B_r} \tag{4.8a}$$

$$MCR = 1 - \frac{B_s \cap B_r}{B_r} \tag{4.8b}$$

In (4.8a) and (4.8b), B_s denotes the set of voxels of the breast region estimated by the CNN segmentation and B_r represents the set of voxels delineated by the expert (obtained by correcting the results of CNN segmentation). The value of *RO* ranges from 0 (no overlap) to 1 (complete overlap). The value of *MCR* is also bounded between 0 (no misclassified voxels) and 1 (total misclassification). A breast region is considered to be properly segmented when the relative overlap is larger than 0.85 and when the misclassification rate is smaller than 0.10.

To asses the success of lesion detection, *Detection Sensitivity*, FP_{slice} (false-positive rate per slice) and FP_{lesion} (false-positive rate per lesion) are used. These metrics are defined as follows [101]:

$$Detection\ Sensitivity\ (\%) = \frac{Number\ of\ True\text{-}Positive\ Detections}{Total\ Number\ of\ Lesions} \times 100 \tag{4.9a}$$

$$FP_{slice}(\%) = \frac{Number\ of\ Slices\ Containing\ False\text{-}Positive\ Detections}{Total\ Number\ of\ Slices} \times 100 \tag{4.9b}$$

$$FP_{lesion}(\%) = \frac{Number\ of\ False\text{-}Positive\ Detections}{Total\ Number\ of\ Lesions} \times 100 \tag{4.9c}$$

A detection is accepted to be a true-positive detection if a voxel within the detected volume has previously been marked by experts as a lesion center; otherwise, it is a false-positive detection. This definition is appropriate here because the objective is solely lesion detection, not discrimination. However, it should be applied with great caution for comparison purposes since it will favor a method that oversegments lesions.

4.7 Results

For illustrating the technique two cases are considered. The first case is for a patient with an ovoid malignant lesion (51-year-old woman with an invasive ductal carcinoma, on the left breast manually marked at slices 20-24). Figure 4.2a shows the pre-contrast image and the automatically segmented breast region (as a contour overlay) corresponding to the representative slice stack in which the lesion has the largest diameter (slice 22). Figure 4.2b is an image that shows the maximum intensity regions for the stack under consideration. This maximum intensity image (MII) is generated pixel by pixel by assigning the maximum intensity among the five subtraction images of the stack, obtained by subtracting the post contrast images from the pre contrast image. Figure 4.2c and Figure 4.2d show the nMITR maps computed for the whole slice and for the segmented breast. The results of template matching and thresholding are presented in Figures 4.2e-4.2f. The lesion is detected in all slices without false positives. The breast region manually delineated by the expert, the region segmented automatically and the lesion detected are shown in Figures 4.3a-4.3e.

(a)

(b)

Figure 4.2 Representative slice stack (slice 22) for a 51-year old woman with an ovoid malignant lesion. (a) Pre-contrast axial breast image with superimposed automatically segmented breast region as a contour overlay, (b) maximum intensity image ("×" indicates the lesion center), (c) computed nMITR map for the whole slice (nMITR values greater than 0.33 are in white), (d) Figure 4.2c after masking with the segmented breast region, (e) output after 3D template matching, (f) suspiciously enhancing regions detected after thresholding.

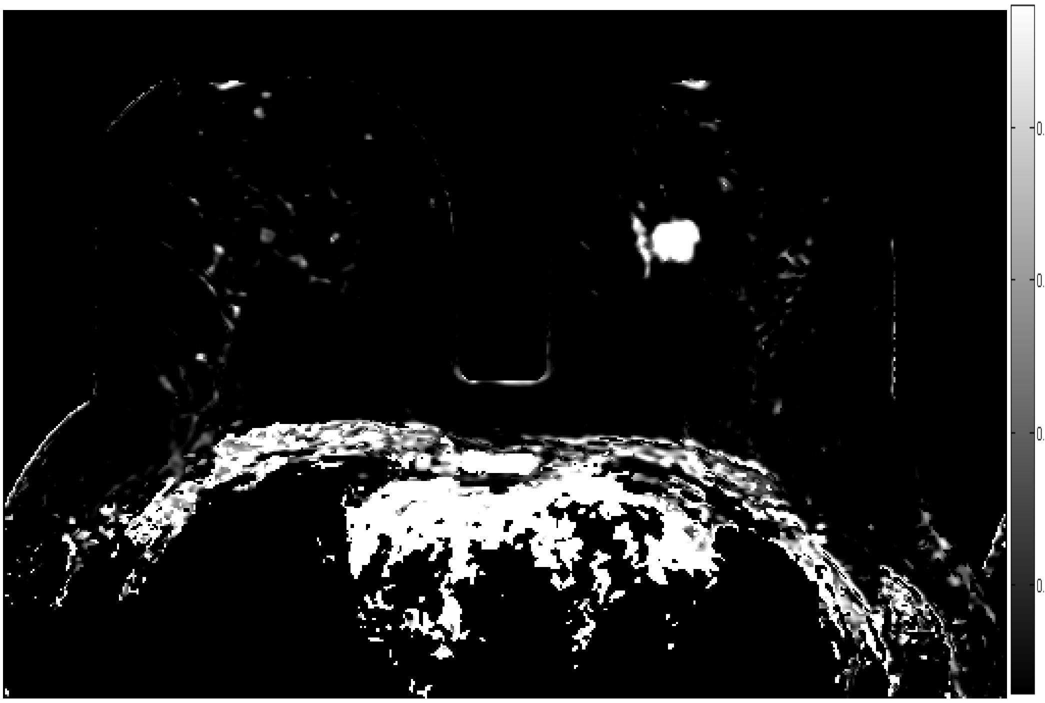

(c)

(d)

Figure 4.2 Continued

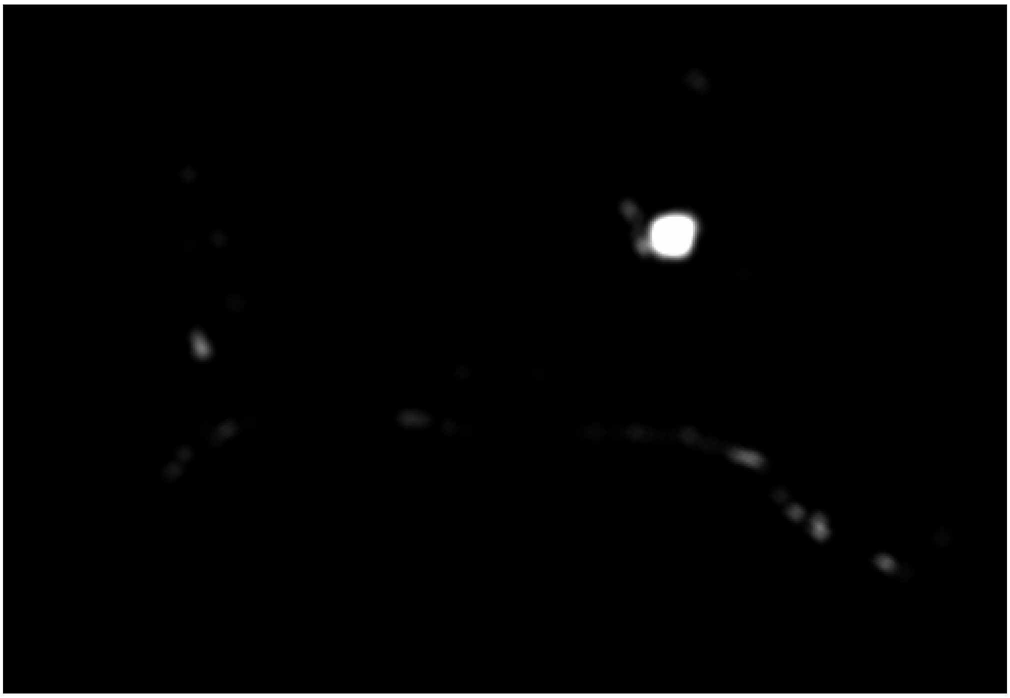

(e)

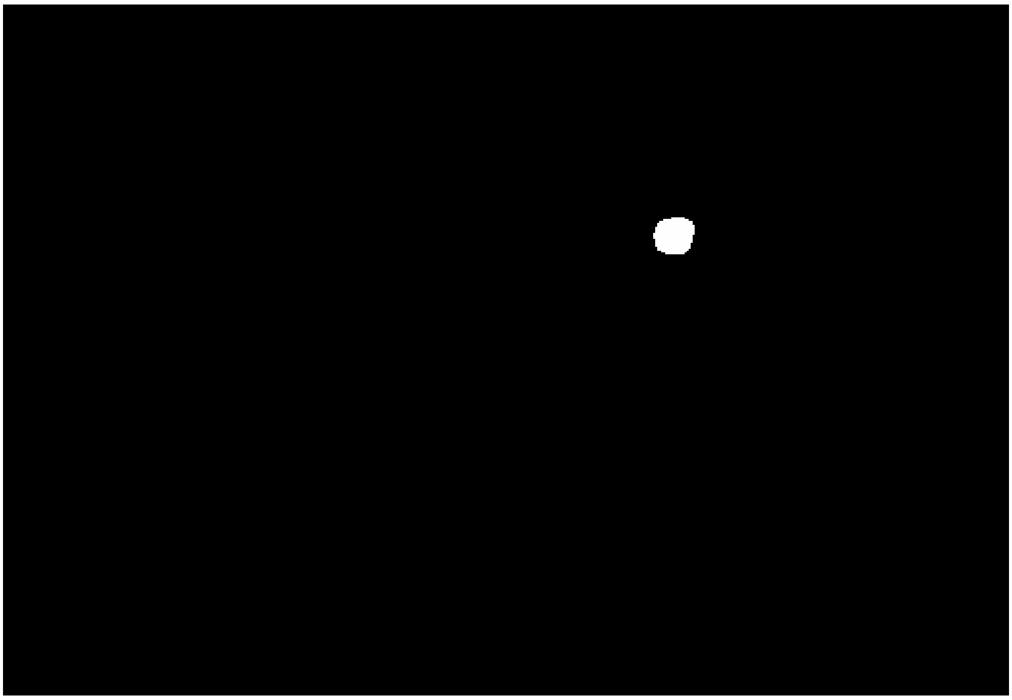

(f)

Figure 4.2 Continued

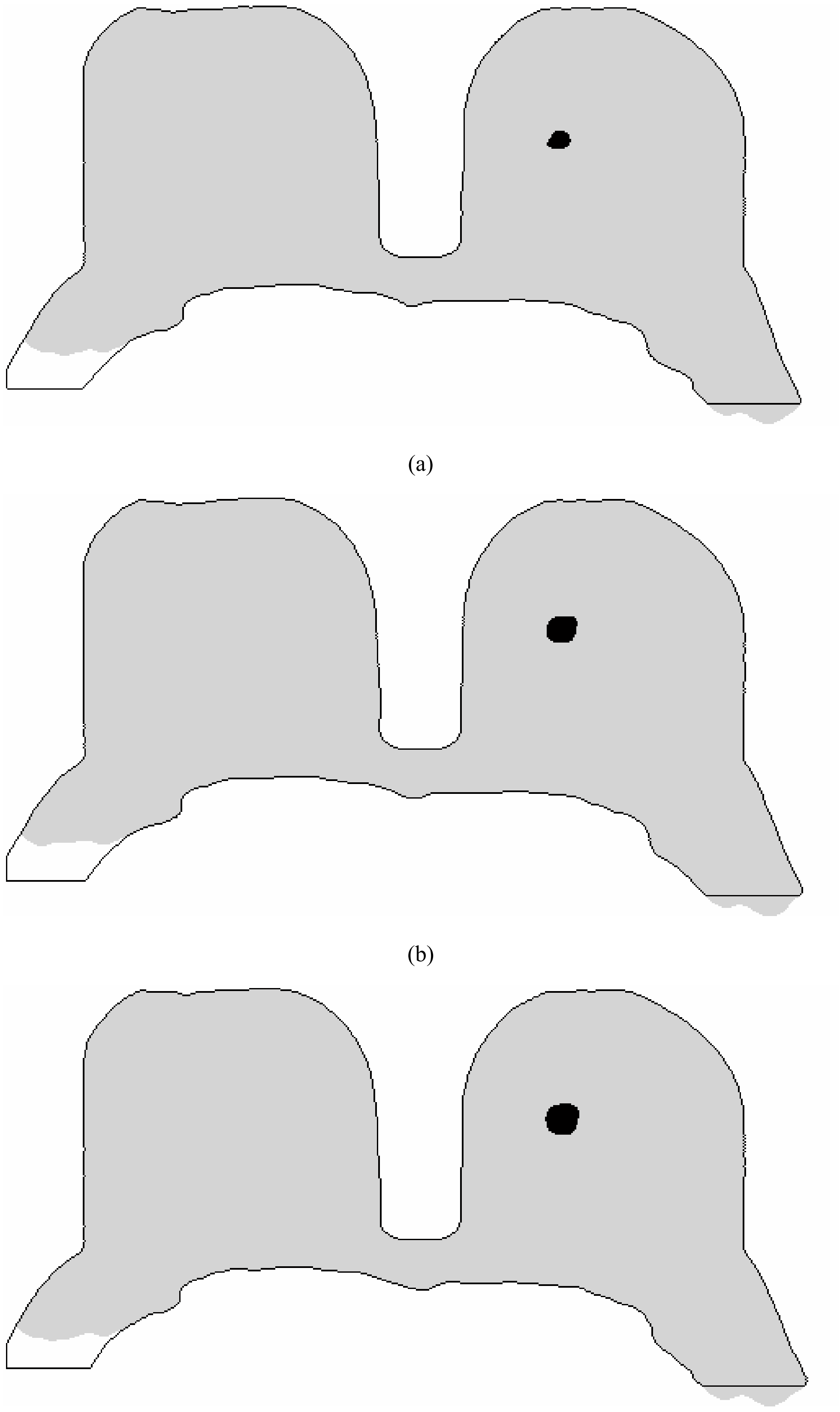

(a)

(b)

(c)

Figure 4.3 Breast region manually delineated by the expert (solid black contour), the region segmented automatically (gray colored area) and the lesion detected by the system (black colored area), (a-e) slices 20 to 24.

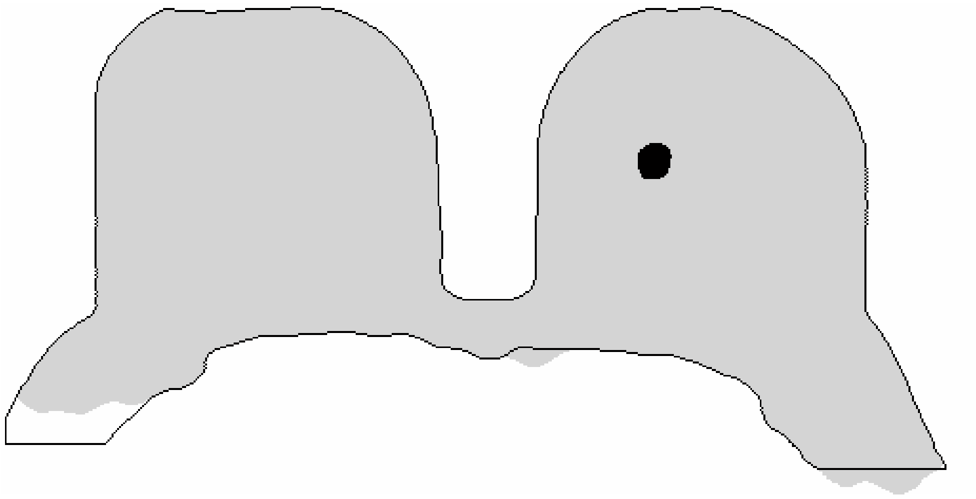

(d)

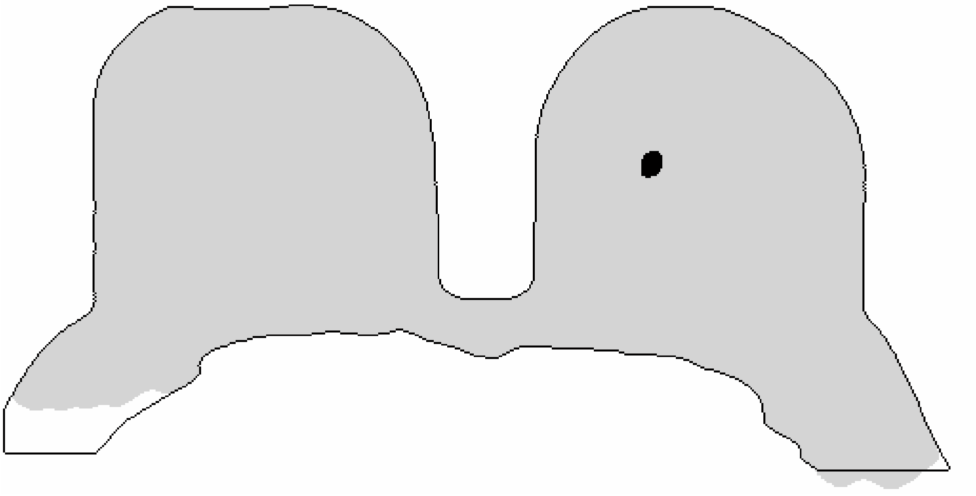

(e)

Figure 4.3 Continued.

In the second case a patient with an irregular malignant lesion (41-year-old woman with an invasive ductal carcinoma on the left breast manually marked at slices 13-25) is considered. The results for the representative slice stack (slice 18) are given in Figures 4.4a-4.4f. As illustrated in Figures 4.5a-4.5m, the lesion is detected in all the slices without false positives. Note that lesion spicules are removed due to the round mass template; for lesion detection, this loss of morphological information is tolerable. For discriminating malignancy, however, morphological information is important and therefore different segmentation techniques that preserve morphology must be used.

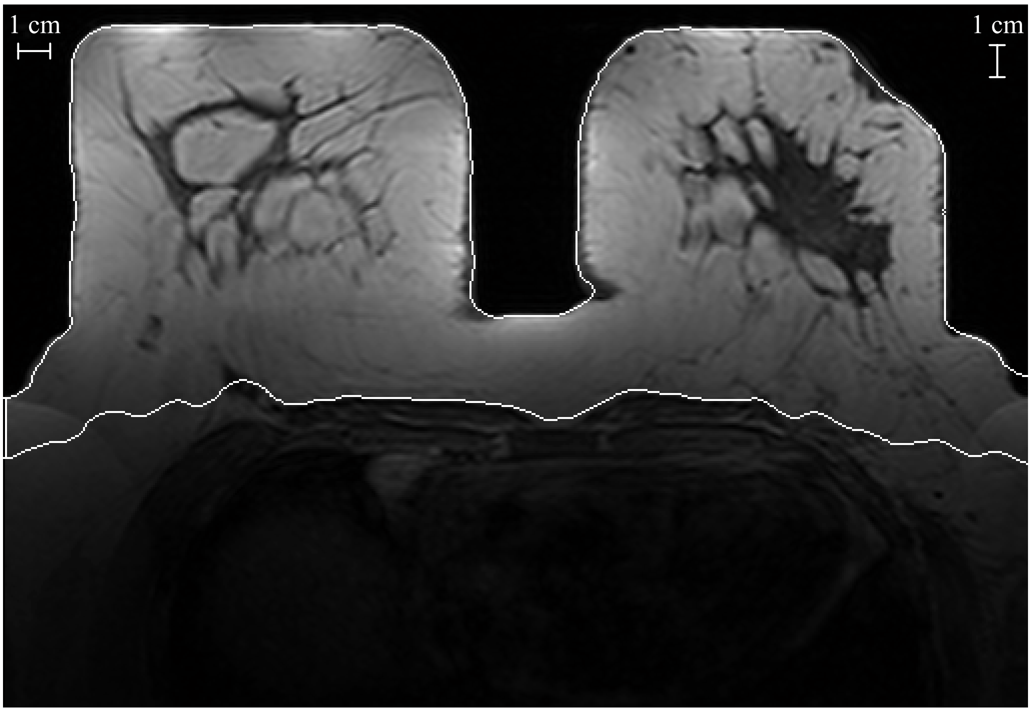

(a)

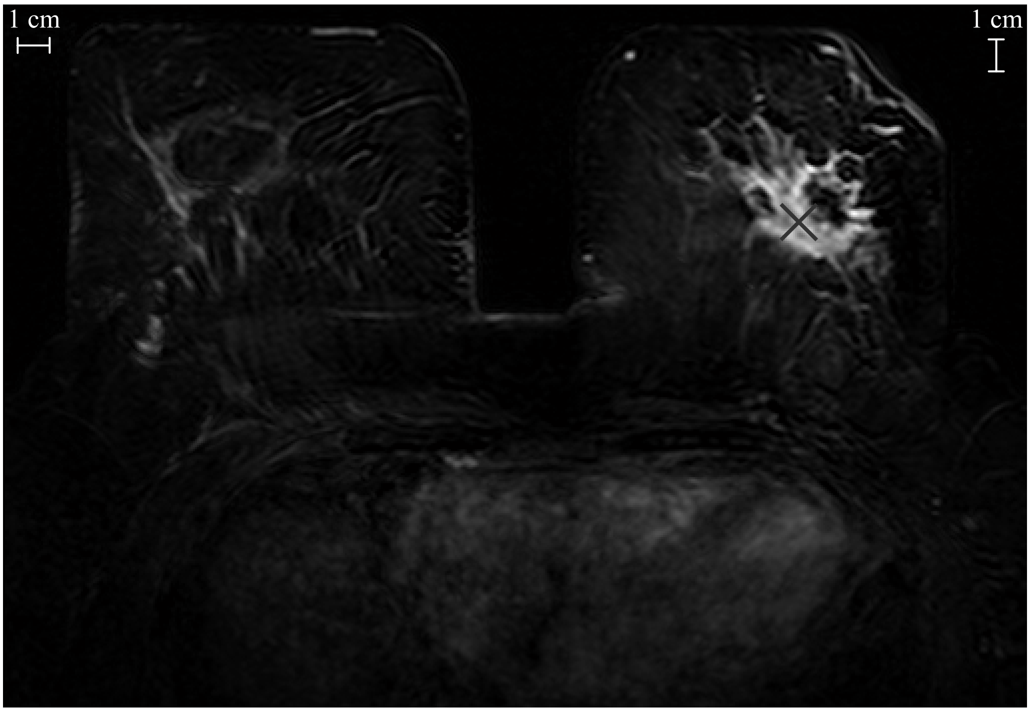

(b)

Figure 4.4 Representative slice stack (slice 18) for a 41-year old woman with an irregular malignant lesion. (a) Pre-contrast axial breast image with superimposed automatically segmented breast region as a contour overlay, (b) maximum intensity image ("×" indicates the lesion center), (c) computed nMITR map for the whole slice, (d) Figure 4.4c after masking with the segmented breast region, (e) output after 3D template matching, (f) suspiciously enhancing regions detected after thresholding.

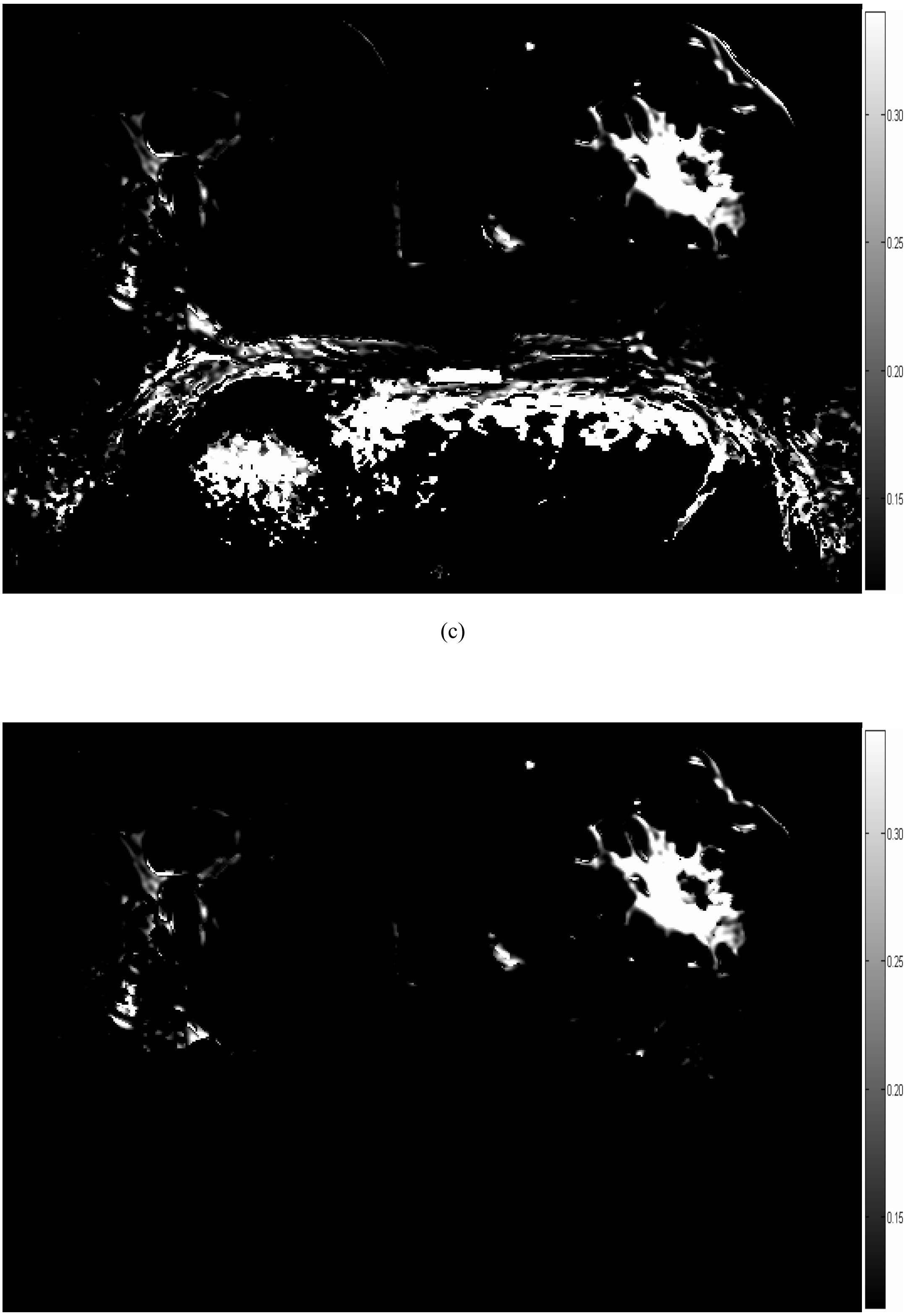

(c)

(d)

Figure 4.4 Continued.

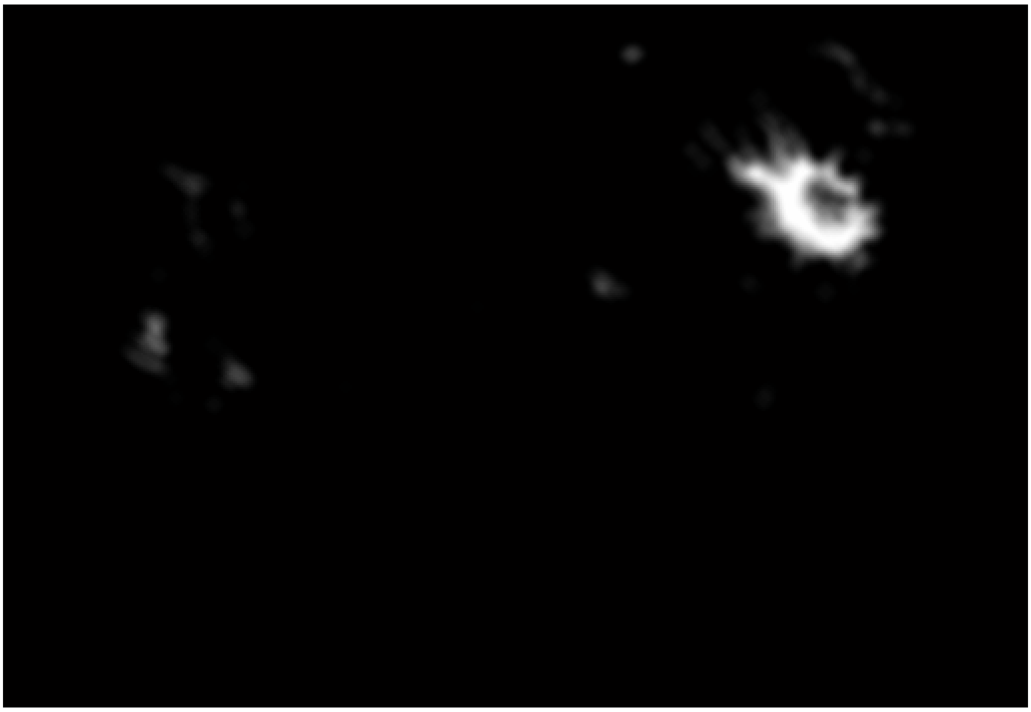

(e)

(f)

Figure 4.4 Continued.

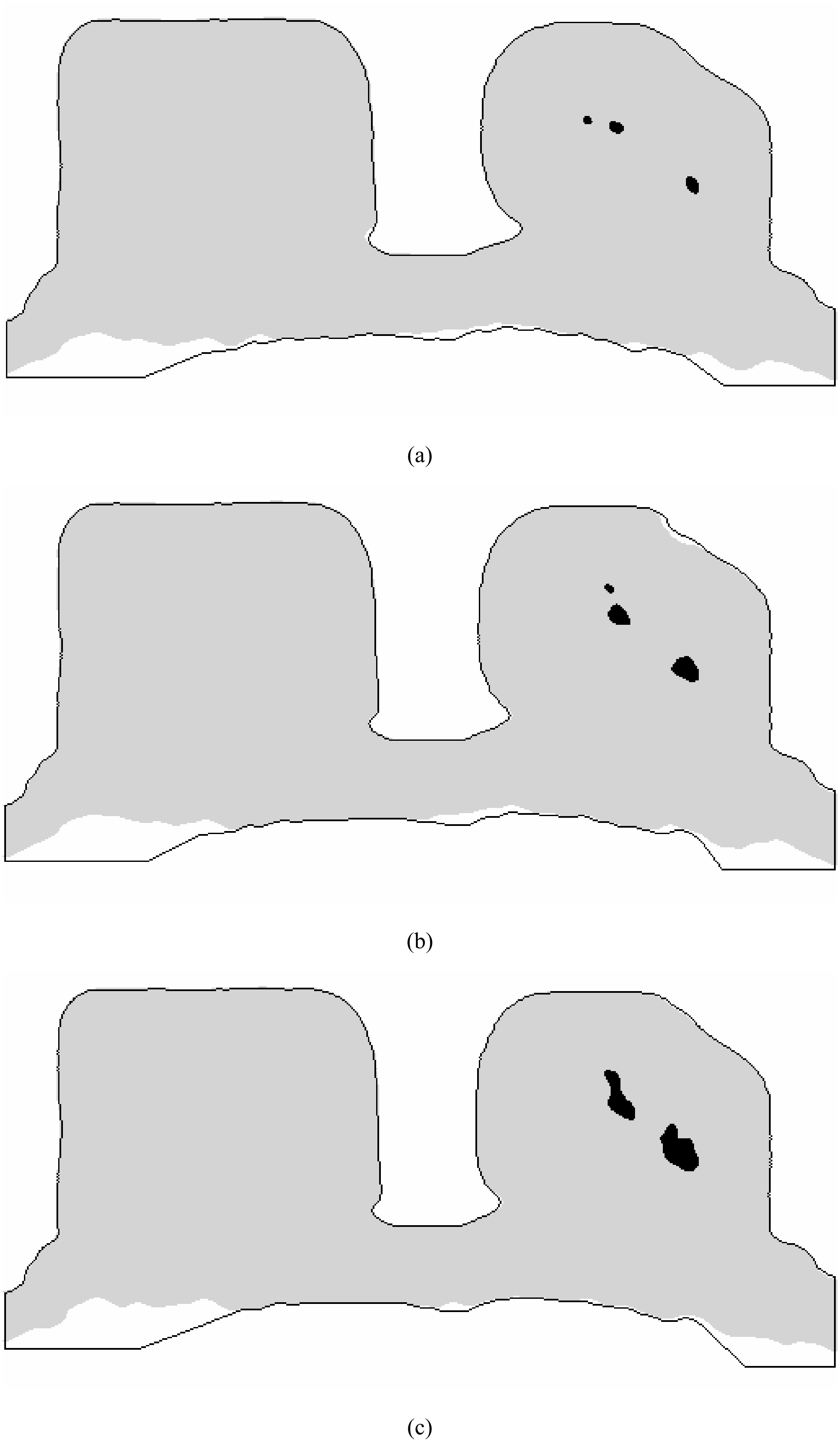

(a)

(b)

(c)

Figure 4.5 Breast region manually delineated by the expert (solid black contour), the region segmented automatically (gray colored area) and the lesion detected by the system (black colored area). (a-m) Slices 13 to 25.

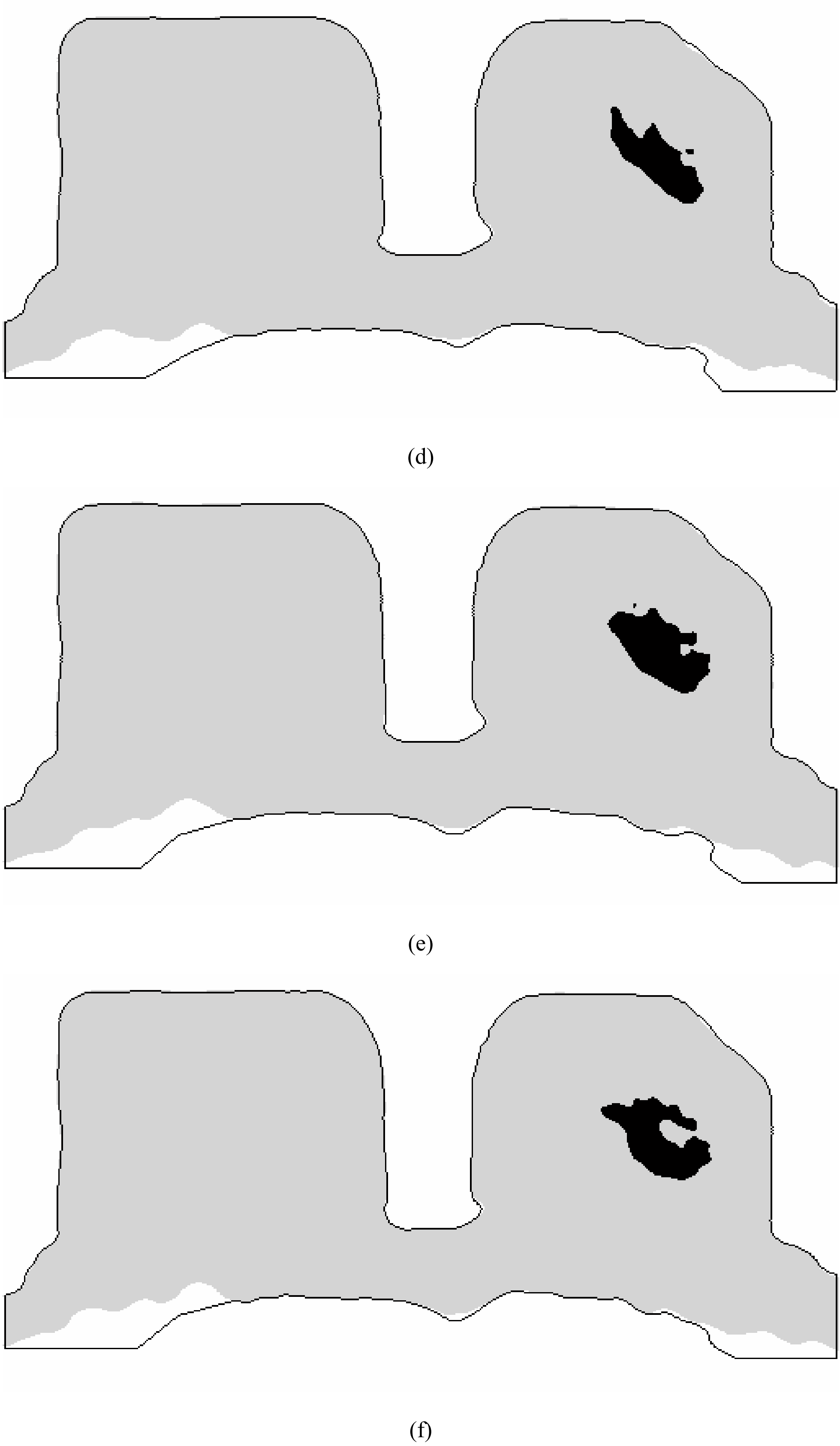

(d)

(e)

(f)

Figure 4.5 Continued.

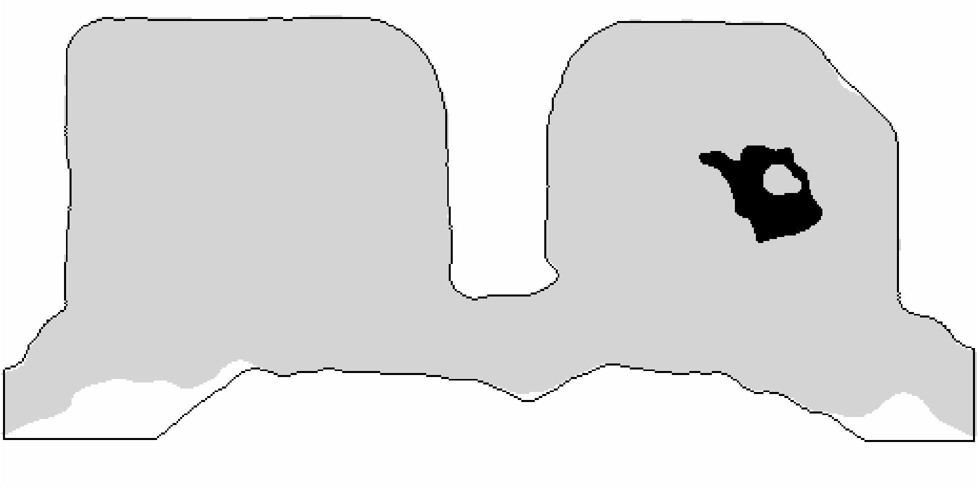

(g)

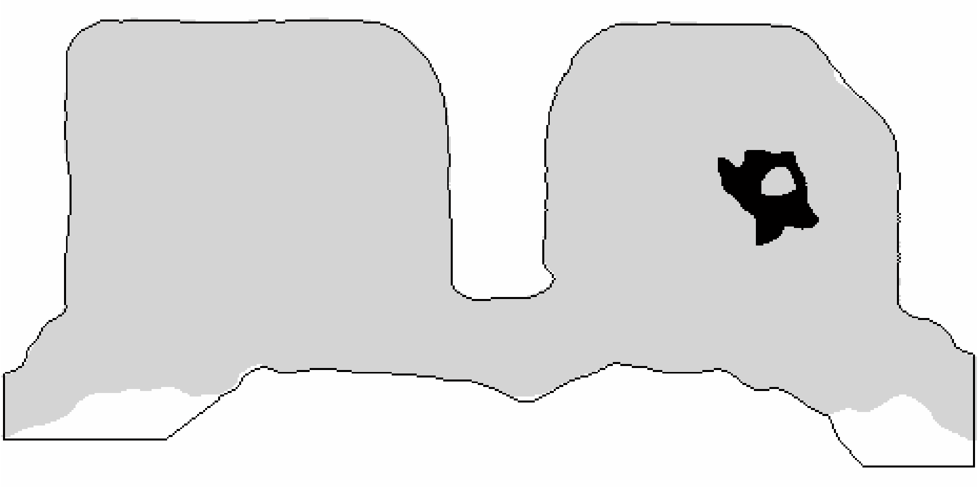

(h)

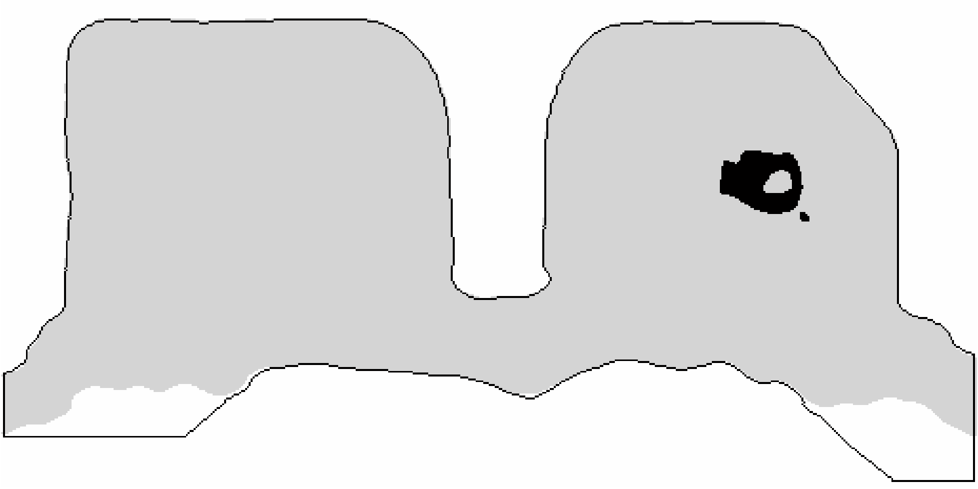

(i)

Figure 4.5 Continued.

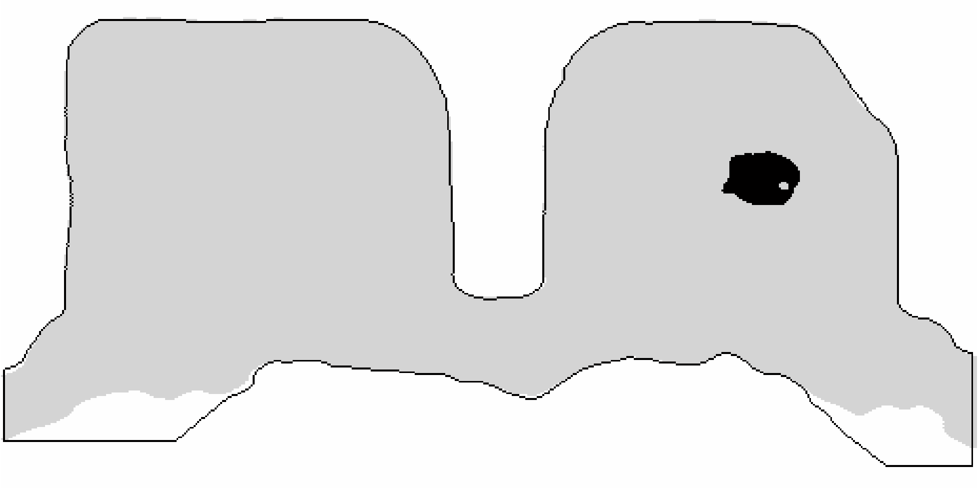

(j)

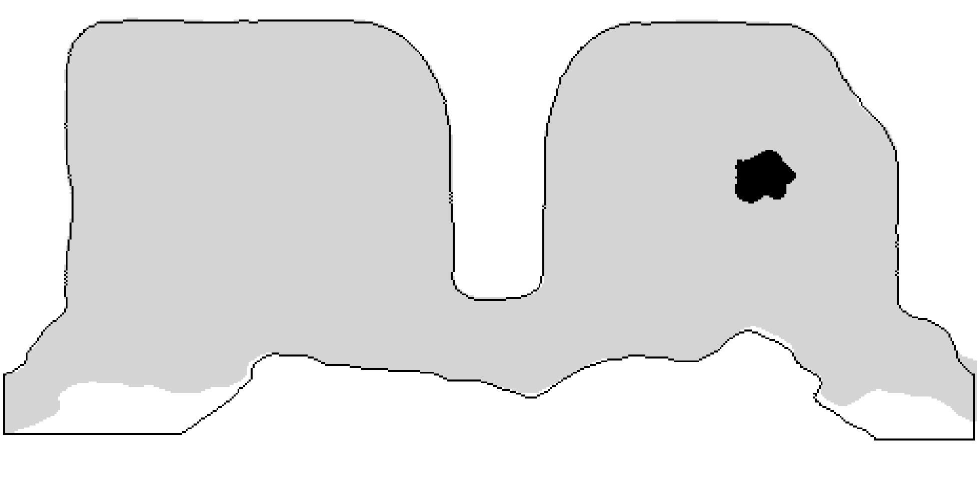

(k)

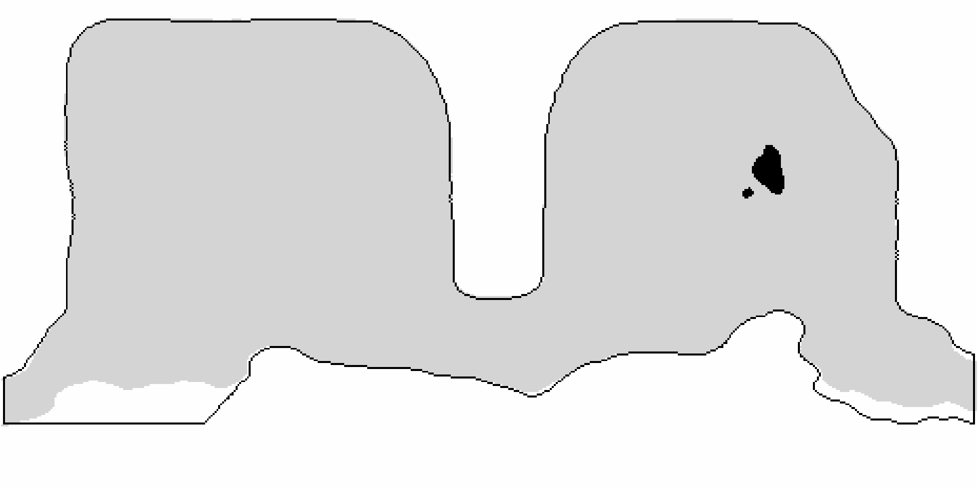

(l)

Figure 4.5 Continued.

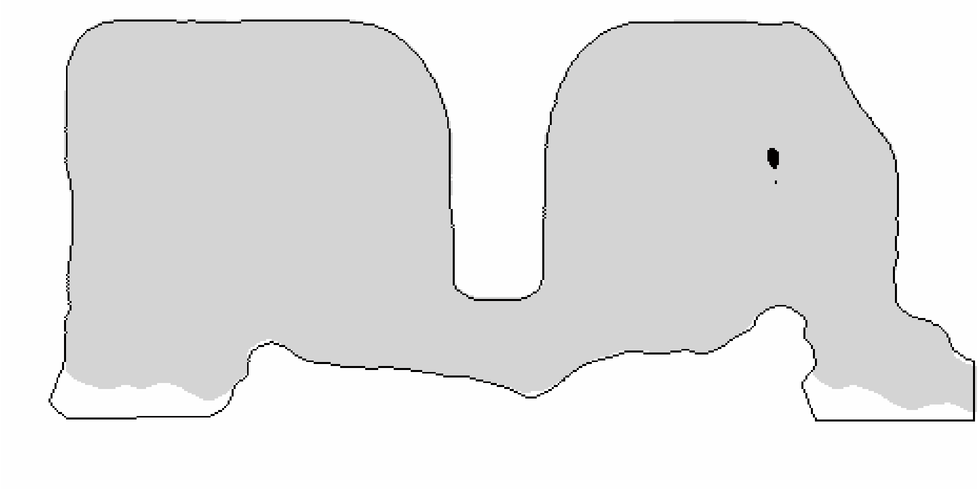

(m)

Figure 4.5 Continued.

The system was tested using a dataset consisting of 2064 high-resolution axial images in 344 slices, each containing one pre-contrast and five post-contrast axial MR mammograms from 19 patients with 20 malignant and 19 benign lesions marked by experts. 97% of the breasts were segmented properly and all the lesions were detected correctly (i.e., 100% detection sensitivity). Due to segmentation artifacts and a number of large-diameter blood vessels, there were some false-positive detections (31%/lesion, 10%/slice). These statistics suggest that this system may be used to facilitate detection of lesions in DCE-MR mammograms.

4.8 Conclusion

Due to the limitations and the ionizing nature of X-ray mammography there is a growing interest in the use of contrast enhanced dynamic MR mammography for breast cancer diagnosis. Since the number of acquired and constructed images for DCE-MRM is too many, qualitative evaluation is a time consuming process and requires great deal of experience. Missing of minute details may result in poor specificity and sensitivity in the final diagnosis. Therefore, quantitative methods are being developed to aid radiologists.

These methods require manually marked regions of interests which is also a time-consuming process.

In this chapter, we introduce a fully automated 3D lesion detection system for bilateral, axial DCE-MR mammograms. The system does not require prior knowledge concerning breast anatomy such as chest wall flatness, prior mastectomy history. Breast regions in the images are extracted by a segmentation scheme based on cellular neural networks. The performance of the segmentation is quantified using two metrics; relative overlap and misclassification rate. Segmentation with CNNs is very effective and is an alternative method to perform morphological operations. A CNN based system can be realized either by software that runs on a digital computer, or by a dedicated hardware that uses special CNN chips. When implemented in such a dedicated hardware, very high throughputs can be achieved and images can be processed in (almost) real-time.

For the segmented breast, using a moving ROI of 3×3 voxels, a 3D nMITR map is generated. To identify suspicious enhancements and to remove (deceptively enhanced) fatty tissue, muscles and normal parenchyma, this map is converted into a binary form employing a carefully selected threshold. The resultant map is then processed with a 3D template of three layers of 12×12 cells using a convolution-like operation. This operation is quite similar to what radiologists do for lesion detection; they mentally use templates based on their experience and evaluations of lesion anatomies. The template is so designed that it can detect small or large lesions with different shapes. At the end of the template processing, volumes geometrically similar to the template become enhanced. To detect breast lesions, the convolution result is passed from a threshold that yields a similarity of 47%. A lower value will result in increased false positive detections due to enhanced blood vessels, while higher values will result in missed lesions.

To our knowledge, there are no publications on computerized methods that focus solely on DCE-MRM lesion detection. Bian et al [13] seem to be working on this topic and in a recent abstract reported their initial results. When tested on a dataset consisting of 20 cases with 21 lesions, their method correctly detected 16 of the lesions and on average, there were 9 false-positive detections per case (see the footnote on page 149). These findings correspond to a detection sensitivity of 76% and a false-positive detection rate per lesion of 857%. In comparison, the performance of our system is better (detection sensitivity = 100%, false-positive detection rate per lesion = 31%).

Proper segmentation of the breast is vital for the success of the system. There are cases in which segmentation may not be very accurate, especially for fat patients. Since intensities are reduced further away from the breast coil, segmentation may end inappropriately within the axilla at an arbitrary edge, leading to false negative detections. When there is a suspected lesion within the axilla, due to its better coverage, sagittal imaging should be used to minimize problems.

Patient motion can lead to serious diagnostic complications as a result of misalignments of the image sequences during acquisition of contrast-enhanced MR mammograms. Several image registration techniques have been proposed that attempt to solve this difficult problem [102, 103, 104, 105]. Although the present system does not include a dedicated motion correction scheme, it is inherently capable of compensating small motion artifacts due to the averaging nature of the nMITR maps.

During 3D template matching there may be some loss of morphological information. This loss of is tolerable in the current system since it is intended only for localizing lesions. This localization information can later be used as a guide for more accurate lesion segmentation that preserves morphology for malignancy discrimination.

The system is capable of distinguishing deceptive enhancements due to blood vessels that make evaluations difficult and time-consuming. Moreover, the system has the potential of facilitating detection of multifocality and multicentricity; an important issue since presence of multicentricity is highly correlated with cancer re-occurrence. We hope that its use in clinical practice and for surgical planning will result in a decrease in the number of unnecessary mastectomies and a reduction in mortality.

This study is a preliminary search into computerized detection of lesions using nMITR maps of DCE-MR mammograms. We need to point out that the results presented here are far from complete. There are still many problems waiting further exploration and room for improvements: Classical optimization techniques or genetic algorithms may be used to compute optimal patient-specific template parameters and thresholds; 3D CNNs can be used for lesion detection to minimize computational costs; false positive findings due to blood vessels and segmentation problems may be further reduced through 3D morphological and enhancement analysis and the system can be equipped with discrimination capabilities based on dynamic and morphological features.

5. IMPROVED LESION LOCALIZATION WITH FUZZY C-PARTITIONING

5.1 Introduction

X-ray mammography is the conventional screening tool used to detect breast cancer in its early stage. Due to reported false-negative rates that may be as high as 34% [46], limitations on dense breasts, ionizing nature, overlapping structures, summation shadows and patient discomfort during breast compression, contrast-enhanced magnetic resonance mammography (CE-MRM) is gaining increased acceptance as an adjunct tool [106]. In CE-MRM, additional information supplied by the enhancements that reflect vascularity and permeability of the relevant tissues lead to superior detection and classification of breast cancers and to higher positive predictive values when compared to X-ray mammography [107]. For improving interpretation accuracy and reproducibility further, recent analysis strategies use semi-automatically selected region of interests (ROIs) to detect lesions and to extract quantitative enhancement and/or morphologic descriptors.

Tzacheva et al [20] developed a semi-automated 2D lesion detection algorithm for the assessment of morphological features of breast lesions. The algorithm applies user-controlled intensity thresholding followed by binary conversation on a single post-contrast sagittal fat suppressed T_1-weighted image of the breast in which the lesion is present. The processed images have intensity values ranging between 0 and 255. Liney et al [21] defined a similar method based on intensity thresholding using fat suppressed T_1-weighted breast images. Deurloo et al [84] proposed the use of an automated method in three dimensions after a point in the lesion designated manually on the first post contrast subtraction image by the radiologist. For 3D detection of lesions from contrast enhanced MR mammograms, Chen et al [85] developed a method based on Fuzzy c-means clustering (FCM). Radiologist first selects an ROI; FCM is applied next on the enhancement values calculated for the ROI. Membership map is then binarized and lesion is detected after connected-component labeling, object selection, and hole-filling.

In all the studies mentioned above, user guidance is necessary; the user must mark the ROI and select a point inside the lesion or an intensity threshold value. Considering the acquired and constructed images for CE-MRM, the radiologist has to visually inspect hundreds of images. Missing of a very small detail may result in poor specificity and sensitivity in the final diagnosis. Moreover, normal regions that appear deceptively enhanced due to vascularizations, especially in premenopausal women make the task complicated. To facilitate overall analysis, visualization of suspiciously enhancing regions has been improved by recent computerized systems that provide color coded parametric maps of enhancements [4-7]. However, these systems still rely on qualitative assessment of enhancing lesion volumes which is subjective, erroneous, highly observer-dependent and time-consuming. There is a need for automated detection and estimation of lesion volumes. A number of computerized techniques have been developed for use in diagnostic breast imaging, such as for X-ray mammography [8, 9], sonography [10], tomosynthesis [11] and computed tomography [12]. To our knowledge, for CE-MRM, only Bian et al [13] reported a fully automated lesion localization technique. This technique consists of four consecutive stages: breast volume segmentation based on a volume growing method, fuzzy c-means clustering analysis on voxel-based enhancements within the 3D breast image data, voxel-by-voxel membership assignment to the most-enhancing categories and connectivity and size criteria for eliminating some false-positive detections (see the footnote on page 149).

In the present study, we introduce a novel, robust and accurate method for improved lesion localization based on the use of cellular neural networks (CNNs). The proposed scheme employs four coupled 2D CNNs connected in cascade to segment the breast region of interest from pre-contrast images. For the segmented tissues, relative enhancements are computed and a 3D normalized maximum intensity-time ratio (nMITR) map is generated. This map is converted into binary form using a thresholding operation and processed by a 3D CNN with a fuzzy c-partitioning output function to boost lesions and to eliminate moderately enhanced normal parenchyma, fat and blood vessels. Suspicious regions in the resultant map are pre-localized through volumetric 6-neighborhood connectivity search. A set of decision rules extracted from volume and 3D eccentricity features are used finally to decide whether these pre-localized regions are lesions. This further reduces possible false detections due to artifacts caused by highly enhanced normal tissue, such as blood vessels, nipples and normal parenchyma and due to chest-wall artifacts caused by over segmentation.

5.2 Imaging Protocol

Magnetic resonance imaging is performed on a 1.5 Tesla MR scanner (Magnetom Symphony, Siemens Medical Systems, Erlangen, Germany) equipped with a dedicated four-element phased-array receiver breast coil. Patients are positioned prone with the breast to be imaged in gentle compression within the coil to minimize motion artifacts. The imaging sequence is 3D fast low angle shot (FLASH) (TR/TE 9.80/4.76 msec, flip angle 25^o, matrix size 512×512, slice thickness 2.5 mm, $0.625\times0.625mm^2$ in-plane resolution). During and immediately after the bolus injection of contrast agent Gd-DTPA (0.1 mmol/kg body weight), one pre-contrast and five post-contrast high-resolution bilateral axial images are acquired per slice with a temporal resolution of approximately 88 seconds. 12-bit grayscale image sets are transferred from the MR scanner to a personnel computer in DICOM format for further analysis using Matlab 7.0 (The Mathworks Inc, Natick, MA, USA).

5.3 Patient Population and Image Dataset

Thirty-nine women (age range, 32-83 years; mean age, 48.4 years) were retrospectively entered into this study. The nature of the imaging procedure was explained to all the patients considered in this study and their consents were secured. For each breast MR examination, 180 images corresponding to 30 slices were analyzed. A total of 76 mass lesions (39 benign and 37 malignant) ranging in size between 0.14 cm^3 and 17.23 cm^3 were marked by two experienced radiologists on the slices by mutual agreement. All the findings were supported either by histopathological examination or by clinical follow-up. From this data, a training dataset was formed that included 21 benign and 25 malignant lesions. The remaining data consisting of 18 benign and 12 malignant lesions was used as the test dataset.

5.4 Image Processing using Cellular Neural Networks

Image processing involves combinations of highly complicated mathematical operations that may include a variety of transformations, convolutions, statistical computations, smoothing, filtering, pattern recognition, etc. Computational burden of many of these operations are far greater than that can be handled within practical time limits by existing sequential machines having Von-Neuman architecture. This burden can be “eased-out” by distributing the workload using parallel designs. In fact, Chua in 1988, introduced Cellular Neural Networks (CNNs), which are massively parallel cellular structures with learning abilities [108]. Due to their extremely high throughputs, CNNs offer almost real-time solutions to complex image processing applications [109, 110]. For example, using hardware CNN implementation basic morphological operations can be completed within 1μs, independent of image size and structuring elements [90].

In medical image processing, CNNs have been used by various investigators (for a good review see Aizenberg et al [95]). Rekeczky et al [91] have shown feasibility of CNN based real-time feature extraction from echocardiographic images. Zarandy et al [92] have used a CNN to analyze X-ray mammograms. Girodana et al [93] have proposed a CNN based technique for fast and accurate detection of craniofacial landmarks on X-ray images. Shitong et al [94] have studied automated white blood cell detection methods using microscopic blood images and showed that the CNN based method works better when compared with the existing two methods: threshold segmentation followed by mathematical morphology and the fuzzy logic method. Zhang et al [111] have automated the detection of small-size pulmonary nodules from computed tomography images with a CNN based scheme.

A discrete-time CNN can be defined by an array of locally interconnected cells. Consider a 3D $L \times M \times N$ image and a cell located at position (*i, j, k*), $i = 1,\ 2, ..., L$, $j = 1,\ 2, ..., M$, $k = 1,\ 2, ..., N$. The *r*-neighborhood of the cell located at position (*i, j, k*) is defined by:

$$N_{i,j,k}\left(r\right) = \left\{ (l,m,n) \,\middle|\, \max(|\,i-l\,|,|\,j-m\,|,|\,k-n\,|) \le r;\ 1 \le l \le L,\ 1 \le m \le M,\ 1 \le n \le N \right\} \tag{5.1a}$$

where r is a positive integer. The output $y_{i,j,k}(t)$ and the state $x_{i,j,k}(t)$ at step $t = 1,2,3...$ can be written as [90]:

$$y_{i,j,k}(t) = 0.5 \times \left\{ \left| x_{i,j,k}(t-1)+1 \right| - \left| x_{i,j,k}(t-1)-1 \right| \right\}, \; x_{i,j,k}(0) = \chi_{i,j,k} \tag{5.1b}$$

$$x_{i,j,k}(t) = \sum_{(l,m,n) \in N_{i,j,k}(r)} A_{l,m,n} \times y_{i+l,j+m,k+n}(t) + \sum_{(l,m,n) \in N_{i,j,k}(r)} B_{l,m,n} \times u_{i+l,j+m,k+n} + b \tag{5.1c}$$

where $u_{i,j,k}$ is the input, $A_{l,m,n}$ and $B_{l,m,n}$ are the entries at the *l,m,n*-th neighborhood of the feedback and control templates and b is a constant bias parameter. The magnitudes of the input $u_{i,j,k}$ and the initial state $x_{i,j,k}(0) = \chi_{i,j,k}$ are less than or equal to one. For a 2D network, the third index k can be dropped. Note that the template A operates in a feedback loop along with a nonlinearity and that template B forms a simple feed-forward finite impulse response filtered version of the input. Although a number of templates have been reported for some basic image processing [92, 97, 112], depending on the application, they may not be directly usable and some modifications may be necessary. The templates used in the present thesis are discussed in the following sections.

5.5 Segmentation of Breast

A typical bilateral axial breast MR image includes several regions that are out of interest such as chest muscles, heart, lungs and thoracic cavity. To reduce false positive detections from these regions, segmentation of the breast region is a necessity for any computerized lesion localization technique. The breast region can be segmented as the middle section between breast-air and breast-chest wall boundaries.

Air produces a near-zero image intensity so that the breast-air boundary may be identified by simply searching a sharp increase in the intensity of the mammogram. However, due to the intensity inhomogeneity artifacts and the presence of muscles near the chest wall, breast-chest wall boundary detection is a complicated problem. Hayton et al [86] developed a method based on morphological operations (iterative morphological erosion followed by dilation) and graph search to find an approximate location of the chest wall on the pre-contrast images. For certain patients, the algorithm generates satisfactory results but it requires a long process time and fails if the patient's chest is not flat. Twellmann et al [87] proposed a simple technique that applies median filtering, gray-level based histogram thresholding and morphological operations on pre-contrast images. However, it may fail to segment breast tissues close to the chest wall, most probably, due to the used thresholding method. Wenzhu et al [113] discussed a method that uses mathematical morphology and region growing to locate breast-air boundary and active contour model to locate breast-chest boundary from pre-contrast images. The performance of the algorithm depends on appropriate selection of field of view (FOV) and makes several assumptions such as locations of the axilla, mid-sternum and nipples. It may not work properly especially if the patient has prior mastectomy.

In this study, for breast segmentation we use four specially designed 2D CNNs connected in cascade. This segmentation technique is robust and does not require prior information concerning breast anatomy and FOV. The initial state of the first net, CNN_T are the intensity values of pre-contrast MR image, normalized to be between -1 and +1. This net is used for gray-level thresholding; its output is processed by the second net, CNN_O. CNN_O performs binary morphological image closing, removes small objects and smoothes out sharp corners. Although the performance of this net is reasonably good in segmenting target tissues, inhomogeneity artifacts may lead to falsely segmented regions from the chest wall, lung and the heart. Therefore, two additional nets; CNN_E and CNN_R are used to perform morphological image erosion followed by image reconstruction. Thus irrelevant regions are removed and the biggest breast region of interest is detected.

Although, in the literature [92, 97, 112], a number of templates have been reported for the tasks undertaken by CNN_T, CNN_O, CNN_E and CNN_R, direct use of these templates in the present application lead to serious segmentation artifacts. To minimize these artifacts template A in CNN_O was modified by adding two extra rows and two extra columns and the bias parameter b in CNN_T was changed to 0.79. A summary of the templates used in segmentation are presented in Table 5.1.

Table 5.1
Parameter values of the CNNs used.

	Input	Initial State	**A**	**B**	*b*
CNN_T CNN for Gray-level thresholding *(r=1)*	0	Normalized pre-contrast image	$\begin{bmatrix} 0 & 0 & 0 \\ 0 & 2 & 0 \\ 0 & 0 & 0 \end{bmatrix}$	$\begin{bmatrix} 0 & 0 & 0 \\ 0 & 0 & 0 \\ 0 & 0 & 0 \end{bmatrix}$	0.79
CNN_O CNN for erasing small objects *(r=2)*	0	Thresholded pre-contrast image	$\begin{bmatrix} 0 & 0 & 0 & 0 & 0 \\ 1 & 1 & 1 & 1 & 1 \\ 1 & 1 & 0 & 1 & 1 \\ 1 & 1 & 1 & 1 & 1 \\ 0 & 0 & 0 & 0 & 0 \end{bmatrix}$	$\begin{bmatrix} 0 & 0 & 0 & 0 & 0 \\ 0 & 0 & 0 & 0 & 0 \\ 0 & 0 & 0 & 0 & 0 \\ 0 & 0 & 0 & 0 & 0 \\ 0 & 0 & 0 & 0 & 0 \end{bmatrix}$	0
CNN_E CNN for morphological erosion *(r=1)*	0	Small objects erased pre-contrast image	$\begin{bmatrix} 0 & 0 & 0 \\ 0 & 1 & 0 \\ 0 & 0 & 0 \end{bmatrix}$	$\begin{bmatrix} 0 & 1 & 0 \\ 1 & 1 & 1 \\ 0 & 1 & 0 \end{bmatrix}$	-4.00
CNN_R CNN for breast mask reconstruction *(r=1)*	Small objects erased pre-contrast image	Eroded and small objects erased pre-contrast image	$\begin{bmatrix} 0 & 1 & 0 \\ 1 & 2 & 1 \\ 0 & 1 & 0 \end{bmatrix}$	$\begin{bmatrix} 0 & 0 & 0 \\ 0 & 2 & 0 \\ 0 & 0 & 0 \end{bmatrix}$	2.50

The stopping criteria for these nets are defined as follows:

CNN_T: After each iteration, the voxel values change towards either +1 or -1, except those selected by the bias value. This change will eventually go towards zero as the process stabilizes. Therefore, the iteration is stopped when the total number of voxel intensity remains unchanged from iteration to iteration.

CNN$_O$: In this case, the image to be processed is binary (i.e., black-and-white). The iteration is stopped if there is no difference between the voxel intensities after eight consecutive iterations; it is also stopped if this criterion cannot be met within 200 iterations.

CNN$_E$: The binary image is eroded until the total number of white voxels is reduced by 50%.

CNN$_R$: The breast mask is reconstructed until there is no difference between the voxel intensities after eight consecutive iterations.

5.6 Lesion Localization

To distinguish deceptively enhancing regions from lesions in clinical practice, radiologists mentally make use of enhancement properties and lesion anatomy; in this study, we follow a similar approach using a fifth net with a fuzzy c-partitioning based output function. Unlike the previous nets, this net *CNN$_L$* is a 3D net and is used for detecting suspiciously enhancing regions. The inputs of this net are the normalized maximum intensity-time ratio (nMITR) maps, generated as described below: Consider the (*i,j,k*)-*th* voxel of an image inside the segmented breast. The mean $\overline{I}_{i,j,k}(v)$ of (2D) 1-neighborhood intensity ($r = 1$) values $I_{i,j,k}(v)$ of the pre-contrast image ($v = 0$) and the post-contrast images ($v = 1, 2, \cdots, 5$) is computed as

$$\overline{I}_{i,j,k}(v) = \frac{1}{9} \times \sum_{l=-1}^{1} \sum_{m=-1}^{1} I_{i+l,j+m,k}(v) \tag{5.2a}$$

The normalized enhancement is defined by [54]:

$$E_{i,j,k}(v) = \frac{\overline{I}_{i,j,k}(v) - \overline{I}_{i,j,k}(0)}{\overline{I}_{i,j,k}(0)} \times 100, \quad v \neq 0 \tag{5.2b}$$

Now let $\max\left\{E_{i,j,k}(v)\right\}$ be the maximum normalized enhancement and let T_{max} be the time in seconds when the maximum is reached. The *(i,j,k)-th* voxel of the nMITR map is defined as [34]:

$$nMITR_{i,j,k} = \frac{\max\left\{E_{i,j,k}(v)\right\}}{T_{\max}} \tag{5.2c}$$

Performing the above computations for the whole images a 3D nMITR map is generated. These values are passed through a fixed threshold (TH_1) to obtain a binary image:

$$R_{i,j,k} = \operatorname{sgn}\left\{nMITR_{i,j,k} - TH_1\right\} \tag{5.3}$$

where $\operatorname{sgn}(\cdot)$ represents the signum function. For the dataset used in the present work, this threshold is $TH_1 = 0.33\ \text{sec}^{-1}$; it is chosen so that, after thresholding, only tissue that show 20%, 40%, 158% and higher maximum enhancements at 1, 2 and 8 minutes after contrast agent administration remains in the processed image, respectively. This way, fatty tissues and other moderately enhanced normal tissues such as blood vessels, parenchyma and muscles are eliminated.

CNN_L processes $R_{i,j,k}$ as the input to localize suspiciously enhancing regions. This net uses 5-neighborhood ($r = 5$) and has a $11\times11\times3$ control template as given in Eqs. 5.4.a and 5.4b. It is assumed that the template entries are zero at undefined locations. Regions geometrically similar to the template become enhanced after a single iteration. When the template and the region under examination have no common voxels, the final state will reach its minimum of -274. On the other hand, when the voxels within the template and the region under examination are all common, it will reach its maximum of +274. The output of CNN_L is calculated using Eq. 5.4c.

$$\left[B_{l,m,0}\right]=\begin{bmatrix}0&0&0&0&1&1&1&0&0&0&0\\0&0&0&1&1&1&1&1&0&0&0\\0&0&1&1&2&2&2&1&1&0&0\\0&1&1&2&2&2&2&2&1&1&0\\1&1&2&2&2&2&2&2&2&1&1\\1&1&2&2&2&2&2&2&2&1&1\\1&1&2&2&2&2&2&2&2&1&1\\0&1&1&2&2&2&2&2&1&1&0\\0&0&1&1&2&2&2&1&1&0&0\\0&0&0&1&1&1&1&1&0&0&0\\0&0&0&0&1&1&1&0&0&0&0\end{bmatrix} \tag{5.4a}$$

$$\left[B_{l,m,-1}\right]=\left[B_{l,m,+1}\right]=\begin{bmatrix}0&0&0&0&0&0&0&0&0&0&0\\0&0&0&0&1&1&1&0&0&0&0\\0&0&0&1&1&1&1&1&0&0&0\\0&0&1&1&2&2&2&1&1&0&0\\0&1&1&2&2&2&2&2&1&1&0\\0&1&1&2&2&2&2&2&1&1&0\\0&1&1&2&2&2&2&2&1&1&0\\0&0&1&1&2&2&2&1&1&0&0\\0&0&0&1&1&1&1&1&0&0&0\\0&0&0&0&1&1&1&0&0&0&0\\0&0&0&0&0&0&0&0&0&0&0\end{bmatrix} \tag{5.4b}$$

$$y_{i,j,k}(t)=\operatorname{sgn}\left\{x_{i,j,k}(t-1)-TH_2\right\},\ \ x_{i,j,k}(0)=0 \tag{5.4c}$$

This equation differs from Eq. 5.1b; it depends on a threshold TH_2 which is determined adaptively for each patient using the maximum entropy principle and fuzzy c-partitioning [114]. To minimize artifacts from very small regions of normal tissues that show high enhancements, final state values within the range -150 to +274 are considered only and mapped into a single dimensional array s.

Spline-based membership function of a potential lesion $\mu_l(s,a,c)$ and the membership function of normal tissues that show high enhancement (and thus likely to cause false detection) $\mu_f(s,a,c)$ are defined as:

$$\mu_l(s,a,c)=\begin{cases} 1, & s \le a \\ 1-2\left(\dfrac{s-a}{c-a}\right)^2, & a < s \le \dfrac{a+c}{2} \\ 2\left(\dfrac{c-s}{c-a}\right), & \dfrac{a+c}{2} < s < c \\ 0, & s \ge c \end{cases} \tag{5.5a}$$

$$\mu_f(s,a,c)=\begin{cases} 0, & s \le a \\ 2\left(\dfrac{s-a}{c-a}\right)^2, & a < s \le \dfrac{a+c}{2} \\ 1-2\left(\dfrac{c-s}{c-a}\right)^2, & \dfrac{a+c}{2} < s < c \\ 1, & s \ge c \end{cases} \tag{5.5b}$$

In Eqs. (5.5a-5.5b) a and c are parameters that determine the extremes of the sloped portion of the membership functions; TH_2 is the arithmetic mean of the "optimal" values of these parameters, $\hat{a}$ and $\hat{c}$:

$$TH_2 = \frac{\hat{a}+\hat{c}}{2} \tag{5.5c}$$

$\hat{a}$ and $\hat{c}$ are obtained from the fuzzy 2-partition that has the maximum entropy. This partition is determined through an exhaustive search. The probabilities of the fuzzy events, $P_l(a,c)$, $P_f(a,c)$ and the entropy of the specified partition, $H(a,c)$ are calculated in terms of the probability of the occurrence of s, $\Pr(s)$ using:

$$P_l(a,c) = \sum_{s=-150}^{274} \mu_l(s,a,c)\Pr(s) \tag{5.5d}$$

$$P_f(a,c) = \sum_{s=-150}^{274} \mu_e(s,a,c)\Pr(s) \tag{5.5e}$$

$$H(a,c) = -P_f(a,c)\times\log\left(P_f(a,c)\right) - P_l(a,c)\times\log\left(P_l(a,c)\right) \tag{5.5f}$$

5.7 Elimination of False-Positive Detections

The output of *CNN$_L$* cannot be used directly for lesion detection because normal tissue, such as blood vessels, nipples and normal parenchyma that appear as highly enhanced regions in the dynamic mammograms may leave many artifacts that could result in false detections. Moreover, over segmentation problems may cause similar artifacts from vascularized tissues in the chest-wall. Therefore, it is very important to discriminate such regions carefully. To do this, objects in this binary image are identified by a volumetric 6-neighborhood connectivity search and volume and 3D eccentricity criteria are used to decide whether suspicious regions are indeed lesions, as explained next.

The moment of order ($p_i + p_j + p_k$) of a binary 3D object, imaged with a scanner whose slice thickness is r_k and resolutions in the horizontal and the vertical directions are r_i and r_j is defined as:

$$m_{p_i p_j p_k} = \sum_{i,j,k} \left(r_i \times i\right)^{p_i} \times \left(r_j \times j\right)^{p_j} \times \left(r_k \times k\right)^{p_k} \times f_{i,j,k} \tag{5.6}$$

where $f_{i,j,k}$ is an indicator function which is one if the voxel (i, j, k) is inside the object and zero otherwise. Eq. 5.6 is modified from [115] and considers anisotropic nature of image resolutions. Note that the volume of the object can be computed in terms of the moments as $V = (r_i \times r_j \times r_k) \times m_{000}$ and the centroid $g = (g_i, g_j, g_k)$ as $g_i = m_{100} / m_{000}$, $g_j = m_{010} / m_{000}$ and $g_j = m_{010} / m_{000}$. We define 3D eccentricity, Ecc as:

$$Ecc = \sqrt{1 - \frac{d_{\min}^2}{d_{\max}^2}} \tag{5.7a}$$

where $d_{\min}$ and $d_{\max}$ represent the lengths along the principal directions that correspond to the minimum and the maximum eigenvalues of the normalized second order central moment matrix η:

$$\eta = \frac{1}{m_{000}} \times \begin{bmatrix} \mu_{200} & \mu_{110} & \mu_{101} \\ \mu_{110} & \mu_{020} & \mu_{011} \\ \mu_{101} & \mu_{011} & \mu_{002} \end{bmatrix} \tag{5.7b}$$

In the above expression $\mu_{p_i p_j p_k}$ represents the central moment:

$$\mu_{p_i p_j p_k} = \sum_{i,j,k} \left(r_i \times i - g_i\right)^{p_i} \times \left(r_j \times j - g_j\right)^{p_j} \times \left(r_k \times k - g_k\right)^{p_k} \times f_{i,j,k} \tag{5.7c}$$

Eccentricity is a quantity that ranges from 0 (round) to 1 (elongated); it is invariant to translation, orientation and scale change and can be adoptable to different scanners with different imaging resolutions. Since blood vessels are more elongated than lesions of similar sizes, in the present study, eccentricity is used to distinguish blood vessels from lesions.

Through extensive experimentation on the training dataset, we have come up with the following decision rules for identifying lesions:

Rule 1: A suspicious region is *not* a lesion if $V < 0.08\ \text{cm}^3$.

Rule 2: A suspicious region is a lesion if $0.08\ \text{cm}^3 < V < 1.00\ \text{cm}^3$ and $Ecc < 0.91$.

Rule 3: A suspicious region is *not* a lesion if $V \geq 1.00\ \text{cm}^3$ and $Ecc > 0.97$.

The above criteria have been shown to be very successful in reducing a great deal of problematic false detections due to artifacts caused by highly enhanced normal tissue, such as blood vessels, nipples and normal parenchyma and artifacts from vascularized tissues in the chest-wall due to over segmentation.

5.8 Performance Analysis

To determine the success of the automated breast segmentation, several metrics are computed based on C_s, the set of voxels within the breast region estimated by the CNN segmentation and C_r , the set of voxels delineated by manual correction of the segmentation. Let $C_{TP} = C_s \cap C_r$ and $C_{FP} = C_s - (C_s \cap C_r)$. The subscripts *TP* and *FP* stand for true positive and false positive. Segmentation precision *PR* (also called as relative overlap in [99]) is calculated using [100]:

$$PR(C_s, C_r) = \frac{n_{C_{TP}}}{n_{C_s \cup C_r}} \tag{5.8a}$$

$n_{\Re}$ denotes the total number of voxels within region $\Re$. [1]

Segmentation accuracy is assessed using true positive volume fraction *TPVF* (the fraction of total amount of voxels delineated by the radiologists that was covered by our method) and false positive volume fraction *FPVF* (the voxels falsely identified by our method as a fraction of the amount of the voxels in C_r). Clearly, the greater the *TPVF* and the smaller the *FPVF* values are, the better will be the accuracy. These parameters are computed using

$$TPVF(C_{TP}, C_r) = \frac{n_{C_{TP}}}{n_{C_r}} \tag{5.8b}$$

$$FPVF(C_{FP}, C_r) = \frac{n_{C_{FP}}}{n_{C_r}} \tag{5.8c}$$

---

[1] Note that in this work, to minimize the time required for manual segmentations, manual corrections to computerized segmentations are used as references. These segmentations are not "blind" to computer segmentations, and hence comparison of segmentation performance with methods that use "pure" manual segmentation is not entirely right. However, from experience we know that, for breast to air boundary, computerized segmentations and pure manual segmentations are almost the same.

The performance of the lesion detection is quantified by Se (sensitivity), FP_{slice} (false-positive rate per slice), FP_{lesion} (false-positive rate per lesion) and FP_{case} (false-positive rate per case) using [101]:

$$Se = \frac{Number\ of\ True\text{-}Positive\ Detections}{Number\ of\ Lesions} \tag{5.9a}$$

$$FP_{slice} = \frac{Number\ of\ Slices\ Containing\ False\text{-}Positive\ Detections}{Number\ of\ Slices} \tag{5.9b}$$

$$FP_{lesion} = \frac{Number\ of\ False\text{-}Positive\ Detections}{Number\ of\ Lesions} \tag{5.9c}$$

$$FP_{case} = \frac{Number\ of\ False\text{-}Positive\ Detections}{Number\ of\ Cases} \tag{5.9d}$$

5.9 Results

In this preliminary study, a dataset consisting of 1170 slices containing one pre-contrast and five post-contrast bilateral axial MR mammograms from 39 patients with 76 mass lesions was used. 600 slices of this set containing 21 benign and 25 malignant lesions was used to form the training dataset. The remaining data consisting of 570 slices with 18 benign and 12 malignant lesions was used as the test dataset. The images contained not only breast tissue, but also muscles, heart, lungs and thoracic cavity. To prevent false detections from irrelevant tissues, breast tissue region was first segmented from pre-contrast images using four cascade-connected 2D CNNs. The segmentation algorithm performed well with high average precision, high true positive volume fraction and low false positive volume fraction with an overall performance of 0.93±0.05, 0.96±0.04 and 0.03±0.05, respectively (training: 0.93±0.04, 0.94±0.04 and 0.02±0.03; test: 0.93±0.05, 0.97±0.03 and 0.05±0.06). Suspicious regions were detected from normalized maximum intensity-time ratio (nMITR) maps computed over the pre and post-contrast images of the segmented breast region. A fuzzy 3D CNN with a control template consisting of three layers of 11×11 cells was applied next to discriminate previously marked lesions. To reduce false-positive detections due to artifacts caused by deceptively enhanced blood vessels, nipples and normal parenchyma and artifacts from vascularized tissues in the chest-wall due to over segmentation, a set of decision rules extracted empirically from volume and 3D eccentricity features were used to make final decisions and localize lesions.

Free-response receiver operating characteristic curves that show the performance of lesion detection sensitivity versus false positives per lesion, per slice and per case are given in Figure 5.1. From these curves, it can be observed that the performance of the system is quite satisfactory. For the training dataset, the maximum detection sensitivity is 100% with false-positive detections of 0.28/lesion, 0.09/slice and 0.65/case. However, for the test dataset, the maximum detection sensitivity is 97% with false-positive detections of 0.43/lesion, 0.11/slice and 0.68/case. This is due to a missed 0.16cm^3 small benign lesion that has moderate continuous enhancement. On the average, for a detection sensitivity of 99%, the overall performance of the system is 0.34/lesion, 0.10/slice and 0.67/case.

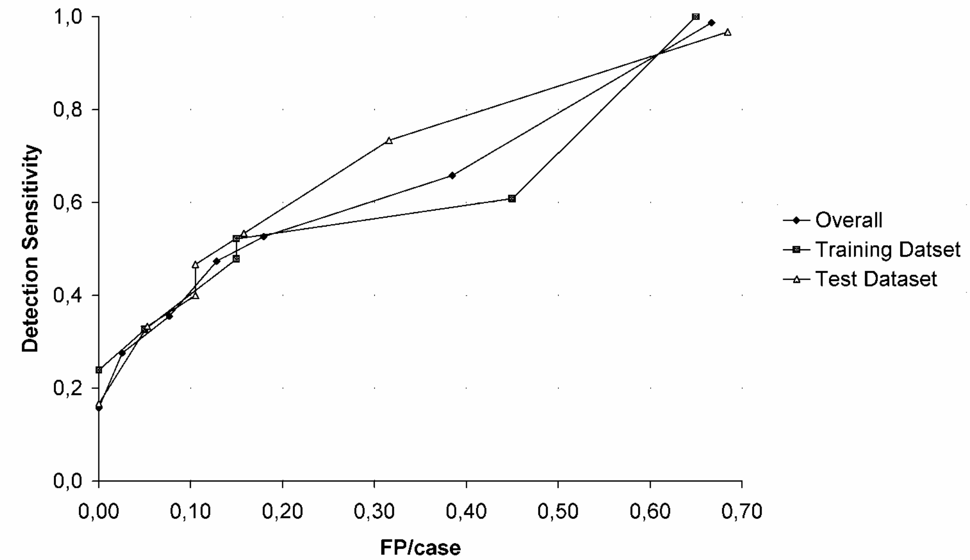

(a)

Figure 5.1 Free-response receiver operating characteristic curves that show the performance of lesion detection sensitivity (a) for false positives per lesion, (b) for false positives per slice and (c) for false positives per case.

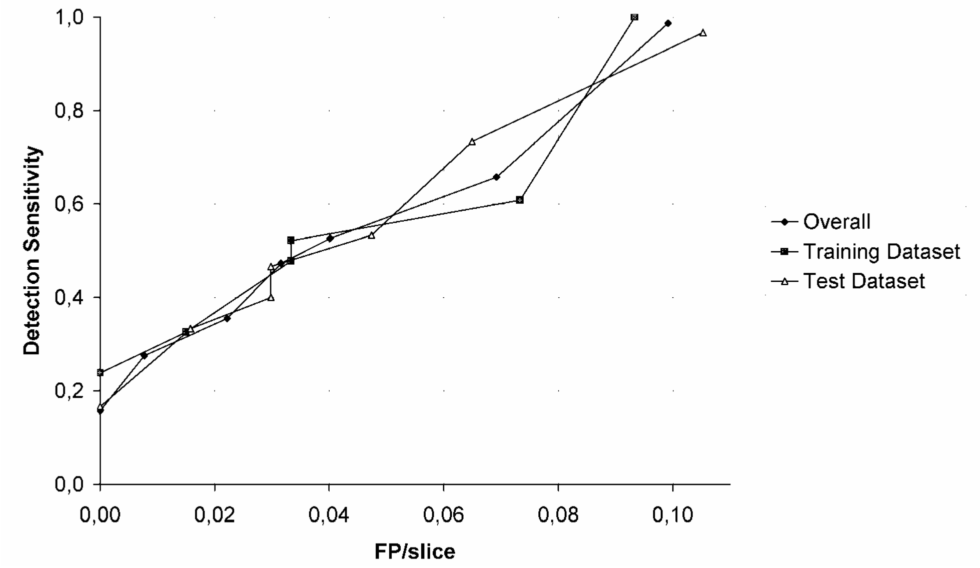

(b)

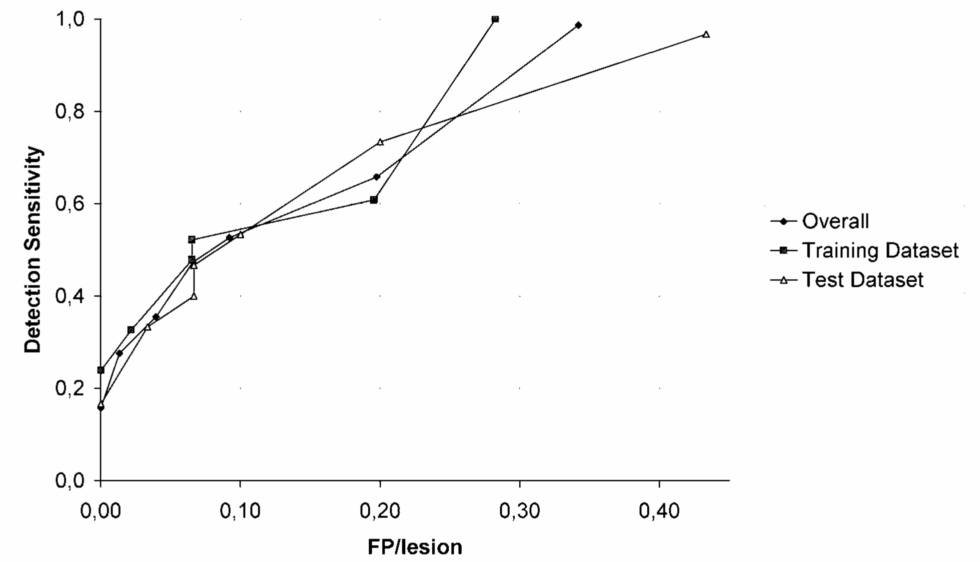

(c)

Figure 5.1 Continued.

For illustrating the technique, a patient with a small benign lesion (49-year-old women with a fibroadenoma finding on right breast near to the chest-wall) is considered. The lesion is present in four slices (begins at slice 14 and ends at slice 17). Figure 5.2 shows the maximum intensity projection (MIP) of the representative slice in which the lesion has the largest diameter (slice 16). The lesion is located near the chest wall and therefore may be missed when the breast is not segmented accurately. However, using the method introduced, the breast is segmented reasonably correctly. Figure 5.3 shows the pre-contrast image and the automatically segmented breast region (as a contour overlay) corresponding to the representative slice. The outputs of CNN_T , CNN_O , CNN_E and CNN_R are given in Figure 5.4.

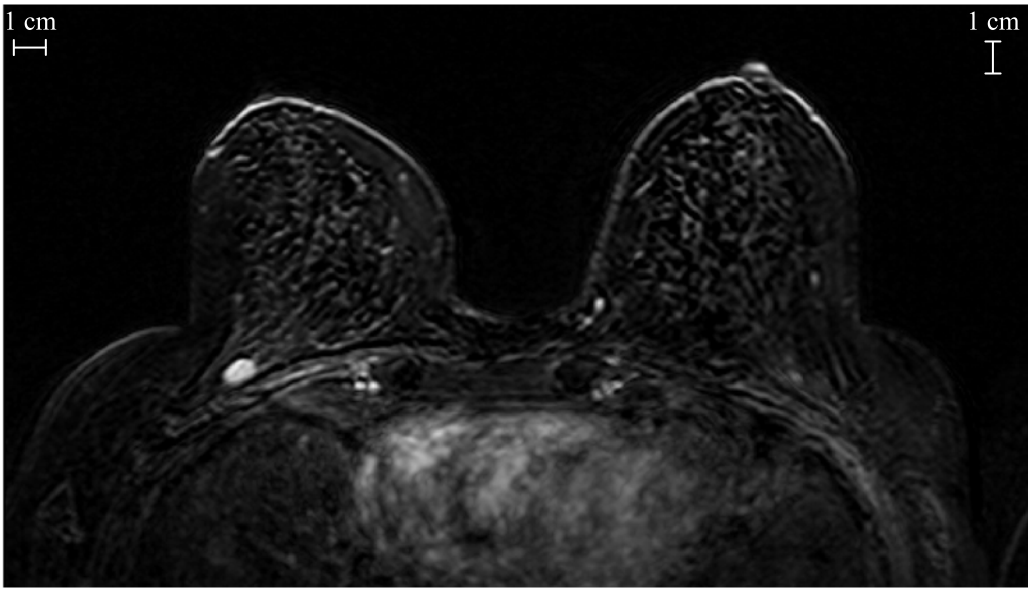

Figure 5.2 The maximum intensity projection of the representative slice (slice 16).

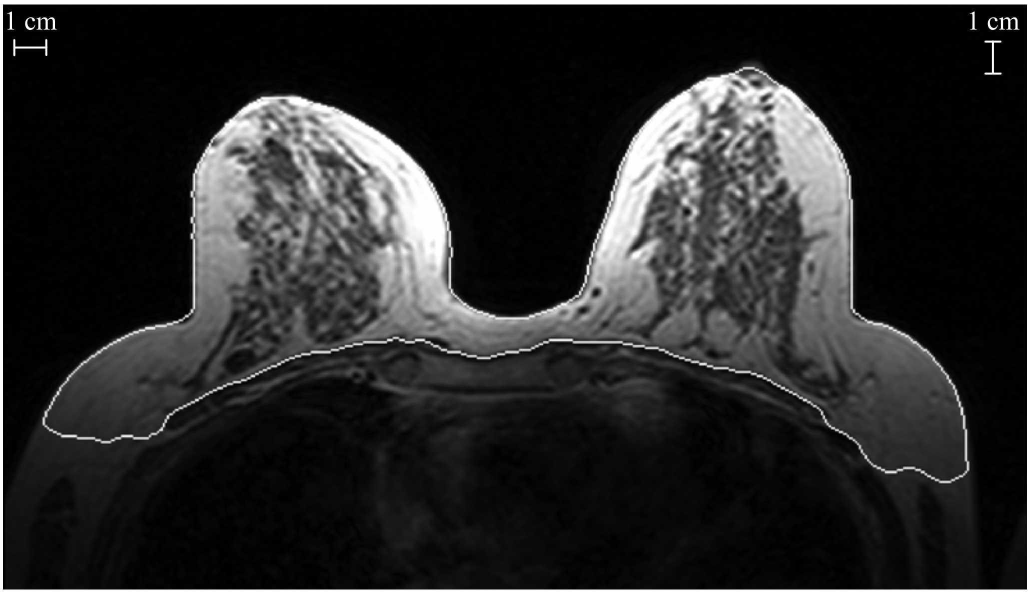

Figure 5.3 Pre-contrast image and the automatically segmented breast region.

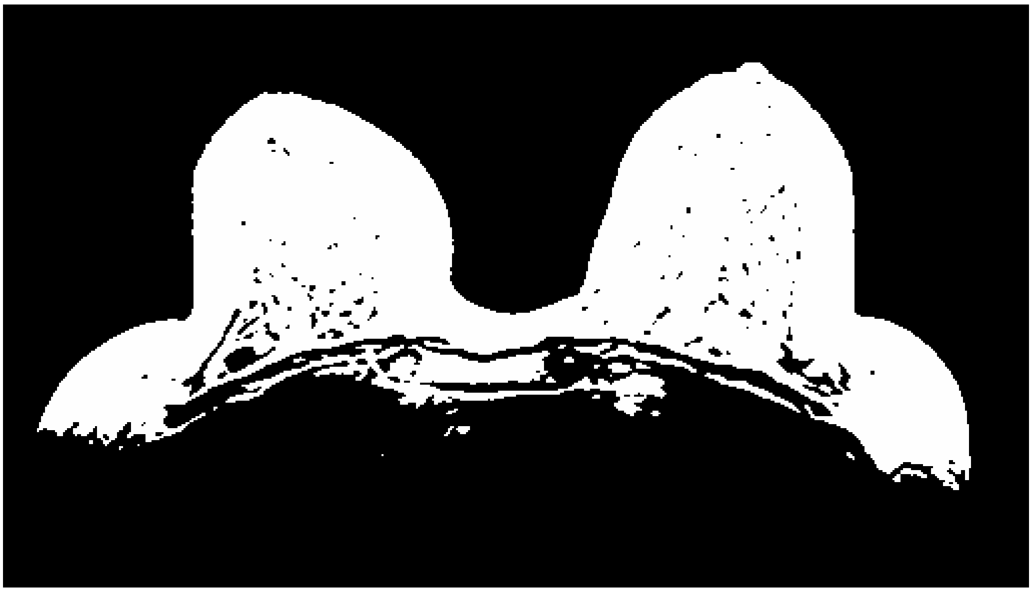

(a)

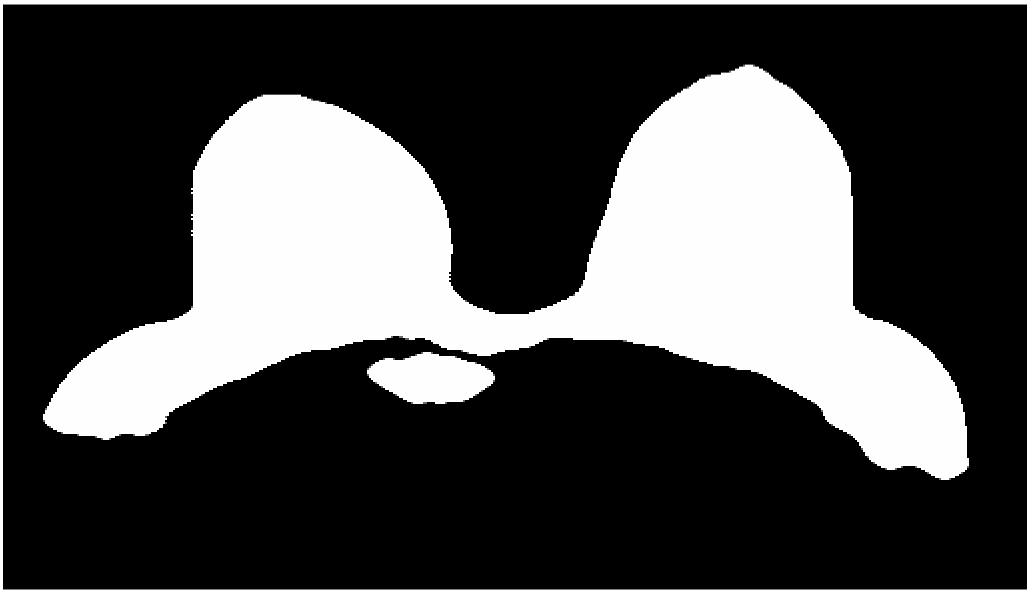

(b)

Figure 5.4 (a-d) Outputs of CNN_T, CNN_O , CNN_E and CNN_R.

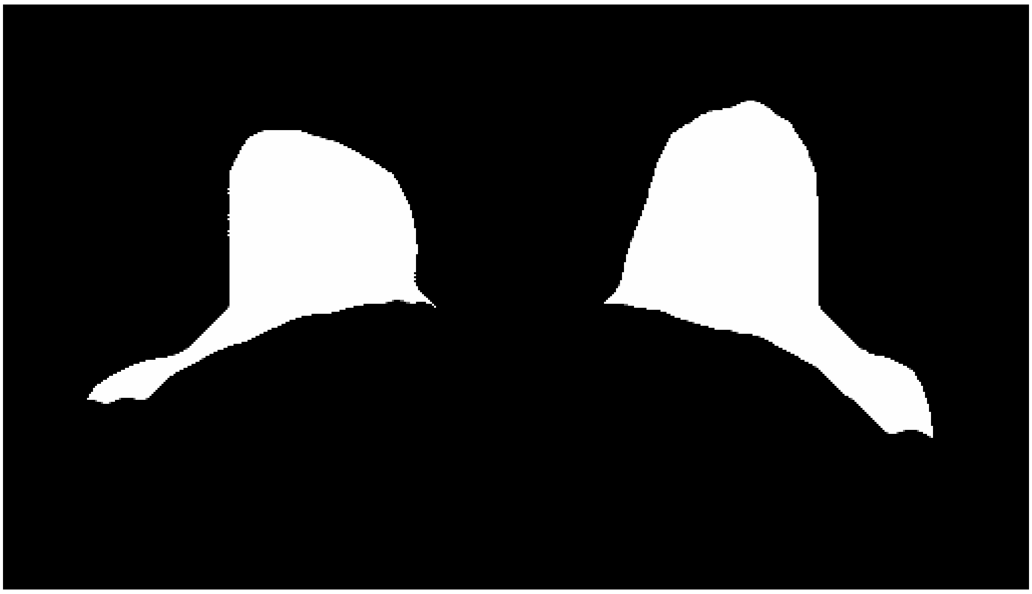

(c)

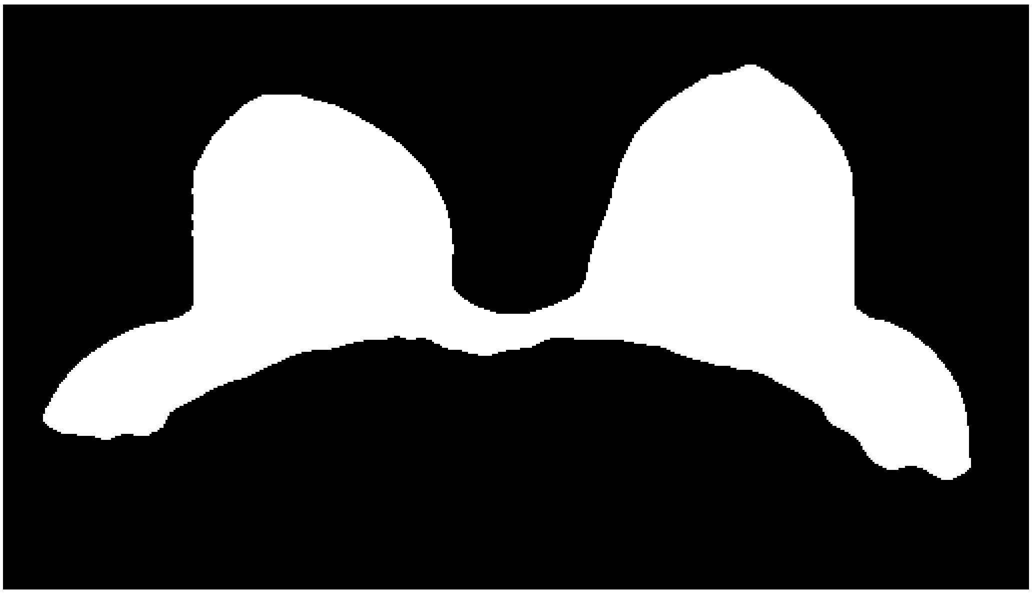

(d)

Figure 5.4 Continued.

The 3D nMITR map of the breast region is generated using a small ROI moved over all the pre and post-contrast images. The nMITR map corresponding to the representative slice is shown in Figure 5.5 (regions having nMITR values greater than 0.33 are shown in white). This 3D map is passed through a threshold and processed with a 3D fuzzy CNN designed to enhance breast lesions. A 2-fuzzy partition having maximum entropy is formed when the membership functions are characterized with the parameters $\hat{a} = -124$ and $\hat{c} = -97$ and $TH_2 = -110.5$, as shown in Figure 5.6.

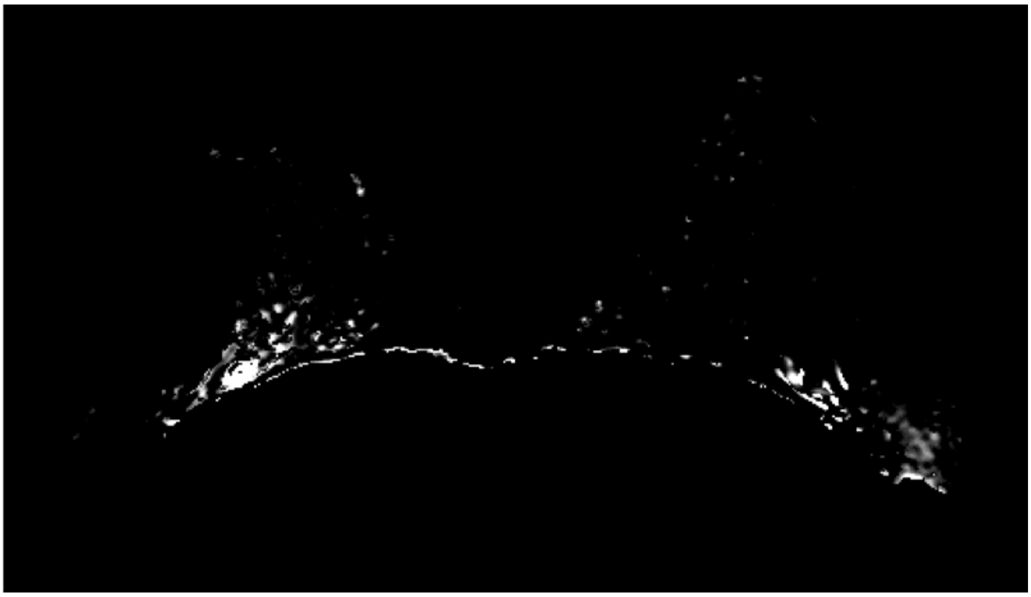

Figure 5.5 nMITR map corresponding to the representative slice (regions having nMITR values greater then 0.33 are shown in white).

After applying volume and 3D eccentricity criteria, the lesion is successfully identified in all the slices without false positives. The breast region manually delineated by the expert (solid black contour), the region segmented automatically (gray colored area) and the lesion localized (black colored area) are presented in Figures 5.7a-d.

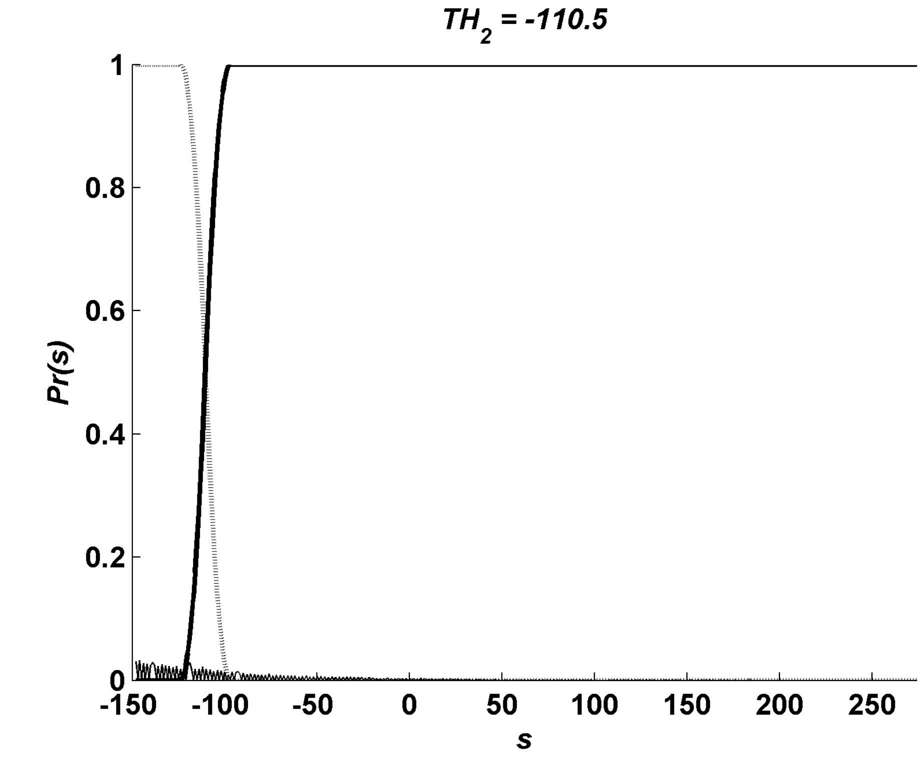

Figure 5.6 Plots of membership functions that form 2-fuzzy partition with maximum entropy.

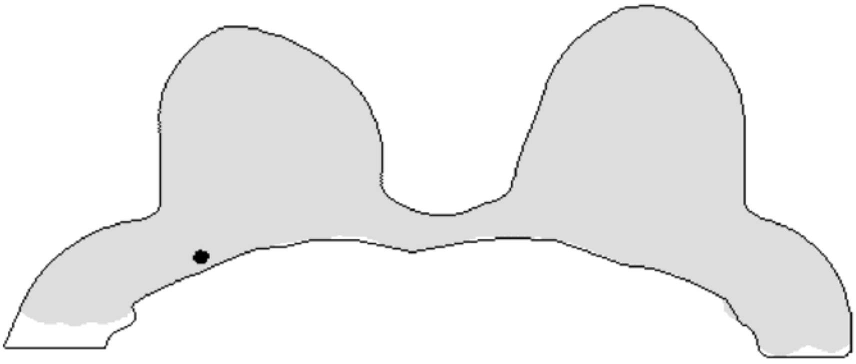

(a)

Figure 5.7 Breast region manually delineated by the expert (solid black contour), the region segmented automatically (gray colored area) and the lesion localized by the system (black colored area). (a) Slice 14, (b) slice 15, (c) slice 16, (d) slice 17.

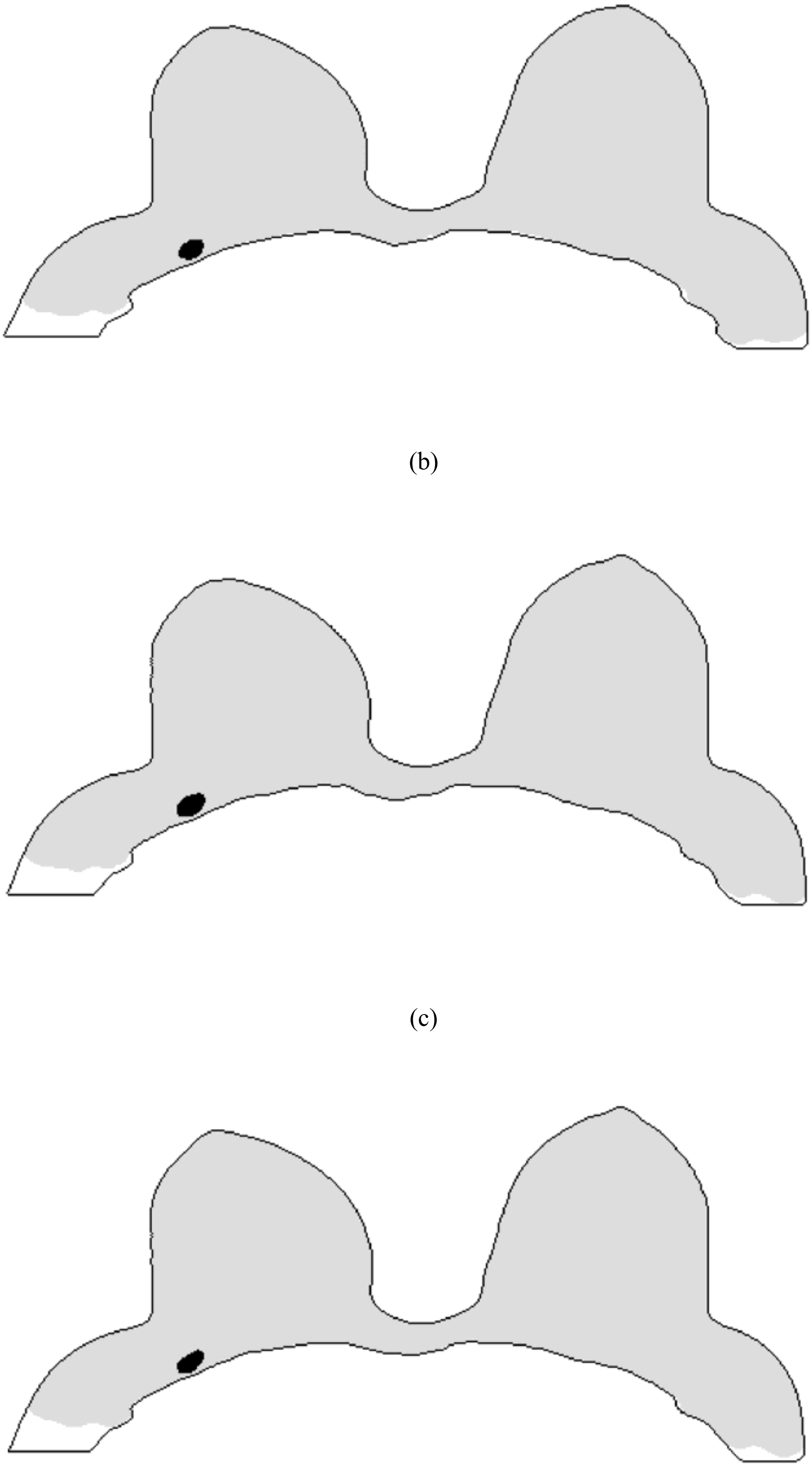

(b)

(c)

(d)

Figure 5.7 Continued.

5.10 Discussion

Qualitative evaluation of CE-MRM is time consuming and requires a great deal of user experience since the number of acquired and constructed images is far too many. Missing of minute details may result in poor specificity and sensitivity in the final diagnosis. Deceptively enhanced regions due to blood vessels and normal parenchyma, especially of premenopausal women, further complicate the evaluations. Although automated methods are being developed to aid radiologists, they still require visually identified and manually marked regions of interests.

In this thesis, a fully automated 3D lesion localization system is introduced that does not require any user guidance. The system makes use of massively parallel cellular structures with learning capabilities called Cellular Neural Networks (CNNs) that offer alternative solutions to complex image processing applications with their extremely high throughputs. Breast region of interest is first segmented from the pre-contrast images using four coupled 2D CNNs connected in cascade. For the segmented tissues, relative enhancements are computed and a 3D normalized maximum intensity-time ratio (nMITR) map is generated. This map is converted into binary form using a threshold so chosen that tissues that have low degrees of enhancements are discarded while the rest are reserved. To boost lesions and to eliminate moderately enhanced normal tissues, the resulting binary image is processed by a 3D CNN with a fuzzy c-partitioning output function. Suspicious regions in the resultant map are pre-localized through volumetric 6-neighborhood connectivity search. A set of decision rules extracted from volume and 3D eccentricity features are used to make final decisions and localize lesions.

The system introduced does not require prior information concerning breast anatomy; it is robust and exceptionally effective for detecting breast lesions. At a detection sensitivity of 99%, false positive rate per lesion is less than 0.34 and false positive rate per case is less than 0.67, overall. In comparison, computer identified regions from the most enhancing membership category, Bian’s method [13] detects only 16 lesions (76% of the studied cases) with a higher false positive rate per case (9.00) (see the footnote on page 149).

We have also analysed the “extended” dataset using the lesion localization method based on 3D template matching, introduced in our previous study. For the training dataset, the maximum detection sensitivity was found to be 91% with false-positive detections of 1.20/lesion, 0.47/slice and 2.75/case. However, for the test dataset, the maximum detection sensitivity was 70% with false-positive detections of 2.00/lesion, 0.73/slice and 3.16/case. The overall performance was as follows: detection sensitivity 83%, false positive rate per lesion 1.52, false positive rate per slice 0.57 and false positive rate per case 2.91.

The use of CNNs, fuzzy c-partitioning, volume and 3D eccentricity criteria reduces false-positive detections due to artifacts caused by deceptively enhanced blood vessels, nipples and normal parenchyma and artifacts from vascularized tissues in the chest-wall due to over segmentation. We hope that this system will facilitate breast MR examinations, improve localization of lesions, provide important information before surgery, help reduce mortality due to undetected cancer re-occurrence as a result of missed multicentricity and decrease the number of unnecessary biopsies and mastectomies.

A software implementation of the proposed method, using a PC equipped with 2.4GHz processor, 3GB RAM, and Matlab 7.0, requires less than 18 minutes to process a single patient data. Although, this time can be reduced to sub-minute levels, using optimizing compilers, a direct hardware implementation will allow almost “real-time” processing speeds and will certainly open up new clinical applications. For example, quasi-automated MR-guided biopsies may be feasible and additional post-contrast lesion images can be acquired to improve morphological characterizations.

The system is currently developed to segment axial breast images and to localize lesions but does not discriminate malignancy. By a simple modification of the CNN_O it can be extended to images acquired in other views and by considering additional dynamic and morphological features such as mean margin sharpness and nMITR entropy of a detected lesion volume it can be equipped with discrimination capabilities [19, 116]. Because these features are quantitative and come from 3D data, this will not only improve standardization and diagnostic accuracy, but will also result in considerable savings in overall evaluation times; these issues are especially important for multi-center facilities.

6. ENHANCEMENT DESCRIPTORS FOR MALIGNANCY DETECTION

6.1 Introduction

Dynamic contrast enhanced magnetic resonance mammography (DCE-MRM) is gaining acceptance in mammographic evaluations. According to Pavic et.al., only DCE-MRM “has the potential for detection of lesions not seen by (X-Ray) mammography and ultrasound, and for non-invasive characterization of breast lesions” [106]. Although the resolution of DCE-MRM is lower than X-ray mammography, its 3D properties are invaluable in exact localization, visualization, and the assessments of the aggressiveness and the multifocality of the lesions. An important advantage in favor of DCE-MRM, beside absence of ionizing radiation is that lesion-obscuring overlapping structures and summation shadows are much less pronounced in comparison with X-ray mammography since in case of MRM there is no need for excessive breast compression during imaging.

In DCE-MRM, a contrast agent is injected and several pre-contrast and sequential post-contrast MR images are acquired. The concentration of the contrast agent at malignant lesions will be higher than those of the surrounding regions due to increased vascularity in these regions. Image subtraction and/or maximum intensity projection (MIP) are used to augment and detect enhancing regions. Once identified, a lesion is evaluated using various qualitative and quantitative techniques based on its morphological and/or the enhancement properties.

Qualitative methods are in general, based on a visual analysis of the morphology and shape of the contrast enhancement curve obtained for a manually positioned 2D region of interest (ROI) [15, 22, 23, 24]. Proper selection of the size and the position of an ROI is an important issue that depends highly on experience. In general, it is advantageous to place a region of interest (ROI) over the early enhancing component of a lesion. If a larger ROI is used, necrotic components of the lesion may undesirably affect the evaluations; in case enhancement curves and morphologies of benign and malignant lesions are visually similar, the performance of methods that use qualitative techniques will be poor. *Quantitative* methods make use of a number of protocols and quantitative interpretation criteria such as maximum signal enhancement rates at specific times, time to maximum enhancement and wash-out ratio, etc. to standardize MR mammography and improve diagnosis [25, 26, 27, 28, 29, 30]; the ROI is manually or semi-automatically positioned. Recently, the maximum intensity time ratio (MITR) and its normalized form have been shown to be an important criterion for lesion detection. A summary of these studies and the key characteristics are presented in Table 6.1.

Flickenger et al [31] claimed that the MITR is "the most accurate numerical descriptor of the enhancement pattern for separating benign breast lesions from malignant lesions". They analyzed enhancement characteristics of palpable breast masses in 23 patients (10 malign and 13 benign lesions) using large ROIs. Three of the eight fibroadenomas exhibited enhancement patterns indistinguishable from cancer; this might be due to intensity inhomogeneities. Had they used normalization, they would likely have had even better results.

Liney et al [32] examined 117 breast MR lesions and evaluated the maximum enhancement rates and normalized MITR (nMITR) measurements over user-defined and semi-automated ROIs. In each case, a slice was selected that contained the largest cross section of the suspicious lesion. Three types of measurements were performed: whole lesion ROI, the most enhancing 9 pixel ROI and 10% threshold ROI. The results demonstrated the significance of nMITR values for benign and malignant tumors ($P=$ 0.096, 0.023 and 0.001 for each type of measurement, respectively). Although high significance can be achieved when the nMITR parameter was computed using a small semi-automated ROI, it was concluded that these approaches were highly dependent on the radiologists' experience.

Gibbs et al [33] developed and compared four breast cancer classification schemes that utilize enhancement and textural features of the lesions. Their data set included 45 malignant and 34 benign lesions from 79 women (acquired with a 3D MR imaging

Table 6.1
Quantitative measurement of nMITR from manually drawn ROIs.

Reference	Imaging Resolution	Number of Cases	Measurement Strategy	Parameter used to discriminate malignant and benign lesions	*P*-value	Diagnostic Accuracy
[31]	NA	23 (13 B, 10 M)	Whole lesion ROI	MITR	NA	Three of eight fibroadenomas indistinguishable from cancer.
[32]	NA	117 (36 B, 81 M)	Whole lesion ROI	nMITR	0.096	NA
			9 pixel ROI	nMITR	0.023	NA
			10% threshold ROI	nMITR	0.001	NA
[33]	256×128	79 (34 B, 45 M)	Whole lesion ROI	nMITR	0.130	0.620
			Whole lesion ROI	Patient age, lesion size, time to max. enhancement and two textural parameters	NA	0.920
[16]	112×256	115 (35 B, 70 M)	Whole lesion ROI	The curve type, relative signal intensity decrease from the peak to the 7th and 5th postcontrast images, , relative signal intensity decrease from the first to the 7th postcontrast image, nMITR and time-to-peak features	NA	0.942 * 0.737 **
			Whole lesion ROI	All the kinetic and the morphologic features (totally 14 features)	NA	0.981 * 0.786 **
[34]	256×128	49 (17 B, 32 M)	Whole lesion ROI	nMITR	0.060	0.640
			9 pixel ROI	nMITR	0.023	0.650
[35]	256×192	88 (68 B, 20 M)	Whole lesion ROI	nMITR	0.008	0.852
			9 pixel ROI	nMITR	0.019	0.795

* using the training set, ** using verification set, M: Malignant, B: Benign, NA: not available

sequence and a matrix size of 256×128). An experienced radiologist examined and drew ROIs on the images to cover whole lesions as closely as possible while excluding speculations and surrounding fatty tissues. Relative enhancement at 1 minute and 2 minutes, maximum relative enhancement, time to maximum enhancement and nMITR were computed. nMITR had a *P*-value of 0.130 and a diagnostic accuracy of 0.620. Time to maximum enhancement was found to be the most significant enhancement parameter (*P*= 0.0002 and accuracy= 0.740) and therefore was used in all the schemes. The most diagnostically accurate scheme (accuracy= 0.920) was based on the patient age, lesion size, time to maximum enhancement and two textural parameters. It was also concluded that the lack of discrimination power evident in nMITR was probably due to the large number of fibroadenomas (31 of 34) in the data set.

Szabo et al [16] assessed the discriminative ability of morphologic and kinetic features of breast lesions and their relative relevance using artificial neural networks (ANNs). 105 breast lesions, 75 malignant and 30 benign, were considered. Dynamic MR imaging was performed using a 3D sequence and a 112×256 matrix. Manually drawn ROIs were positioned over a tumor area that showed high enhancement at early postcontrast images; the earliest and the strongest enhancements were chosen for each lesion. Morphologic parameters were margins, homogeneity, rim enhancement and septations. Kinetic features were signal intensities, percentage enhancement, curve type, relative signal intensity decrease, nMITR (they called as slope) and time to peak enhancement. They used an ANN, based on the curve type, relative signal intensity decrease from the peak to the 7th postcontrast image, relative signal intensity decrease from the peak to the 5th postcontrast image, relative signal intensity decrease from the first to the 7th postcontrast image, nMITR and time-to-peak features. It showed a diagnostic accuracy of 0.942 on the training set and 0.737 on the verification set. If all the kinetic and the morphologic features (totally 14 features) were utilized, the accuracy was maximized (accuracy of 0.981 on the training set and 0.786 on the verification set).

Gibbs et al [34] studied differential diagnosis of sub-1 cm breast lesions (32 malignant and 17 benign) detected on contrast enhanced MR images from 43 women using a 3D sequence and a 256×128 matrix. ROIs, encompassing the whole lesion as closely as possible, were drawn by an expert radiologist. 9-pixel square ROIs were semi-automatically positioned on the most enhancing area. Relative enhancement at 1 minute and 2 minutes, maximum relative enhancement, time to maximum enhancement, MITR and nMITR were computed for each type of ROIs. Statistical analysis results demonstrated that nMITR gave higher performance than the MITR. For a whole lesion, nMITR gave the best performance (P= 0.060 and accuracy= 0.640±0.080) while good performance was achieved for 9-pixel square (P= 0.023 and accuracy= 0.650±0.080). The contrast enhancement rates were also fitted to a two-compartment pharmacokinetic model and amplitude, exchange rate constant and the washout rate constant were computed. The best individual parameter calculated from the dynamic images was found to be the exchange rate constant (with an accuracy of 0.740±0.080). A diagnostic accuracy of 0.920±0.030 was achieved for a logistic regression model that combines exchange rate and qualitatively determined tumor morphology.

Kneewshaw et al [35] analyzed breast MR images of 88 patients with mammographically detected micro calcifications (20 malignant and 68 benign). 3D images were acquired with a 256×192 matrix. Relative enhancement at 1 minute and nMITR were computed using whole lesion ROI and a 9-pixel box ROI (as used by Gibbs et al). For both methods, the most significant parameter to differentiate benign from malignant lesions was found to be the enhancement at 1 minute. However nMITR of whole ROI and 9-pixel square ROI were found to have greater diagnostic accuracies, 0.852 (P= 0.080) and 0.795 (P= 0.109), respectively.

Recently, there are some efforts to make use of computerized analysis of DCE-MRM. MRIW is a software developed by Leach's group is a frontier research to quantify contrast agent in dynamic contrast enhanced MR images [6]. Five parameters (onset time – time taken to reach 10% enhancement-, initial gradient –rate of increase in signal intensity at the 10% point-, mean gradient –mean rate of signal intensity increase between the 10% point and the 90% point-, maximum enhancement and washout rate are calculated pixel-by-pixel to generate color maps visualizing highly enhancing breast tissues with manual thresholding. These maps provide valuable information during the subjective placement of ROIs.

MTDYNA (Mevis Inc, Germany) is another software tool that generates color parametric maps of relative changes in each pixel's signal intensity over time. Three time points are used to determine the color coding: the precontrast, first postcontrast and final time point. Enhancement of initial postcontrast time point relative to the baseline precontrast time point determines an initial color category. The final displayed colors for each pixel are determined by the rate of enhancement change between the initial postcontrast and last post contrast points. The software has a commercialized version called as DynaCAD (Invivo Inc., USA). It has improved capabilities in functional parametric analysis. Eleven parameters calculated pixel-by-pixel are maximum enhancement, enhancement at a time point, value at time point, two phase –the method of MTDYNA-, time to peak, MITR, maximum descent, maximum slope, mean transit time and integral –are under the curve. For better evaluation of suspicious enhancements, manually selected thresholded value is needed to be applied. However Wiener et al reported that the use of the software decreases the interpretation time for a case to approximately 5 min, while detecting malignant lesions easily. Achieved diagnostic accuracy was 0.898 [7].

fTP (CAD Sciences Inc, USA) is a software that utilizes a parametric mapping method based on pharmacokinetic analysis. To do this, vessel permeability (K) and extra-cellular volume (EVF) are calculated pixel-by-pixel by fitting a curve over all available time points. Tissue physiology histogram and fTP colorized images are the visual outputs. The software provides direct link between histogram plot and pixel location in the colorized image. In a clinical study, the mapping method is demonstrated to show 96% sensitivity and 82% specificity in solid lesions detection [4].

CADstream (Confirma Inc, USA) produces colored images to identify areas of significant enhancement after pixel-by-pixel analysis. In addition, it provides details about regions that show significant enhancement. To do this, the radiologist selects a specific area of significant enhancement and the program will automatically generate a synopsis of the full volume of that lesion, including the percentage of the lesions that shows washout, plateau and persistent enhancement. Lehman et al studied the benefits of these percentages in discrimination of breast cancer. They used threshold values of 25%, 50% and 100% enhancement. All malignant lesions showed significant enhancement at all thresholds. The computer-assisted analysis yielded false positive rates that were reduced by 25%, 33% and 50% for each threshold, respectively. There were no significant differences found between enhancement profiles of benign and malignant lesions. All lesions showed a wide range of washout, plateau and persistent patterns of enhancement [5].

All these computerized methods try to overcome difficulties associated with subjective ROI analysis using several enhancement parameters. However, a manually selected threshold value that significantly affects the performance of lesion characterization is still a requirement. MRIW and CADstream differ from the other algorithms since they also provide lesion identification and enhancement distributions. To do this, an expert radiologist must first draw an ROI encompassing the whole lesion appropriately or must mark the lesion. The radiologist must be familiar to the distribution data of malignant and benign lesions to make correct decisions.

In the present study we introduce a novel automated 3D lesion detection technique. It is based on the use of a moving 3×3 voxel mask placed within a rectangular prism volume of interest (VOI), manually marked by an expert radiologist that roughly includes suspicious legions on the computed subtraction images and/or MIPs. Relative contrast enhancement rates and nMITR values corresponding to the center voxels of the moving mask are computed to generate nMITR projection data. This data is used to discriminate fatty tissue and vascular enhancements and to identify lesions within the VOI. A simplified flowchart of the technique is given in Figure 6.1. The details are described in the following section.

6.2 Imaging Protocol

Magnetic resonance imaging was conducted on a 1.5 Tesla MR imager (Magnetom Symphony, Siemens Medical Systems, Erlangen, Germany) equipped with a gradient system having a maximum amplitude of 30 mT/m. A dedicated four-element phased-array receiver breast coil was used. Patients were placed in a prone position during the scan to minimize motion artifacts. The imaging sequence was a variant of spoiled gradient echo imaging, T_1-weighted 3D fast low angle shot (FLASH, TR/TE 9.80/4.76 msec, flip angle 25^{o}, slice thickness 2.5 mm with no gap, 512×512 matrix and $0.625\text{mm}\times0.625\ \text{mm}^2$ resolution in the x and y directions). During and immediately after bolus injection of the

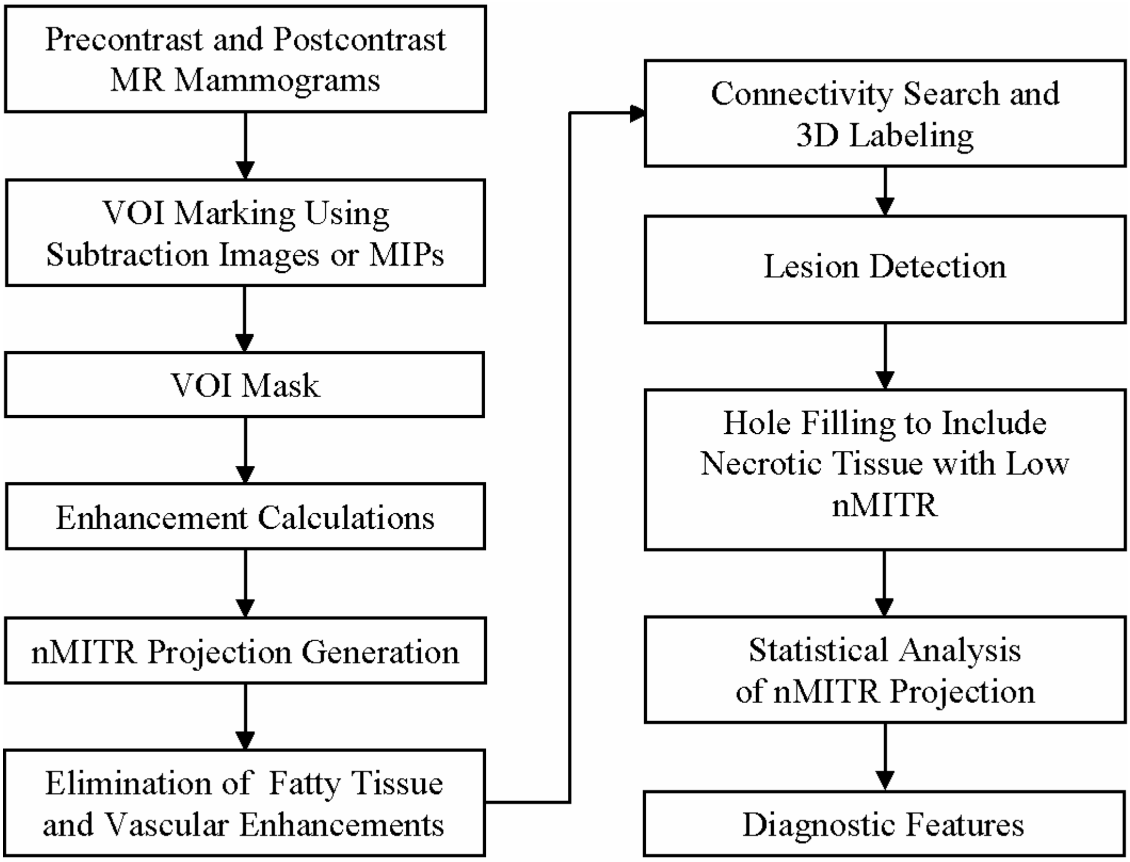

Figure 6.1 Simplified flowchart of the lesion detection scheme.

contrast agent, (Gd-DTPA, 0.1 mmol/kg body weight) one precontrast and five postcontrast axial images were acquired per slice with a temporal resolution of approximately 88 seconds.

6.3 Lesion Dataset

52 lesions, 23 benign and 29 malignant, from 46 women aged between 32 and 83 years (mean 46 years) were retrospectively entered in this study[2]. Written informed consent was obtained from each patient. The lesion volumes ranged from 0.07 cm^3 to 17.20 cm^3 (mean 2.58 cm^3). All cases were proved either by histopathological examination or by clinical follow-up and labeled as benign or malign. Dynamic 12-bit grayscale image sets

---

[2] As part of our program, we prospectively perform MR mammography for preoperative staging of patients with known malignancies and for characterization of lesions for patients diagnosed to have solid lesions detected by mammographical or ultrasound examinations.

that showed sufficient anatomical alignment were transferred from the MR scanner to a personnel computer in DICOM format for further analysis using Matlab 7.0 (The Mathworks, Inc., USA).

6.4 Volume of Interest Selection

As the initial step, an expert radiologist should first manually mark a rectangular prism volume of interest (VOI) that roughly includes suspicious regions on the computed subtraction images and/or MIPs. This VOI should include the first and the last slices of the region.

6.5 nMITR Projection Generation

Enhancement computations are performed using a 3×3 voxel mask $\Re$, placed at some reference voxel within the VOI. The relative contrast enhancement rate corresponding to the voxel at the center of the mask is computed using [54]:

$$E_{\Re}(i) = \frac{I_{\Re}(i) - I_{\Re}(0)}{I_{\Re}(0)} \times 100 \tag{6.1}$$

where $i = 1, 2, ...5$ is a time index and represents the times at which postcontrast images are taken. $I_{\Re}(0)$ is the average intensity of the precontrast image (at the reference time 0) within $\Re$, $I_{\Re}(i)$ is the average intensity of the post-contrast image at time $t = 88 \times i$ seconds within $\Re$. $E_{\Re}(i)$ represents the enhancement value of $\Re$ at time $t = 88 \times i$. The nMITR values are computed using

$$nMITR_{\Re} = \frac{\max\left\{E_{\Re}\right\}}{T_{\max}} \tag{6.2}$$

In Eq. 6.2, $T_{\max}$ denotes the time, in seconds, when the enhancement $E_{\Re}$ reaches to its maximum. The above computations are repeated after moving $\Re$ to another voxel position within the VOI. When every voxel within the VOI is covered, a 3D nMITR projection data set is generated. This data set is basically used for the subsequent analyses, evaluations and visualizations.

6.6 3D Lesion Segmentation

Volumetric lesion segmentation is performed using a semi-automated method. To reduce diffuse background enhancements due to fatty and vascular tissues surrounding the lesion as much as possible, the nMITR projection data is passed through an empirically determined threshold (0.277 sec^{-1}). A lesion identification procedure is carried out to discriminate highly enhancing vessels within the VOI as follows: An 18-neighbourhood connectivity search and labeling operation is performed first to identify enhancing objects (regions) in 3D. The object that has the biggest volume is identified as the lesion. Morphological hole filling is applied next to include necrotic tissues inside the lesion that show low nMITR.

6.7 Feature Extraction

The nMITR values within projection data of the identified lesion are first reformatted so that they have 0.1% precision. This data is then explored statistically to extract the following six potentially diagnostic features: The maximum value, the mean value, the standard deviation, the kurtosis, the skewness and the nMITR-entropy using the following equations:

$$\mu = \sum_{j=1}^{N} p(j) \times nMITR(j) \tag{6.3}$$

$$\sigma = \sum_{j=1}^{N} p(j) \times \left(nMITR(j) - \mu\right)^2 \tag{6.4}$$

$$k = \frac{\sum_{j=1}^{N} p(j) \times \left(nMITR(j) - \mu\right)^4}{\sigma^2} - 3 \tag{6.5}$$

$$s = \frac{\sum_{j=1}^{N} p(j) \times \left(nMITR(j) - \mu\right)^3}{\sigma^3} \tag{6.6}$$

$$e = -\sum_{j=1}^{N} p(j) \times \log(p(j)) \tag{6.7}$$

In the above equations, μ is the average nMITR value and $p(j)$ is the probability of the j-th nMITR. N represents the number of distinct nMITR values (within the 0.1% precision).

6.8 Statistics

The significance and the diagnostic accuracy of each feature in discriminating malignant and benign lesions are evaluated using SPSS 14 (SPSS Inc., USA). The independent samples t-test with either a pooled or separate variance as determined by the Levene's test for equality of variances is performed. A P-value of <0.05 is considered statistically significant. Receiver operating characteristic (ROC) analysis is carried out to determine the diagnostic accuracies of the features [117].

6.9 Results

Fifty-two breast lesions identified from high-resolution MR images of 46 patients are studied. A semi-automated method is used to identify the lesion inside a rectangular prism VOI roughly marked by an expert. Relative contrast enhancements are calculated using a voxel sampling method based on a moving 3×3 mask and a 3D nMITR projection is generated for the VOI. The projection is passed through a threshold to differentiate the suspicious lesion appropriately while eliminating false enhancements of fatty tissues and small blood vessels. A search procedure is performed on the binarized projection to identify suspicious lesions and other highly enhanced vascular regions. Using the nMITR projection data of the identified lesion generated, the following statistical features are computed: The maximum value, the mean value, the standard deviation, the skewness, the kurtosis and the entropy of the nMITR. These values reflect enhancement measurements from a total of 151964 voxels on which the moving 3×3 voxel mask is automatically positioned inside the (estimated) lesions by the system. Examples of the breast lesions estimated by the system are presented in Figures 6.2 and 6.3 as 2D slices. Plots of distinct nMITR values and their probabilities for each lesion are shown in Figure 6.4.

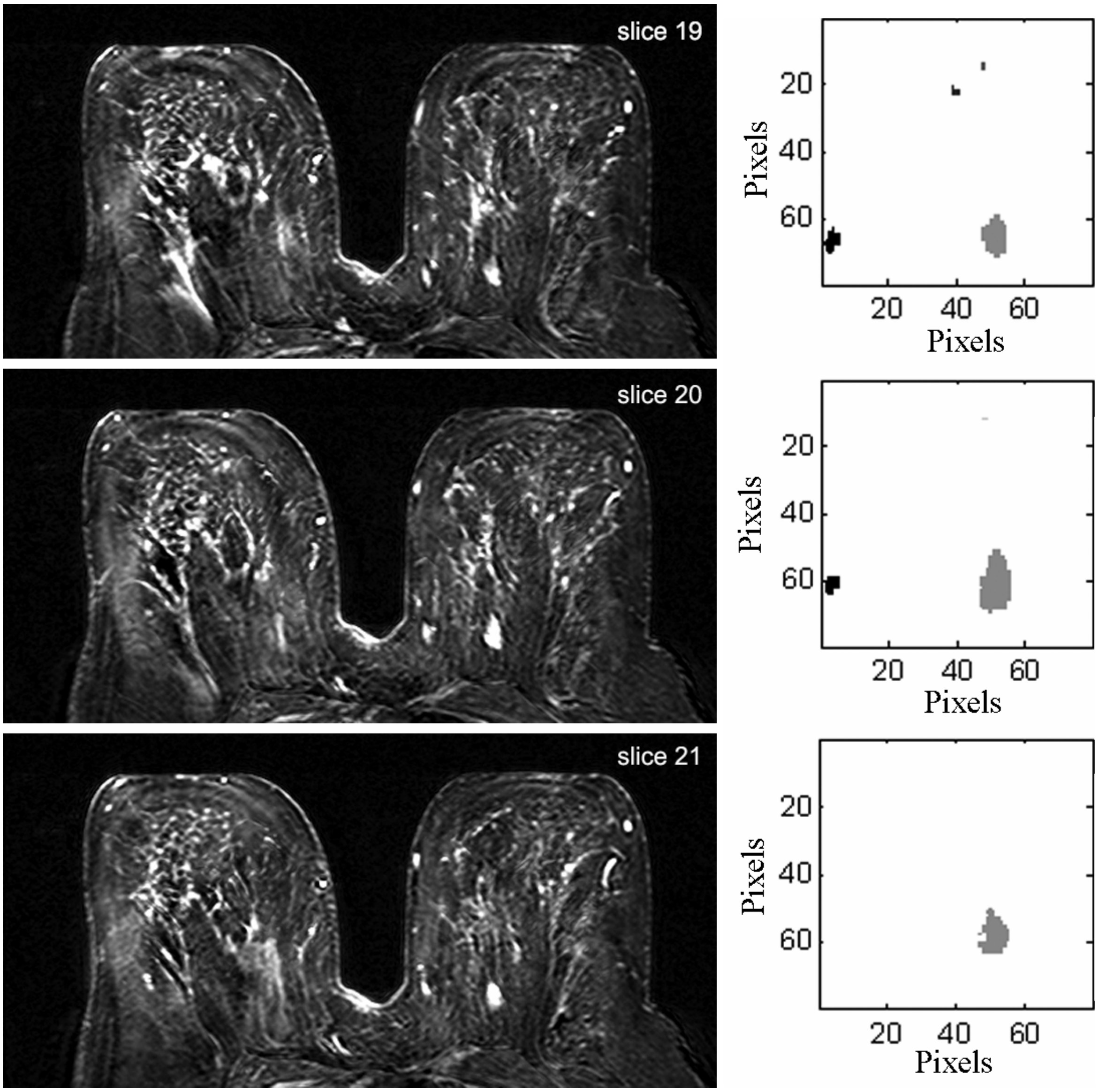

(a) (b)

Figure 6.2 Example of a benign lesion. (a) MIPs, (b) VOI, (c) volumes of the detected objects, (d) identified 3D lesion.

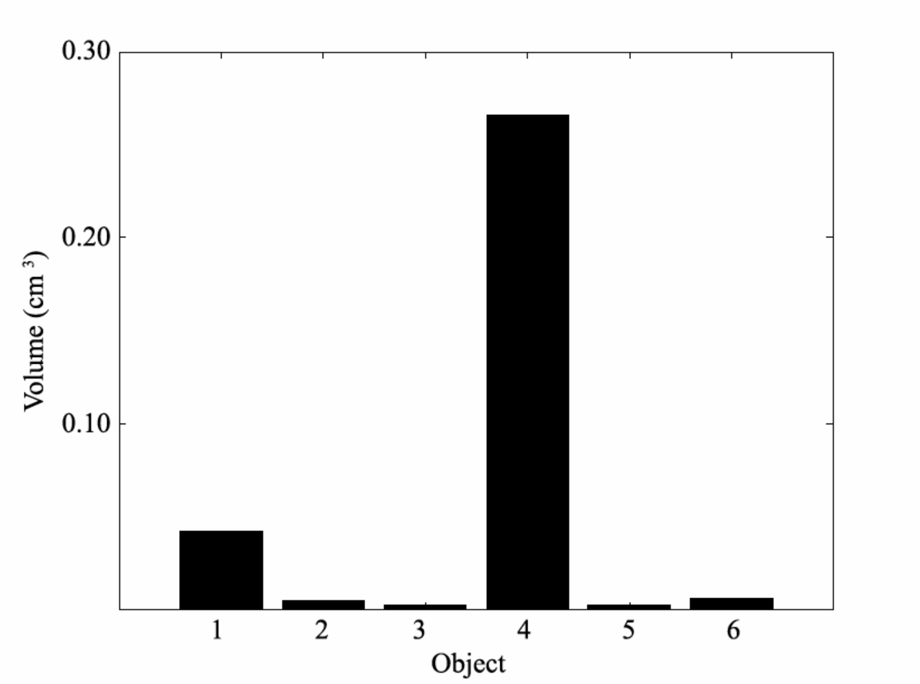

(c)

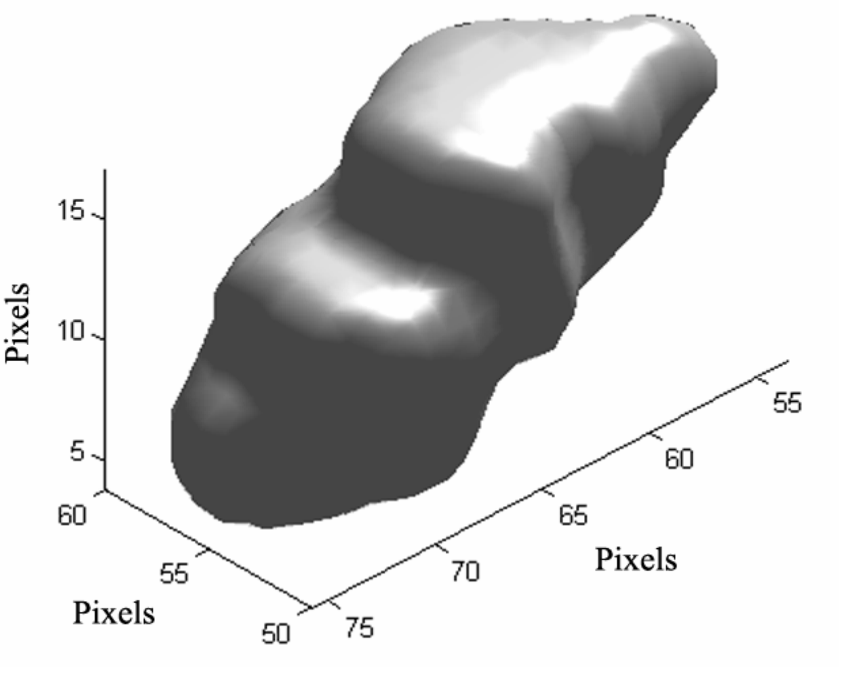

(d)

Figure 6.2 Continued.

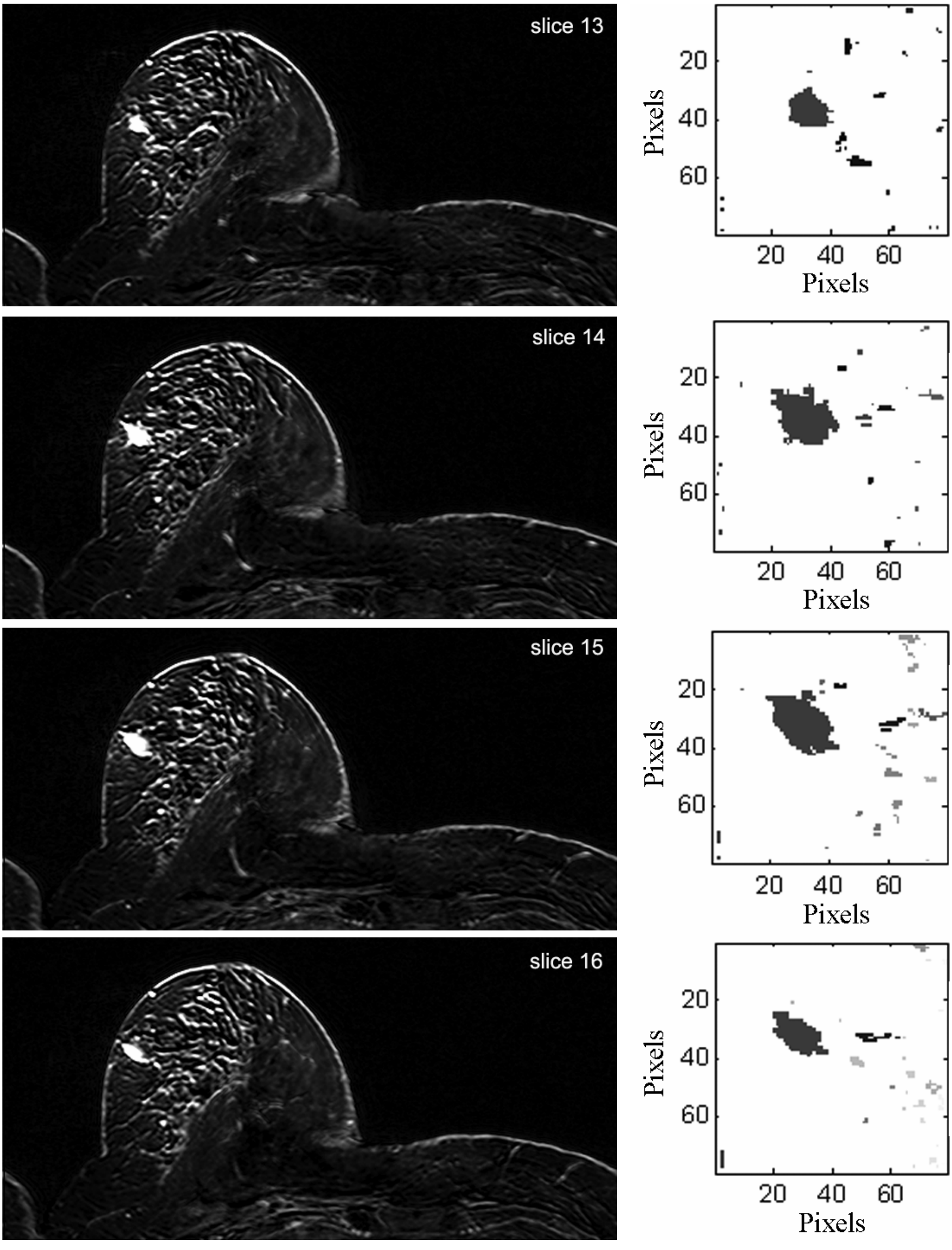

(a) (b)

Figure 6.3 Example of a malignant lesion. (a) MIPs, (b) VOI, (c) volumes of the detected objects, (d) identified 3D lesion.

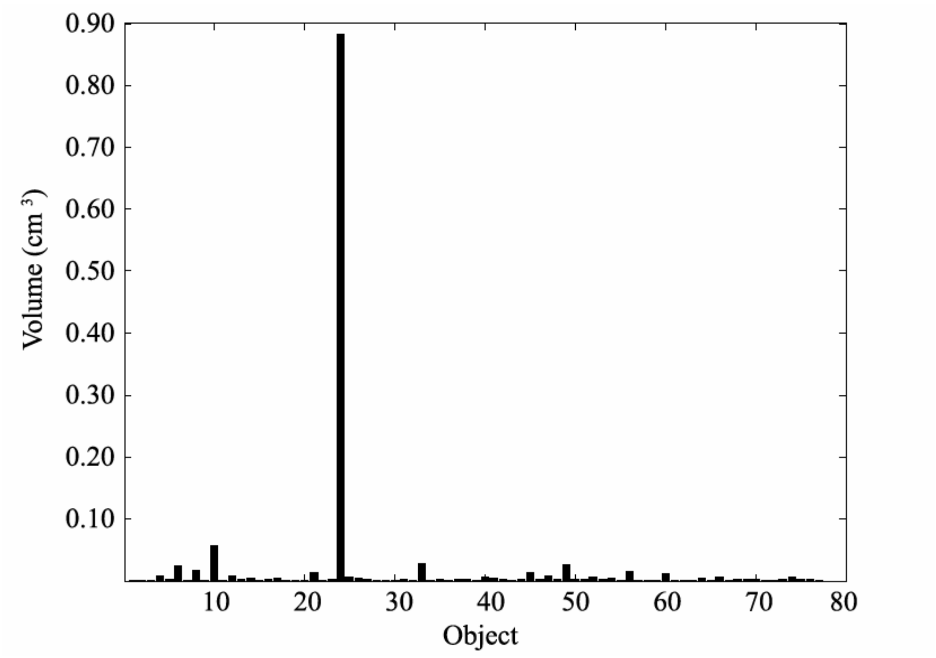

(c)

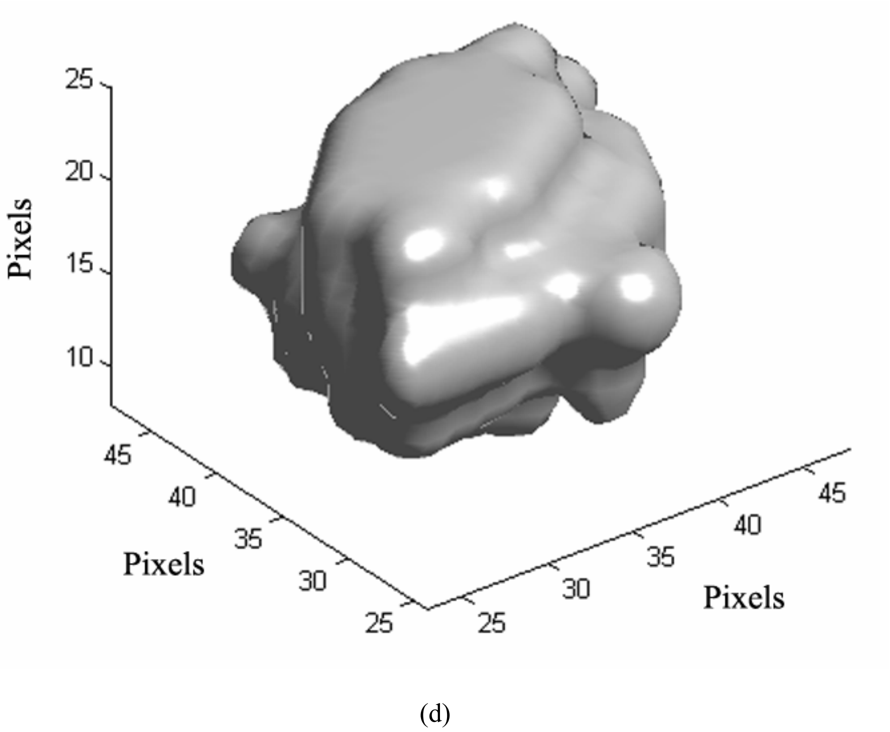

(d)

Figure 6.3 Continued.

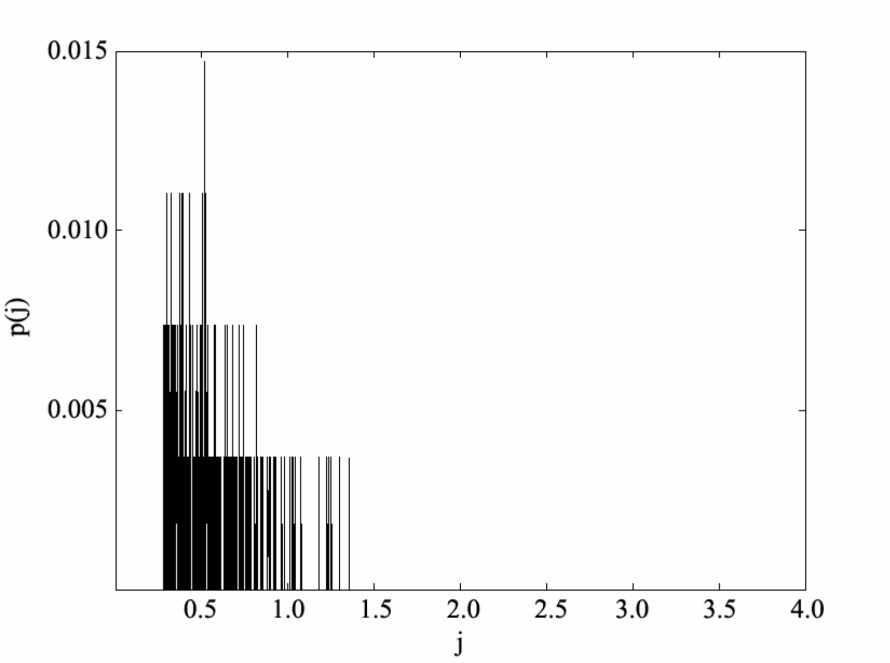

(a)

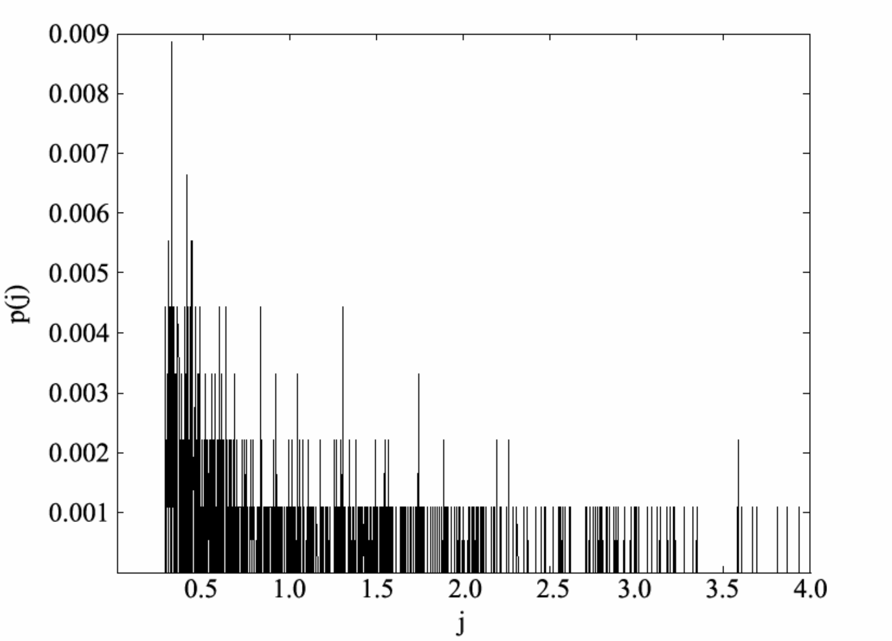

(b)

Figure 6.4 Distinct nMITR values and their probabilities. (a) Benign lesion, (b) malignant lesion

Extracted features are statistically analyzed to determine their significances and accuracies on breast cancer diagnosis. Student t-test results are given in Table 6.2. Area under the ROC curve (AUC) computed for each feature is listed in Table 6.3. The nMITR-entropy shows the highest significance (P=1.59×10^{-12}) and diagnostic accuracy (AUC= 0.97±0.03) while the standard deviation, the maximum and the mean parameters are also found to be significant (P= 3.80×10^{-8}, 3.90×10^{-9} and 1.39×10^{-6}, respectively). The standard deviation of the nMITR is also found to be a significant feature as much as the maximum nMITR and the diagnostic accuracies of both features are found to be similar (AUC= 0.90±0.04 and 0.92±0.04, respectively). The diagnostic accuracy of the mean nMITR is found as 0.86±0.05. Plots of the ROC curves of the significant parameters are shown in Figure 6.5.

Insignificant features are skewness and kurtosis (P= 0.63 and 0.84, respectively). Skewness reflects the asymmetry of the nMITR data around the mean and kurtosis indicates how outlier-prone the distribution of nMITR is. Independent of the lesion type (malignant or benign), nMITR values commonly spread out more to the right of the mean than to the left and nMITR distribution is more outlier-prone than the normal distribution.

Table 6.2
Significance of nMITR based features.

Feature	Benign Mean ± Std.Dev.	Malignant Mean ± Std.Dev.	*t* value	*P*-value
$nMITR_{\max}$	1.56 ± 1.02	4.11 ± 1.54	-7.160	3.90×10^{-9}
μ	0.56 ± 0.23	1.05 ± 0.40	-5.546	1.39×10^{-6}
σ	0.24 ± 0.16	0.69 ± 0.32	-6.678	3.80×10^{-8}
s	1.20 ± 0.72	1.29 ± 0.57	-0.438	6.31×10^{-1}
k	2.07 ± 4.03	1.88 ± 2.62	0.198	8.44×10^{-1}
e	5.40 ± 0.58	6.77 ± 0.48	-9.327	1.59×10^{-12}

Table 6.3
Diagnostic accuracy of nMITR based features.

Feature	AUC	Std. Error	%95 CI of AUC	
			Lower Bound	Upper Bound
$nMITR_{\max}$	0.92	0.04	0.85	0.99
μ	0.86	0.05	0.76	0.96
σ	0.90	0.04	0.82	0.98
s	0.59	0.08	0.43	0.76
k	0.55	0.08	0.39	0.71
e	0.97	0.03	0.91	1.00

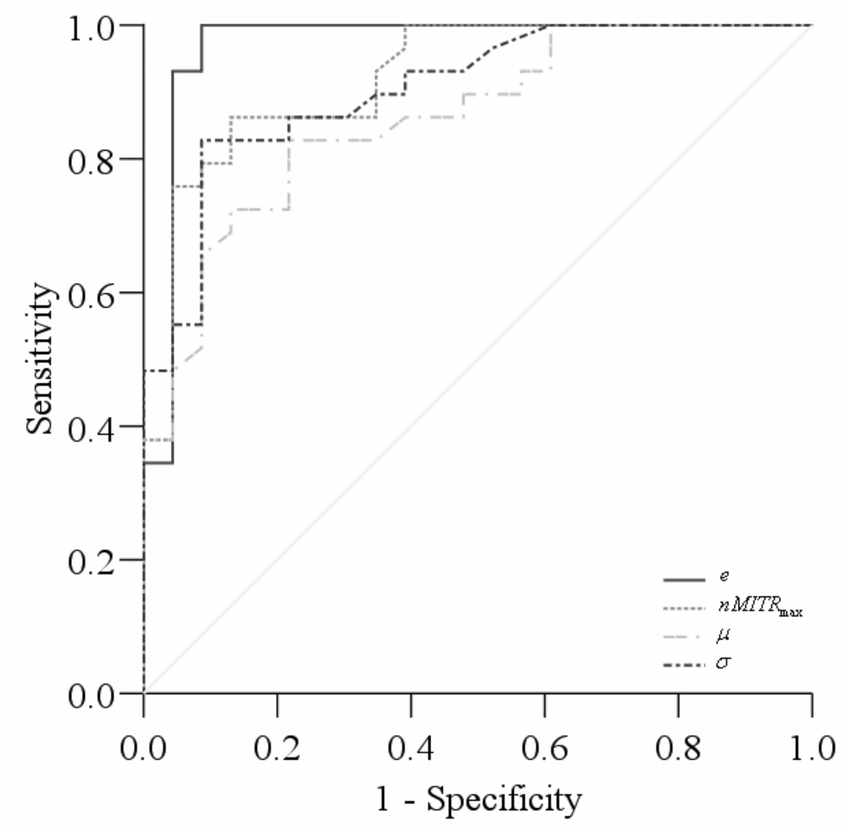

Figure 6.5 ROC curves of the significant features: The maximum nMITR, the mean nMITR, sd of nMITR and nMITR-entropy.

6.10 Discussion

In clinical practice, lesion enhancement analysis starts by manually placing a couple of 2D ROIs on the most suspicious areas of the early post contrast images that show high enhancements after a visual inspection of the acquired images and only a few measurements are used to assess a 3D lesion. Placement of these ROIs is critical and requires lots of experience to achieve reproducible results. For automated ROI placement, the suspected regions must be volumetrically segmented; a difficult and time-consuming process if performed manually. Some region growing and thresholding algorithms have been developed as a partial solution to this problem [5, 6, 20, 30, 84]. These techniques require user supplied information such as a seed point or a threshold value to localize a lesion. In the present study, we describe a novel, fast volumetric lesion segmentation method that requires user interaction only during initialization to roughly mark a rectangular prism VOI covering a suspicious region; the lesion is then automatically identified within milliseconds.

For assessing the identified lesions as benign or malign, a small sampling mask is moved to through the entire VOI, voxel by voxel to obtain accurately samples, enhancement characteristics and an nMITR projection of the tissues involved. Diagnostic relevance of statistical parameters extracted from the generated nMITR projection is studied in detail. The maximum, the mean, the standard deviation and the entropy of the nMITR are found to be highly significant; the skewness and the kurtosis are found to be insignificant. The significance of the mean and the maximum value have been reported earlier [16, 31, 32, 33, 34, 35]; however, standard deviation and entropy have not been reported. In our work, the significance of the standard deviation and the maximum are found to be similar and that of the nMITR-entropy is found to be the most significant. In general, the significance of the parameters studied in this work are found to be greater than those reported in the literature due to the 3D nature of our method, the use of the voxel sampling via moving masks and the use of high resolution images.

Current methods for evaluation of lesions in MR mammography are mostly subjective and require a great deal of user experience to avoid false positive biopsies. To reduce unnecessary biopsies, enhancement analysis must use quantitative methods and must be standardized. Due to the quantitative and the standardized nature of the technique introduced in this work, we expect that its use will result in increased diagnostic reproducibility and improved overall performance especially for clinically and mammographically occult lesions. Our results demonstrate that benign lesions can be discriminated from malign lesions accurately using the nMITR-entropy, the most significant and diagnostically accurate parameter among the parameters studied in this work. The use of this parameter and the technique introduced in this work will certainly be very helpful during decision making, surgical planning and in predicting the extent of residual disease after neoadjuvant chemotherapy.

In conclusion, our findings demonstrate usefulness of the nMITR features, illustrate improvements in the diagnostic accuracies achievable with high resolution images and enhancement measurements of each tissue inside a volumetrically segmented breast lesion using voxel sampling based on a moving mask. The proposed method is robust, efficient and reliable in terms of observer variability, allows better standardization of the evaluations, and appears promising. However, generalization of the results requires further testing on large number of cases, lesion sizes and subgroups, reproducibility, applicability to other populations and other MRI systems. For future work, we are planning a multicenter study to expand our database and design a classification scheme that also considers lesion morphology hoping to further improve the performance of diagnosis by detecting rapidly enhancing fibroadenomas.

7. MORPHOLOGICAL DESCRIPTORS FOR MALIGNANCY DETECTION

7.1 Introduction

Dynamic Contrast-enhanced MR-Mammography (DCE-MRM), when compared with X-ray mammography, offers an alternative imaging technology that has sufficient potential for detection and noninvasive characterization of breast cancer [106]. It does not use ionizing radiation and hence is particularly suitable for young women, who tend to have dense breasts. Since there is no need for excessive breast compression during imaging, lesion-obscuring overlapping structures and summation shadows are much less pronounced in comparison with X-ray mammography. DCE-MRM makes possible accumulation of a wealth of information on the investigated lesion including tissue relaxation times and perfusion as revealed by contrast enhancement dynamics as well as morphology which are representative of the histologic features of lesions [75].

Morphological characteristics of lesions in DCE-MRM contain important diagnostic information and can be used for discriminating malignancy. Typically, irregular morphology, irregular or spiculated margins, heterogeneous internal enhancements and rim enhancements are signs of malignancy while smooth margins and homogenous internal enhancements are associated with benign lesions [14]. A number of researchers analyzed the diagnostic usefulness of qualitatively assessed morphological parameters. Using their own architectural interpretation model, Nunes et al [15] reported that negative predictive value for malignancy for smooth margins was 95% and for lobulated margins 90%, while for irregular and spiculated margins, positive predictive value for malignancy was 84% and 91%, respectively. Wedegartner et al [17] demonstrated significance of irregular lesion contour and shape. Using an artificial neural network, Szabo et al [16] showed that discriminative ability of morphologic parameters such as lesion margins, homogeneity, presence of ring enhancement and septations are comparable to that of an expert radiologist. However, qualitative assessment of lesion morphology is highly time-intensive, experience dependent and inter-observer variable, especially when lesion volumes are considered. Therefore, during the past decade, quantification of lesion morphology has been studied by a number of researchers. A summary of these studies is presented in Table 7.1.

Table 7.1
Summary of significant descriptors discussed in literature.

Reference	Number of Cases	Dimension	Significant Descriptors	*P*-value	Accuracy
[18]	33 (M:15 B:18)	3D	Spherical shape index	0.0063	NA
[19]	80 (M:40 B:40)	3D	Smoothness of uptake Mean margin sharpness	NA NA	0.71 0.70
[20]	14 (M:10 B:4)	2D	Combined feature set including 5 parameters (Curvature, eccentricity, filled area, solidity and gray level threshold value)	NA	0.91
[21]	47 (M:32 B:15)	2D	Convexity Complexity	0.001 0.044	NA NA

M: Malignant, B: Benign, NA: not available

Shahar et al [18] calculated volume-to-surface area ratio and spherical shape index measures from boundaries of 33 breast lesions (15 malignant and 18 benign) represented by triangular meshes a using an interactive volume rendering software. Only spherical shape index was found to be a significant discriminator of malignancy (*P*=0.006). Gilhuijs et al [19] computed mean margin sharpness, variation in margin sharpness and smoothness of uptake from 80 lesions (40 malignant and 40 benign). For each case, a seed point within the lesion was manually marked on the subtraction images and the lesion volume was segmented automatically. Smoothness of uptake and the mean margin sharpness were the significant features (maximum accuracy: 0.71 and 0.70, respectively). Tzacheva et al [20]computed curvature scalar, eccentricity, filled area and solidity of 14 lesions (10 malignant and 4 benign) on fat-suppressed late post-contrast images. Lesions were segmented by manually selecting signal intensity thresholds. These descriptors and selected threshold values were supplied to a feed forward neural network to discriminate malignancy. They achieved an accuracy of 0.912. Liney et al [21] calculated convexity, complexity, circularity and elongatedness from fat-suppressed late post-contrast images of 47 lesions (32 malignant and 15 benign) in which the lesions had the maximum diameter. Lesion boundaries were drawn manually or were extracted by a semi-automated algorithm after selection of an intensity threshold value. 2D convexity was the most significant parameter for both methods (P=0.006 and P=0.001, respectively) while the automated method had significantly different values of complexity (P=0.044).

In the present study, we introduce a novel measurement method that provides an objective, consistent and accurate way to extract principal morphological features of lesions in discrimination of malignancy. It is based on normalized maximum intensity time ratio (nMITR) maps of roughly marked rectangular prism volume of interest (VOI) that suitably covers a lesion. Using this VOI data, the lesion is segmented volumetrically and the morphological descriptors are extracted.

7.2 Patients and Lesions

DCE-MR imaging was performed for 51 women (age: 28-83 years; mean age: 46 years) to clarify uncertain clinical, mammographical or sonographical findings and to assess preoperative staging of patients with known malignancies. Informed consent explaining the nature of the imaging procedure was secured from each patient. 26 benign and 32 malignant lesions, confirmed by histopathological examination or clinical follow-up, were retrospectively included in the study.

7.3 MR Imaging Protocol

Imaging was conducted using a 1.5 Tesla MR scanner (Symphony; Siemens AG, Medical Solutions, Erlangen, Germany). Patients were positioned prone with the breast to be imaged in gentle compression within a commercially available 4-channel phased-array breast coil of the same manufacturer. Dynamic data was captured using a T_1-weighted fast spoiled gradient-echo sequence (3D FLASH) in the axial plane with TR/TE= 9.80/4.76 ms, flip angle= 25^o, a 512×512 matrix and 0.625×0.625 mm^2 resolutions in the x and y directions, 2.5 mm slice thickness with no gap. An intravenous bolus of 0.1 mmol/kg body weight of Gd-DTPA (Magnevist, Schering) was administered for enhancing contrast. One pre-contrast and five post-contrast images were acquired for each image slice. 12-bit grayscale image sets were transferred from the MR scanner to a personnel computer in DICOM format for subsequent analysis.

7.4 Lesion Localization

To localize lesions *DynaMammoAnalyst,* a special 32-bit software written by the authors in Borland Delphi 7.0 (Borland Software Cooperation, Inc., USA) is used. The software provides acquired pre and post-contrast images, subtraction images, maximum intensity images (MIIs) and uniquely color-coded maps of normalized maximum intensity time ratio (nMITR). For each slice, subtraction images and MII are generated by processing pre and post contrast images pixel-by-pixel. The nMITR map is calculated using a 3×3 pixel moving window, $\Re$ [34]:

$$nMITR = \frac{I_{\max}(\Re) - I_0(\Re)}{I_0(\Re) \times T_{\max}} \tag{7.1}$$

where $I_0(\Re)$ and $I_{\max}(\Re)$ are the average intensity of the pre-contrast image and maximum average intensity among the post-contrast images. $T_{\max}$ denotes the time (in seconds) when the average intensity reaches to its maximum. nMITR maps are displayed in HSV color format; values lower than 0.14 sec^{-1} are shown in blue while values higher than a threshold (default value 0.27 sec^{-1}) are displayed in red. This threshold should be interactively adjusted by an expert radiologist carefully to distinguish a lesion from its surrounding normal parenchyma and moderately enhanced blood vessels.

For a localized lesion, using *DynaMammoAnalyst* the expert roughly marks a rectangular prism volume of interest (VOI) that suitably covers the lesion based on the nMITR maps by supplying its width, height, starting and ending slice numbers and the coordinates of the upper leftmost pixel. This VOI data is used during volumetric segmentation of the lesion to extract morphological descriptors.

7.5 Extraction of Morphological Descriptors

To extract potential morphological descriptors in discrimination of malignancy, we developed a fully automated software called *MorphoAnalyst* using Matlab Image Processing Toolbox (The Mathworks, Inc., USA). This software assigns labels to objects inside the supplied VOI by using 18-pixel neighbor connectivity search and performs volume thresholding to detect lesions and to eliminate blood vessels. Holes within a detected lesion are filled to include necrotic tissue with low nMITR and morphological descriptors of the segmented lesion volume are extracted. The software also determines the representative slice in which the lesion has the largest diameter and computes its morphological descriptors. These descriptors are convexity, complexity, extent, eccentricity and enclosed area to contact surface area ratio as explained next.

7.5.1 Convexity

Convexity (also called as solidity in [20]) is a measure of roundedness of a lesion. For 2D, it is defined as the ratio of the lesion area A_L, to the area of the convex hull, A_{CH}, [21]:

$$Convexity^{2D} = \frac{A_L}{A_{CH}} \tag{7.2a}$$

For 3D convexity is defined as the ratio of the lesion volume, V_L to the volume of the convex hull, V_{CH}.

$$Convexity^{3D} = \frac{V_L}{V_{CH}} \tag{7.2b}$$

7.5.2 Extent

Extent (also called compactness in [118]) is a measure of the flatness of a lesion. For 2D, it is defined as the ratio of the lesion area to the area of the bounding box, A_{BB} :

$$Extent^{2D} = \frac{A_L}{A_{BB}} \tag{7.3a}$$

For 3D, it is defined as the ratio of the lesion volume to the volume of the bounding box, V_{BB} .

$$Extent^{3D} = \frac{V_L}{V_{BB}} \tag{7.3b}$$

7.5.3 Normalized Complexity

Normalized complexity is a measure of irregularity of lesion border and for 2D is calculated from lesion area, A_L and the lesion perimeter p using[3] [21]:

$$nComplexity^{2D} = 1 - \frac{4\pi \times A_L}{p^2} \tag{7.4a}$$

Inspired from the above definition, we define 3D normalized complexity as:

$$nComplexity^{3D} = w_a \times \overline{nComp_a} + w_s \times \overline{nComp_s} + w_c \times \overline{nComp_c} \tag{7.4b}$$

where the subscripts *a, s* and *c* correspond to axial, sagittal and coronal views. $\overline{nComp_j}$, $(j = a, s, c)$ represents the average normalized complexity calculated over the

---

[3] In [21] complexity is defined as $\frac{4\pi \times A_L}{p^2}$.

slices in which the lesion area is larger than 9mm^2. The weights $\mathbf{w} = \begin{bmatrix} w_a & w_s & w_c \end{bmatrix}$ are determined from the following rules:

1. if $\overline{nComp_a}$, $\overline{nComp_s}$ and $\overline{nComp_c}$ are available then $\mathbf{w} = \begin{bmatrix} 4/6 & 1/6 & 1/6 \end{bmatrix}$
2. if $\overline{nComp_a}$ and $\overline{nComp_s}$ are available then $\mathbf{w} = \begin{bmatrix} 4/5 & 1/5 & 0 \end{bmatrix}$
3. if $\overline{nComp_a}$ and $\overline{nComp_c}$ are available then $\mathbf{w} = \begin{bmatrix} 4/5 & 0 & 1/5 \end{bmatrix}$
4. if only $\overline{nComp_a}$ is available then $\mathbf{w} = \begin{bmatrix} 1 & 0 & 0 \end{bmatrix}$

The weights in the above rules follow from the fact that images are acquired in the axial plane with an isotropic resolution and the fact that the slice thickness is four times greater than the in-plane resolution.

7.5.4 Eccentricity

Eccentricity expresses elongatedness of a lesion and ranges from 0 (round) to 1 (elongated). It is defined as the ratio of the distance d_f, between the foci of the ellipse and its major axis length d_m [20]:

$$Eccentricity^{2D} = \frac{d_f}{d_m} \tag{7.5a}$$

For a 3D image we have an ellipsoid instead of an ellipse and we define eccentricity as the ratio of the distance d_F between the greatest foci of the ellipsoid bounding the lesion to its major axis length d_m.

$$Eccentricity^{3D} = \frac{d_F}{d_m} \tag{7.5b}$$

7.5.5 Enclosed Area to Contact Surface Area Ratio

Enclosed area to contact surface area ratio, *CSAR* is a measure of lesion surface irregularity in 3D and is defined as [119]:

$$CSAR = \frac{n \times a_v}{A_c} - 2 \tag{7.6a}$$

where A_c is the contact surface area calculated by summing the areas of the contact surfaces which are common to two voxels, n is the number of voxels that composes the lesion and a_v is the total area of the six faces of a typical voxel computed using

$$a_v = 2 \times \left(r_x \times r_y + r_x \times r_z + r_y \times r_z \right) \tag{7.6b}$$

r_x and r_y are the resolutions of the imaging protocol in the x and y directions, respectively and r_z is the slice thickness.

7.6 Statistical Analysis

To study the effectiveness of the descriptors, statistical analyses of the computed descriptors for the benign and malignant groups are carried out using SPSS 14 (SPSS Inc., USA). The independent samples t-test with either a pooled or separate variance as determined by the Levene's test for equality of variances is performed. A P-value of <0.05 is considered statistically significant. Receiver operating characteristic (ROC) curves are plotted and the areas under the ROC curves (AUC) are used as an index of diagnostic accuracy.

The cut-off values of the diagnostic descriptors can be determined using utility-based decision theory in combination with ROC analysis. Criteria such as Youden index, odds ratios and kappa index as a function of sensitivity (*Se*) and specificity (*Sp*) pair provides practical solutions [117]. In this study, the following optimality function is used for the most diagnostic descriptor [120]:

$$J(Se, Sp) = Se + \left[\frac{(1-P)}{P} \right] \times \left[\frac{(C_{FP} - C_{TN})}{(C_{FN} - C_{TP})} \right] \times (Sp - 1) \tag{7.7}$$

where P is the expected prevalence of malignancy in the study dataset and C_{FP}, C_{FN}, C_{TN} and C_{TP} are the costs of false-positive, false-negative, true-negative and true-positive decisions, respectively. We assign no cost to correct decisions and same cost to incorrect decisions; i.e., $C_{FP} = C_{FN} = 1$ and $C_{TN} = C_{TP} = 0$. The cut-off value for which *Se* and *Sp* maximizes J is determined as the optimal cut-off $\hat{T}$. Additional diagnostic characteristics of the descriptor at $\hat{T}$ are assessed by *PPV* and *NPV* (positive and negative predictive values) calculated using:

$$PPV = \frac{Se \times P}{Se \times P + (1 - Se) \times (1 - P)} \tag{7.8a}$$

$$NPV = \frac{Sp \times (1 - P)}{Sp \times (1 - P) + (1 - Se) \times P} \tag{7.8b}$$

The performance of the descriptor for $\hat{T}$ is assessed by the diagnostic characteristics such as sensitivity, specificity, positive and negative predictive values.

7.7 Results

Using *DynaMammoAnalyst,* DCE-MRM data from 51 women is explored and 58 lesions (26 benign and 32 malignant) are localized. Rectangular prism volume of interests (VOIs) that suitably cover lesions are roughly marked by an expert radiologist on the nMITR maps. Lesions within the VOIs are segmented in 3D and morphological descriptors are extracted using *MorphoAnalyst*. Convexity, normalized complexity, extent and eccentricity are computed in 2D, using the representative slices in which the lesions have the largest diameters. The 3D versions of these descriptors and enclosed area to contact surface area ratio (*CSAR*) are also computed from segmented lesions.

For illustrating the technique two typical lesions; a benign lesion (fibroadenoma) and a malignant lesion (invasive lobular carcinoma) are considered. The maximum intensity images of the representative slices for each lesion are presented in Figures 7.1a and 7.1b. The benign lesion appears as a lobulated area of homogeneous enhancement while the malignant lesion has inhomogeneous enhancement and has a distinctly irregular shape and spiculated margins. The nMITR maps are shown in Figures 7.2a and 7.2b. The benign lesion occupies 4 slices and the malignant lesion resides in 6 slices. Figures 7.3 and 7.4 show the VOIs marked by the expert and the results of volumetric segmentation. The malignant lesion occupies a volume of 2.10cm^3 and the benign lesion 0.36cm^3. Computed diagnostic morphological descriptors of these lesions are summarized in Table 7.2.

Table 7.2
2D and 3D descriptors computed for two representative lesions (benign and malignant).

Descriptor	Benign	Malignant	Comments
Convexity	0.95	0.91	Low values indicate malignancy
Extent	0.71	0.72	Low values indicate malignancy. However, in this representative slice this measure does not properly reflect the aggressiveness of the lesion
nComplexity	0.19	0.24	High values indicate malignancy
Eccentricity	0.85	0.66	Low values indicate malignancy
$Convexity^{3D}$	0.94	0.82	Low values indicate malignancy
$Extent^{3D}$	0.47	0.37	Low values indicate malignancy
$nComplexity^{3D}$	0.23	0.31	High values indicate malignancy
$Eccentricity^{3D}$	0.88	0.82	Low values indicate malignancy
CSAR	0.38	0.21	Low values indicate malignancy

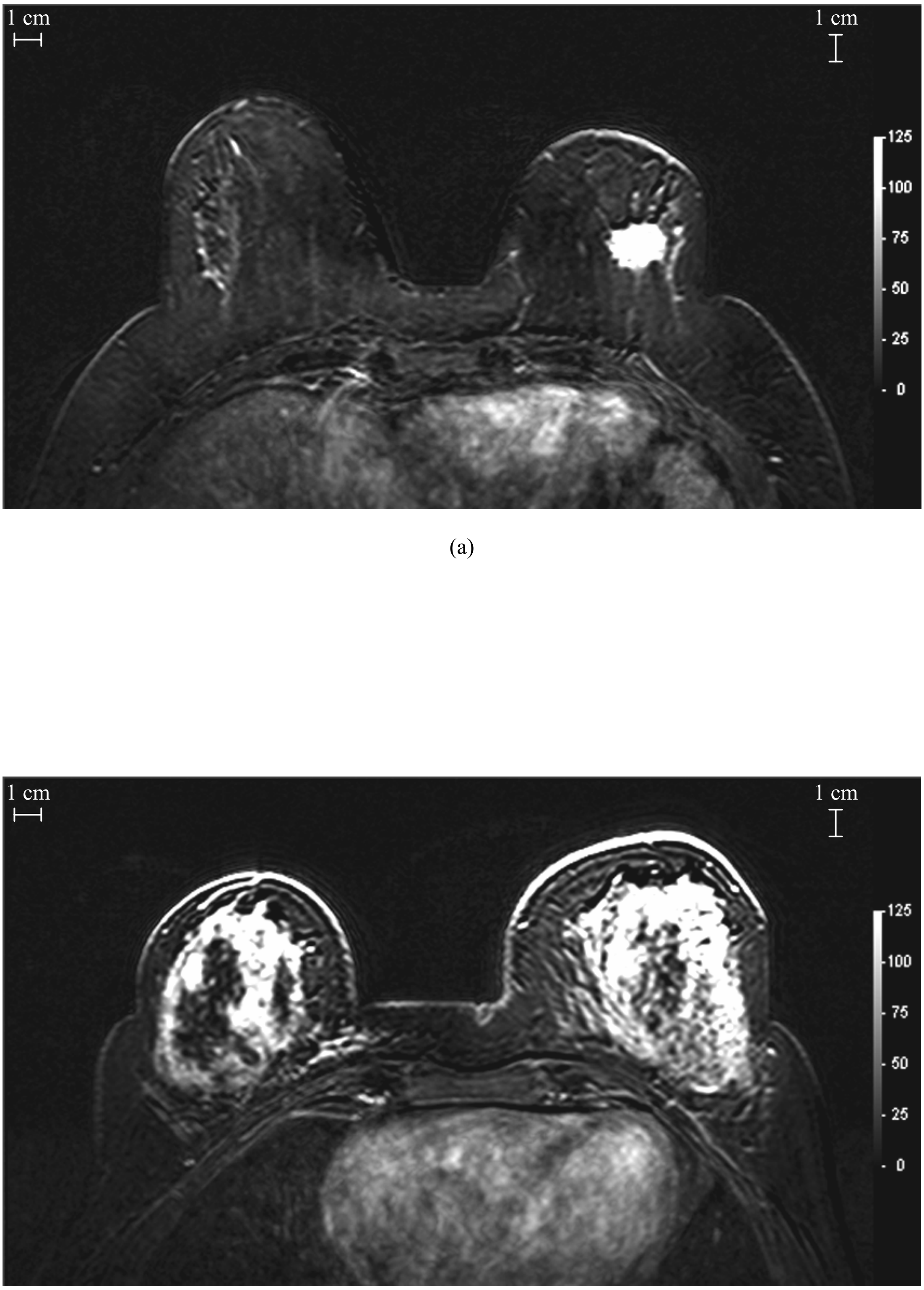

(b)

Figure 7.1 The maximum intensity images for representative lesions: (a) malignant, (b) benign.

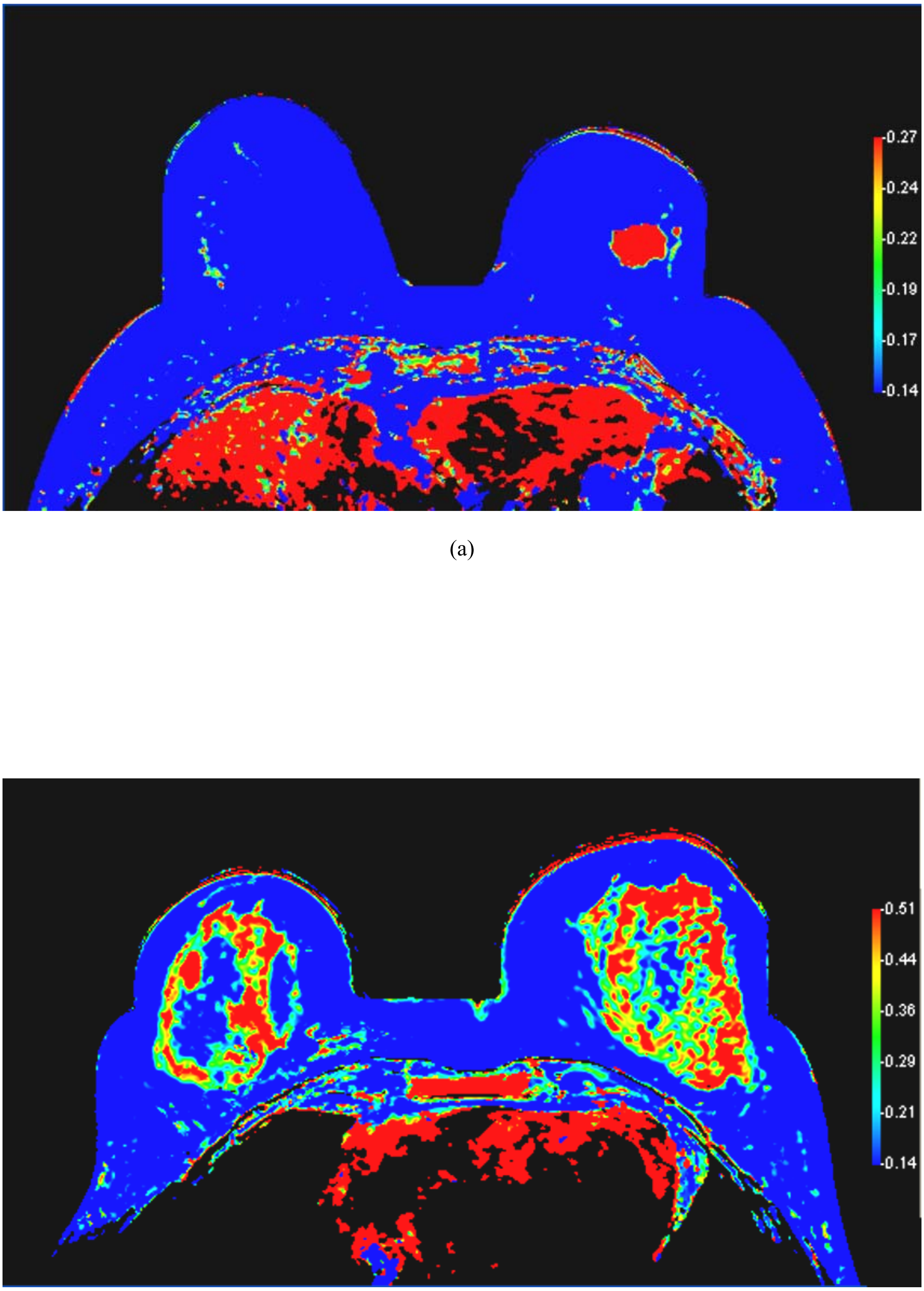

(a)

(b)

Figure 7.2 nMITR maps for representative lesions: (a) malignant, (b) benign.

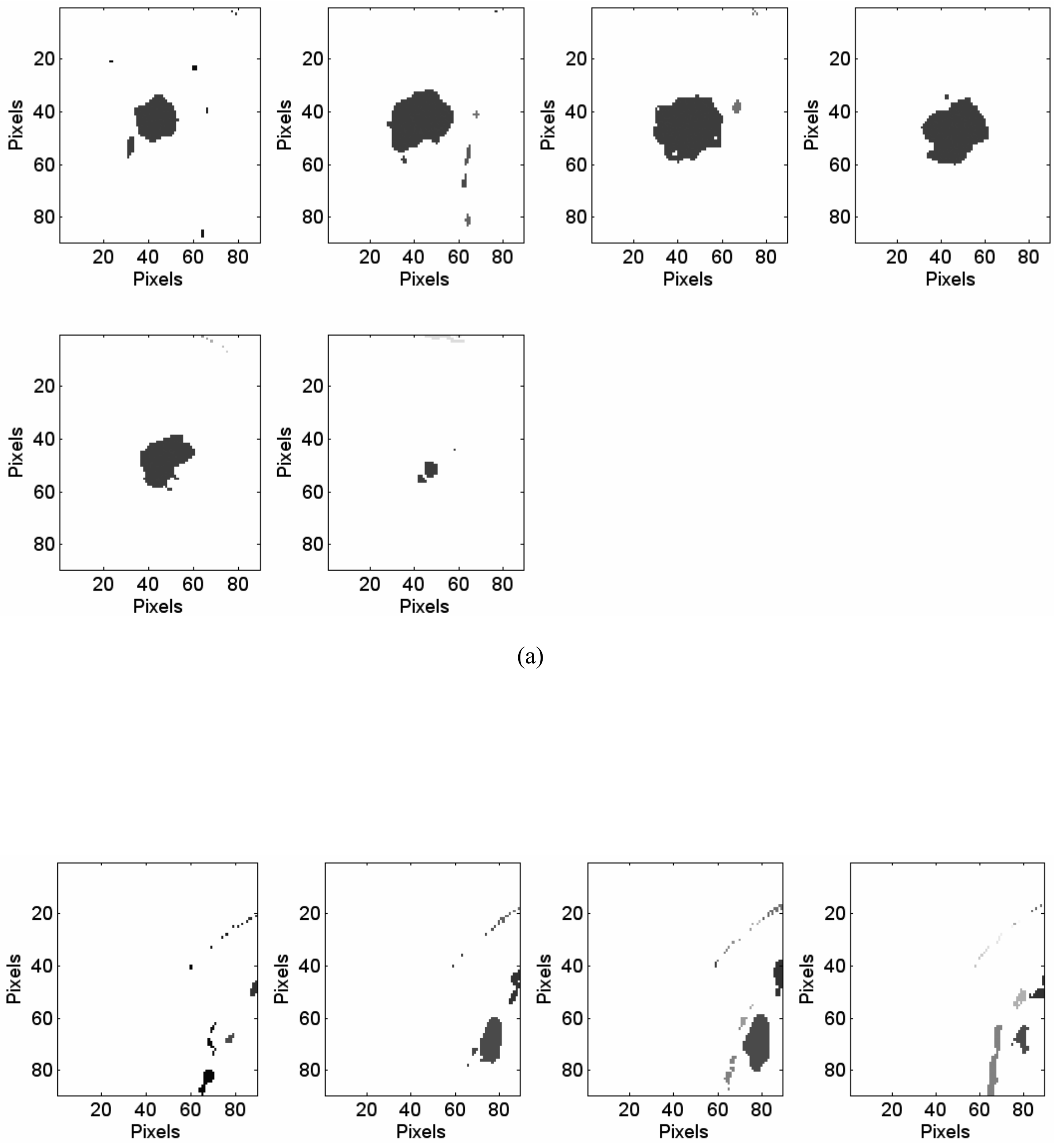

(a)

(b)

Figure 7.3 Slice view of selected VOIs for representative lesions: (a) malignant, (b) benign.

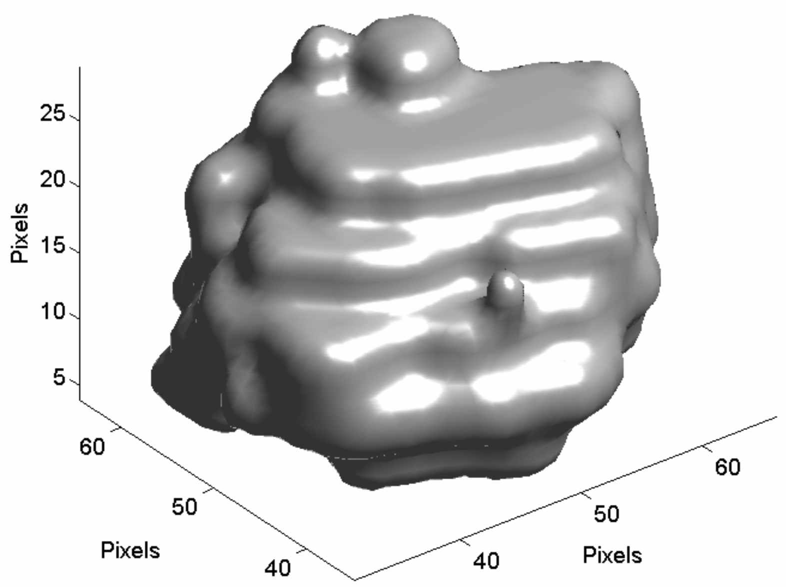

(a)

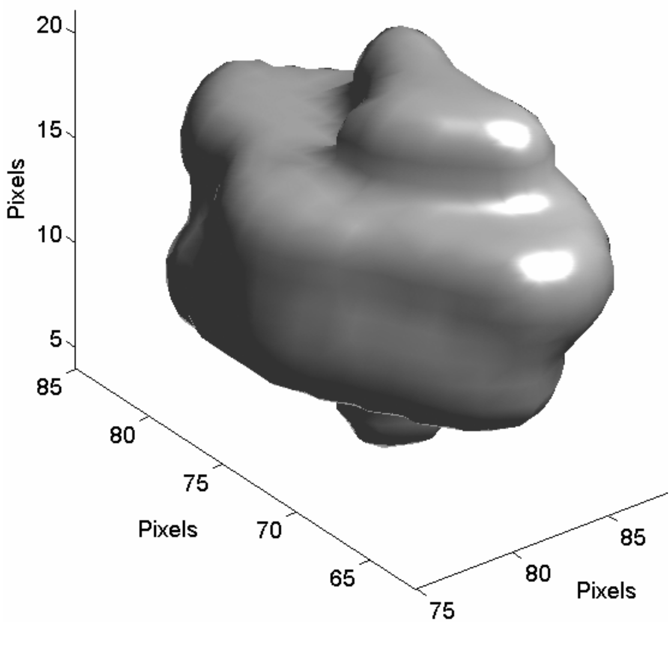

(b)

Figure 7.4 Segmented 3D views of representative lesions: (a) malignant, (b) benign.

The results of statistical analyses of the computed descriptors for the benign and malignant groups are given in Table 7.3. Malignant lesions are distinguishable from benign lesions with lower values of convexity, extent, eccentricity and contract surface area ratio and higher values of complexity. Student t-test results show that when measurements in 2D are considered, there are significant differences between the benign and malignant lesions in terms of convexity (0.88±0.07 and 0.82±0.10, P=0.005), complexity (0.31±0.19 and 0.47±0.20, P=0.002) and extent (0.64±0.09 and 0.59±0.10, P=0.045). Eccentricity is the insignificant descriptor (P> 0.05). Measurements in 3D lead to several improvements: higher significances are obtained for convexity (0.90±0.19 and 0.72±0.13, P<0.001), complexity (0.32±0.15 and 0.45±0.13, P=0.001), extent (0.42±0.11 and 0.34±0.09, P=0.006) and eccentricity (0.83±0.09 and 0.76±0.10, P=0.018). The descriptor for differentiating benign lesions from malignant lesions with the highest significance is found to be the contact surface area ratio (0.43±0.14 and 0.27±0.08, P< 0.001).

Table 7.3
Mean values of the 2D and 3D descriptors computed for the dataset.

Descriptor	Benign (N= 26) Mean ± Std.Dev.	Malignant (N= 32) Mean ± Std.Dev.	*P*-value
Convexity	0.88 ± 0.07	0.82 ± 0.10	0.005
Extent	0.64 ± 0.09	0.59 ± 0.10	0.045
nComplexity	0.31 ± 0.19	0.47 ± 0.20	0.002
Eccentricity	0.70 ± 0.17	0.67 ± 0.14	0.392
$Convexity^{3D}$	0.90 ± 0.19	0.72 ± 0.13	< 0.001
$Extent^{3D}$	0.42 ± 0.11	0.34 ± 0.09	0.006
$nComplexity^{3D}$	0.32 ± 0.15	0.45 ± 0.13	0.001
$Eccentricity^{3D}$	0.83 ± 0.09	0.76 ± 0.10	0.018
CSAR	0.43 ± 0.14	0.27 ± 0.08	< 0.001

The results of ROC analysis for significant descriptors are presented in Table 7.4. Among these descriptors, the *CSAR* stands out in terms of its higher diagnostic accuracy

(0.87). In comparison, accuracies of the other descriptors (convexity, complexity and extent) are lower and range between 0.81 and 0.66. Another observation that can be deduced from this table is that, in discriminating malignancy, the 3D descriptors perform better than the 2D descriptors. Sensitivity, specificity and optimality function plots for *CSAR* are presented in Figure 7.5. From this figure, the optimal threshold is determined to be 0.30. At this threshold, the *CSAR* achieves 92% specificity, 72% sensitivity, 92% positive predictive value and 73% negative predictive value.

Table 7.4
Summary of the ROC analyses.

			95% CI of AUC	
Descriptor	AUC	Std. Error	Lower Bound	Upper Bound
CSAR	0.87	0.05	0.77	0.97
Convexity^{3D}	0.81	0.06	0.69	0.93
nComplexity^{3D}	0.74	0.07	0.61	0.87
Extent^{3D}	0.72	0.07	0.58	0.86
nComplexity	0.71	0.07	0.57	0.85
Convexity	0.70	0.07	0.56	0.83
Eccentricity^{3D}	0.68	0.07	0.54	0.82
Extent	0.66	0.07	0.56	0.83

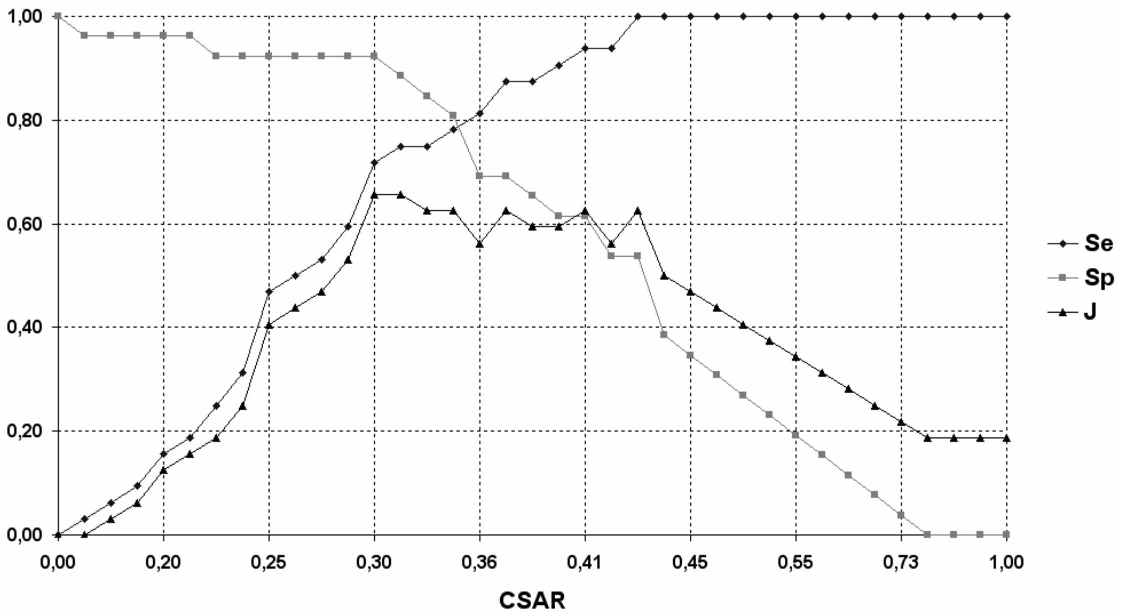

Figure 7.5 Sensitivity, specificity and optimality function plots of *CSAR*.

7.8 Discussion

Morphological characteristics of lesions in DCE-MRM contain important diagnostic information and can be used for assessing breast abnormalities. For example, irregular shape, irregular or spiculated margins, heterogeneous internal enhancements and rim enhancements are signs of malignancy while smooth margins and homogenous internal enhancements are associated with benign lesions.

Recently, a number of quantitative methods have been developed to detect malignancy based on lesion morphology. Diagnostically useful information is commonly extracted using delayed fat suppressed post-contrast images or subtraction images that are helpful to suppress less enhancing normal parenchyma and to highlight avidly enhancing regions. In this study, we introduce a novel method that is based on the use of nMITR maps. These maps, generated from dynamic MRM datasets, do not require prior fat suppression or superb homogeneity and moreover, can improve contrast by suppressing enhancements of blood vessels and normal parenchyma that surround the lesions and therefore are especially advantageous during evaluation premenopausal women.

In a majority of previous morphological studies, lesion assessment is carried out using morphological measures from a “representative” slice in which the lesion has the largest diameter. In one study, a neural network, trained by a feature vector consisting of curvature, eccentricity, gray-level threshold, filled area and solidity is demonstrated to have high diagnostic accuracy on a limited data set of 14 lesions [20]. In another study, the value of complexity, convexity, circularity and degree of elongation in discrimination of malignancy is compared [21]. Convexity and complexity are found to be the significant measures. Our results from convexity, normalized complexity, extent and eccentricity measurements in 2D verify these findings. Moreover, due to the special technique used we achieve higher significance figures.

Morphological studies have recently been extended to volumetrically segmented lesions. In one study, a spherical shape index is reported to have high significance [18], while in another study smoothness of uptake and mean margin sharpness are shown to have good diagnostic accuracies [19]. When compared with these findings, the 3D morphological descriptors introduced in this study, namely, contact surface area ratio, convexity, complexity and extent have higher significances and accuracies (see Table 7.1). In other words, 3D morphological analysis provides a better way to reflect aggressiveness of malignant lesions than 2D analysis.

In conclusion, our results illustrate that the 3D morphological descriptors extracted from the nMITR maps have improved diagnostic performance in discrimination of malignancy; they are efficient and allow better standardization. Among these, the contact surface area ratio has the highest significance and highest diagnostic accuracy; it can be computed easily and is adaptable to any imaging protocol. Morphological descriptors of small lesions or large but lobulated lesions alone may not be sufficient to successfully discriminate malignancy. For such cases, during decision-making, it may be useful to exploit morphological descriptors as well as the dynamic enhancements properties.

8. DECISION SUPPORT SOFTWARE FOR MR MAMMOGRAPHY

8.1 Introduction

MR mammography (MRM) is gaining increased acceptance for detecting breast cancer in its early stages since lesion-obscuring overlapping structures and summation shadows are much less pronounced, as there is no need for excessive breast compression during imaging. It does not use ionizing radiation and hence is particularly suitable for young women, who tend to have dense breasts [106]. With the help of contrast agents that reveal the state of angiogenesis, MR mammography provides important tissue information on cross-sectional morphology, as well as functional information on perfusion and capillary leakage and thus makes possible localization, visualization and assessments of the aggressiveness and multifocality of the breast lesions [75]. Moreover, among the currently available breast imaging techniques such as "X-ray mammography, high frequency breast ultrasound, positron emission tomography and scintimammography, MR mammography offers the highest sensitivity for invasive breast cancer" [3].

For accurate assessment of cancer, a large volume of image data produced with high spatial and temporal resolutions must be analyzed. Acquired T_2-weighted images, pre and post-contrast T_1-weighted images and subtraction images created from the dynamic data should all be inspected by the radiologist carefully slice by slice to identify suspicious regions. This is a very time consuming task and a heavy workload, as these regions can be very small and there may be several deceptively enhanced healthy regions such as blood vessels and normal parenchyma especially in case of premenopausal women. To obtain optimal malignancy discrimination, the morphology and the enhancement dynamics of every suspicious region identified as a lesion, should be carefully evaluated visually [121].

Typically, irregular morphology, irregular or spiculated margins, heterogeneous internal enhancements and rim enhancements are signs of malignancy, while smooth margins and homogenous internal enhancements are associated with benign lesions. Rapid enhancement suggests in most cases malignant lesions and gradual enhancement suggests usually benign lesions [14]. A simple and therefore common technique for enhancement dynamics is the evaluation of the shape of a representative "time–signal intensity curve" of the lesion. To initiate this, the radiologist should place a small region of interest (ROI) over the most rapidly and intensely enhancing component of the lesion [22]. Utmost care is a must during the positioning of the ROI, since missing of a very small detail may result in poor specificity and sensitivity in the final diagnosis. The user must also be familiar with the TICs of malignant and benign lesions to make accurate decisions. Due to the enormous image data that must be processed and interpreted, a typical manual patient evaluation requires constant and diligent attention of the radiologist for periods exceeding 30 minutes.

For improved diagnosis, a number of quantitative methods have been developed that make use of a number of protocols and interpretation criteria such as eccentricity, solidity, maximum enhancement rates at specific times, time to maximum enhancement and washout ratio, etc., [20, 25, 122,123]. Among them, complexity and normalized maximum intensity-time ratio, computed from a "representative" image from the acquired images, fat suppressed images or first subtraction images of a lesion, have been shown to be important criteria [21, 35]. However all these methods are far from practical use and undoubtedly, there is a great need for software packages that automatically extract important diagnostic features of the image data and present them to the radiologists for decision support in the clinical practice.

A pioneering work toward this goal was carried out by Leach et al, who developed MRIW, a software to quantify contrast agent in dynamic contrast-enhanced MR images [6]. Five parameters, onset time (time taken to reach 10% enhancement), initial gradient (rate of increase in signal intensity at the 10% point), mean gradient (mean rate of signal intensity increase between the 10% point and the 90% point), maximum enhancement and wash-out rate were calculated pixel-by-pixel to generate color maps visualizing highly enhancing breast tissues with manual thresholding. These maps provided valuable information during the subjective placement of ROIs. The software was equipped with a facility to display the histogram of the distribution of the relevant parameter within a drawn ROI.

In a recent software, reported by Subramanian et al. [36], the user is interactively allowed to specify a TIC that represents malignancy. A similarity confidence degree is then automatically assigned to each voxel and displayed in different intensities of red. Alternatively, the user could manually identify a suspicious region and draw an ROI inside it; the software then plots its TIC. Since lesions with different TICs may be missed, this system has limited lesion detection capability.

MTDYNA (Mevis Inc, Bremen, Germany) is another software that generates color parametric maps of relative changes in intensity of each pixel over time. Three time points are used to determine the color-coding; the precontrast, the first post-contrast and the final time point. Enhancement of the initial post-contrast time point relative to the baseline pre-contrast time point determines an initial color category. The final displayed colors for each pixel are determined by the rate of enhancement change between the initial post-contrast and last post-contrast points. The software has a commercial version called DynaCAD (Invivo Copr., Orlando, FL). It has improved capabilities; eleven parameters (maximum enhancement, enhancement at a time point, value at time point, two phase –the method of MTDYNA-, time to peak, maximum intensity-time ratio, maximum descent, maximum slope, mean transit time and integral) are calculated pixel-by-pixel. For better evaluation of suspicious enhancements, a manually selected threshold value must be supplied. Wiener et al report that the use of the software decreases interpretation time for a case to approximately 5 min. while detecting malignant lesions Achieved diagnostic accuracy was 89% [7].

fTP (CAD Sciences Inc, White Plains, NY) is a software that utilizes a parametric mapping method based on pharmacokinetic analysis. Vessel permeability and extra-cellular volume are calculated pixel-by-pixel by fitting a curve over all available time points. Tissue physiology histogram and fTP colorized images are the visual outputs. The software provides a direct link between histogram plot and pixel location in the colorized image. In a clinical study, the mapping method is demonstrated to have 96% sensitivity and 82% specificity in solid lesions detection [4].

CADstream (Confirma Inc, Kirkland, WA) is another software that produces colored images to identify areas of significant enhancement after pixel by pixel analysis. In addition, it provides details about regions that show significant enhancement. Once the user selects a specific area showing significant enhancement, the program automatically generates a synopsis of the full volume of that region, including the percentage of the tissue that shows wash-out, plateau and persistent enhancement. Lehman et al studied the benefits of these percentages in discrimination of breast cancer. They used threshold values of 25%, 50% and 100% enhancement. All malignant lesions showed significant enhancement at all thresholds. Computer-assisted analysis yielded false positive rates that were reduced by 25%, 33% and 50% for each threshold, respectively. There were no significant differences found between enhancement profiles of benign and malignant lesions. All lesions showed a wide range of wash-out, plateau and persistent patterns of enhancement [5].

All these computerized methods try to overcome difficulties associated with subjective ROI analysis using several enhancement parameters. However, a manually selected threshold value that significantly affects the performance of lesion characterization is still a requirement. MRIW and CADstream differ from the other software since they also provide lesion identification and enhancement distributions. To do this, the radiologist must first draw an ROI, encompassing the whole lesion appropriately or must mark the lesion. To make correct decisions however he/she must be familiar with the distribution data of malignant and benign lesions. This subjective nature of the assessment clearly results in increases inter-observer variability.

In this thesis, we present *DynaMammoAnalyst*, a novel decision support software that facilitates lesion identification, delineation and evaluation by providing improved visualization, segmentation and localization of suspiciously enhancing regions, interactive plots of time-intensity curves and time-intensity curve distributions. It minimizes the time required to explore breast MRI data and reduces inter and intra-observer variability by providing decision support for simultaneous quantitative dynamic and morphologic evaluations.

8.2 Overview of DynaMammoAnalyst

DynaMammoAnalyst, is a special 32-bit software, designed to run on personal computers with Microsoft Windows operating systems. It is written by the authors in Borland Delphi 7.0 (Borland Software Cooperation, Inc., USA) and has user-friendly graphical interfaces to explore breast MRI in the Digital Imaging and Communications in Medicine (DICOM) standard created by the National Electrical Manufacturers Association. There are four specially designed windows; “Main” window, “Slice Explorer” window, “Zoom” window and “Dynamic Analysis” window.

8.2.1 Loading of Patient Data

The user selects the patient study file, usually named as DICOMdir, to be processed via the “Main” window. This file acts as a directory for DICOM file sets and holds a full four level hierarchy (Patient, Study, Series and Image). It stores information about the breast MR examination such as the patient name, the study date, the imaging protocols used, the names of the acquired image files and their locations. Using these data, the software populates MR image filenames into slice locations under the imaging protocols and creates a study tree, as seen in Figure 8.1. To start diagnostic analysis, the user should select a slice.

8.2.2 Visualization of Suspicious Enhancements

If the selected slice belongs to a scan acquired without contrast agent such as a T2 weighted scans or a fat suppressed T_1-weighted scans, the software only displays the relevant image on the “Slice Explorer” window. At the top of this window, patient information and the imaging protocol used is displayed and a slice navigation bar is presented, as seen in Figure 8.2. However if a slice is selected from a dynamic scan then the software displays acquired pre and post-contrast images, subtraction images, maximum intensity image and uniquely color coded map of normalized maximum intensity time ratio (nMITR) on the “Slice Explorer” window (see Figure 8.3) as discussed below.

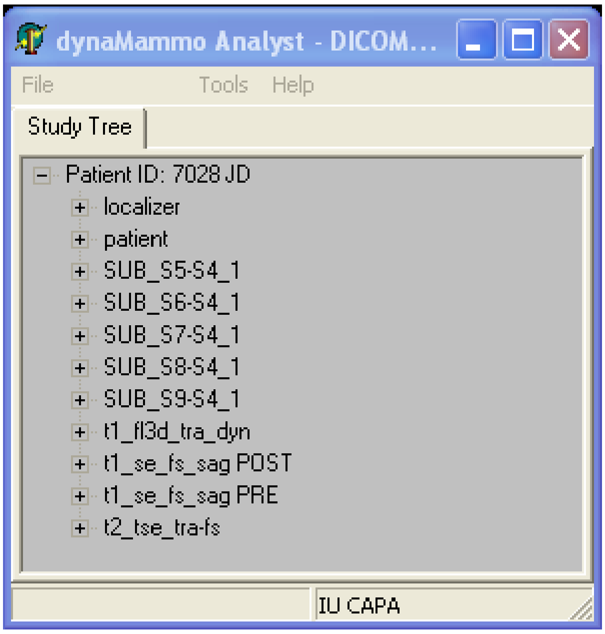

Patient ID: 7028 JD
- localizer
- patient
- SUB_S5-S4_1
- SUB_S6-S4_1
- SUB_S7-S4_1
- SUB_S8-S4_1
- SUB_S9-S4_1
- t1_fl3d_tra_dyn
- t1_se_fs_sag POST
- t1_se_fs_sag PRE
- t2_tse_tra-fs

Figure 8.1 Main window and study tree populated from the selected DICOMdir file.

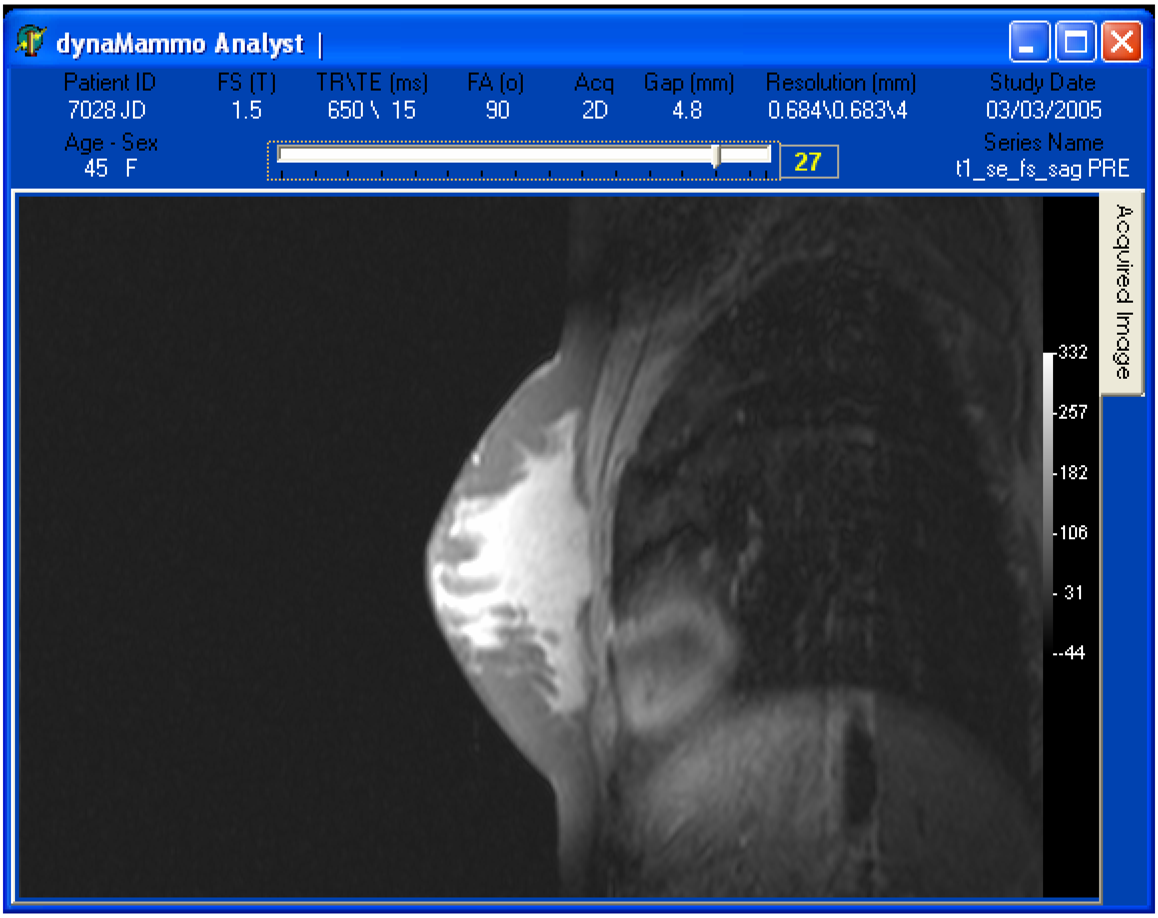

Patient ID	FS (T)	TR\TE (ms)	FA (o)	Acq	Gap (mm)	Resolution (mm)	Study Date
7028 JD	1.5	650 \ 15	90	2D	4.8	0.684\0.683\4	03/03/2005

Age - Sex: 45 F

Series Name: t1_se_fs_sag PRE

Figure 8.2 Slice Explorer window for a scan without contrast agent.

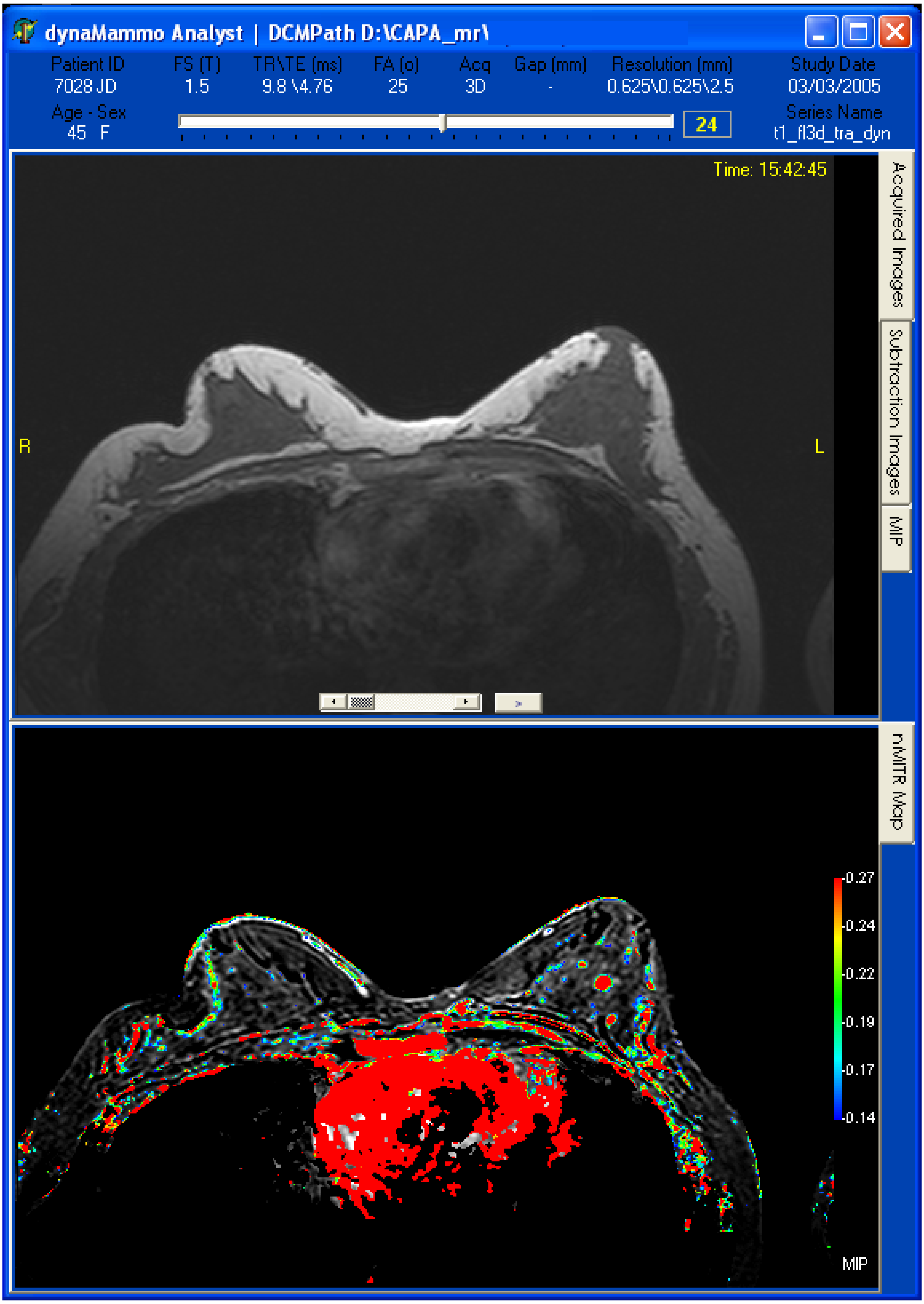

dynaMammo Analyst | DCMPath D:\CAPA_mr\

Patient ID	FS (T)	TR\TE (ms)	FA (o)	Acq	Gap (mm)	Resolution (mm)	Study Date
7028 JD	1.5	9.8 \4.76	25	3D	-	0.625\0.625\2.5	03/03/2005

Age - Sex		Series Name
45 F	24	t1_fl3d_tra_dyn

Time: 15:42:45

Figure 8.3 Slice Explorer window for a dynamic scan.

Subtraction images and MIP are generated by processing acquired pre and post-contrast images pixel-by-pixel for the slice. These images, except MIP, may also be displayed in the cine-mode. The relative enhancements and the nMITR map are calculated using the following equations [54], [34]:

$$E_{\Re}(i) = \frac{I_{\Re}(i) - I_{\Re}(0)}{I_{\Re}(0)} \times 100 \tag{8.1a}$$

$$nMITR_{\Re} = \frac{\max\{E_{\Re}\}}{T_{\max}} \tag{8.1b}$$

In the above equations, $\Re$ represents a small moving ROI, 3×3 pixels in size. It is initially placed to the upper leftmost portion of the slice stack, and moved to a new location until the whole stack is covered. $i = 1, 2, ...5$, is the acquisition order of the post-contrast images; $I_{\Re}(i)$ and $E_{\Re}(i)$ are the average intensity and the relative enhancement of the *i*–th post-contrast image within $\Re$. $I_{\Re}(0)$ is the average intensity of the pre-contrast image. $T_{\max}$ denotes the time (in seconds) at which the enhancement $E_{\Re}$ reaches to its maximum.

The nMITR maps are displayed in HSV color format; values smaller than a lower threshold value (default 0.14 sec^{-1}) are shown in blue while values bigger than an upper threshold value (default 0.27 sec^{-1}) are displayed in red. The default threshold values have been optimized to distinguish lesions from the surrounding vascular tissues such as moderately enhanced normal parenchyma, blood vessels and fat. Although they work well in most applications, the user can interactively adjust the upper threshold for improving contrast. The software makes possible to superimpose the MIP on the nMITR map.

8.2.3 Interactive Enhancement Analysis

When the “Slice Explorer” window is opened for a dynamic scan, the system automatically creates and displays all the relevant images and places a 3×3 pixel ROI at the current cursor location.

A magnified nMITR map of the region centered at the current cursor location, focused by a cross, is also displayed in the "Zoom" window. It is also possible to synchronize this view with the magnified MIP of the region centered at the same cursor location (see Figure 8.4a). The corresponding enhancement values, the time that enhancement reaches its maximum, nMITR value, *ISB* (initial signal behavior) and *PSB* (post-initial signal behavior) of the tissue at this location are computed (using Eqs. 8.1.a-d, [62]) and the TIC is plotted in the "Dynamic Analysis" window. (see Figure 8.4b). If the user changes the cursor to a new location, all these computations and visualization will be repeated. Thus, the user can interactively guide the system to facilitate lesion localization and malignancy detection.

$$ISB = \frac{I_{\Re \max 1-3\min} - I_{\Re}(0)}{I_{\Re}(0)} \times 100 \qquad (8.1.c)$$

$$PSB = \frac{I_{\Re 8\min} - I_{\Re \max 1-3\min}}{I_{\Re \max 1-3\min}} \times 100 \qquad (8.1.d)$$

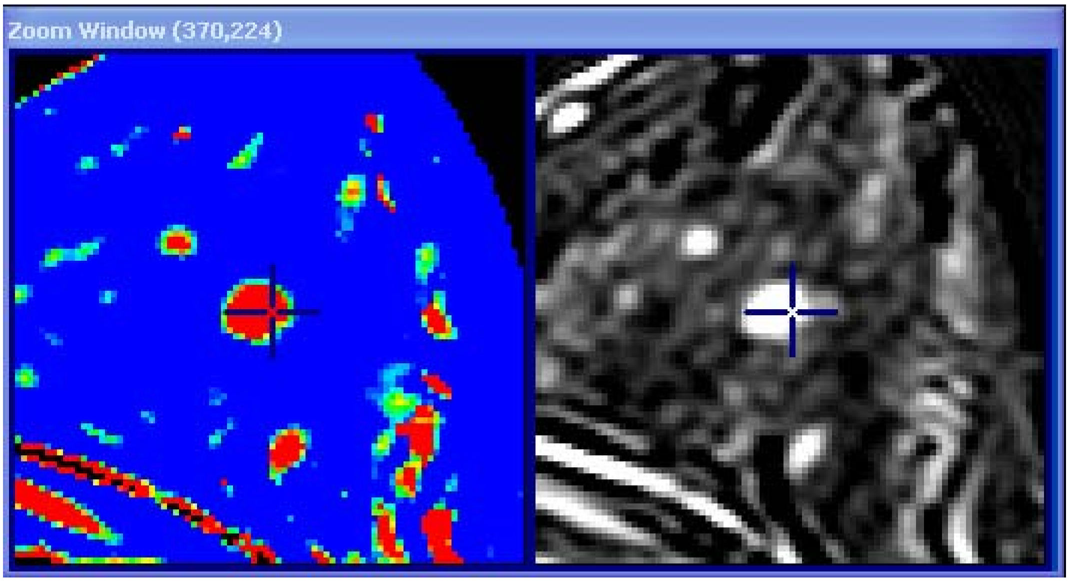

(a)

Figure 8.4 (a) The Zoom Window that displays magnified nMITR map and MII of the region centered at the current cursor location, (b) the Dynamic Analysis window that displays computed enhancement parameters of the tissue at the current cursor location.

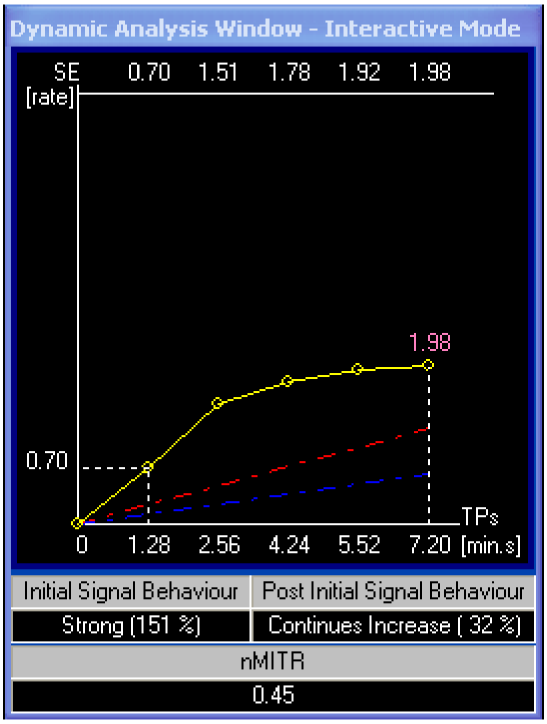

Initial Signal Behaviour	Post Initial Signal Behaviour
Strong (151 %)	Continues Increase (32 %)

nMITR
0.45

(b)

Figure 8.4 Continued.

8.2.4 Automated Lesion Segmentation and Diagnosis

Once a lesion is identified, the user may easily segment it by manually selecting a seed point inside on its nMITR map. Region growing is then automatically performed to generate irregular whole ROI. Several descriptive parameters are next computed and displayed in “Zoom” and “Dynamic Analysis” windows.

The superimposed nMITR map of the lesion and generated ROI (in navy) are presented in the “Zoom” window scaled by a zoom factor of three. The superimposed MIP of the lesion and generated ROI (in blue) is also presented in the same window (see Figure 8.5a). Center location of the lesion (shown in navy and blue in the magnified images), it’s area and bounding box area, valuable for MR-guided interventions, are displayed in this window above two diagnostic features, namely normalized complexity and maximum nMITR. The tissue with the maximum *nMITR* inside the ROI is interrogated pixel-by-pixel to determine the enhancement behavior of the lesion while *normalized complexity* of the

ROI (expressed as the square of the ROI perimeter divided by the 4π×ROI Area) is computed to quantify the shape of the lesion. Mean enhancement values, mean time-intensity curve, percentages of tissues within the ROI with continues increase (*PSB*> 10%), plateau (-10% < *PSB* < 10%) and wash-out (*PSB*< -10%) enhancement patterns, mean initial signal increase and post-initial signal behaviors, mean *nMITR* and mean T_{max} are displayed in the "Dynamic Analysis" window. A diagnostic decision supplied by a classifier embedded into the software is also displayed at the bottom of the "Zoom" window to help the user (see Figure 8.5b). The classifier is a maximum likelihood estimator designed using a training set. Gaussian density functions for two-class (benign or malignant) data are determined by

$$f_{x_1x_2}(x_1,x_2)=\frac{1}{2\pi\left|C_x\right|^{1/2}}\exp\left(-\frac{1}{2}(\mathrm{x}-\mu)'C_x^{-1}(\mathrm{x}-\mu)\right) \tag{8.2}$$

where x_1 and x_2 are the maximum *nMITR* and *normalized complexity* features computed from the slice in which the lesion has the largest diameter; μ and C_x are the mean-value vector and the covariance matrix, respectively.

8.2.5 Experimental Data

Breast imaging is performed on a 1.5 Tesla MR scanner (Magnetom Symphony, Siemens Medical Systems, Erlangen, Germany) equipped with a dedicated four-element phased-array receiver breast coil. Patients are positioned prone with the breast to be imaged in gentle compression within the coil to minimize motion artifacts. The imaging sequence is 3D fast low angle shot (FLASH) (TR/TE 9.80/4.76 msec, flip angle 25^o, matrix size 512×512, slice thickness 2.5 mm, $0.625\times0.625\text{mm}^2$ in-plane resolution). During and immediately after the bolus injection of contrast agent Gd-DTPA (0.1 mmol/kg body weight), one pre-contrast and five post-contrast high-resolution bilateral axial images are acquired per slice with a temporal resolution of approximately 88 seconds. 12-bit grayscale image sets are transferred from the MR scanner to a personnel computer in DICOM format for further analysis.

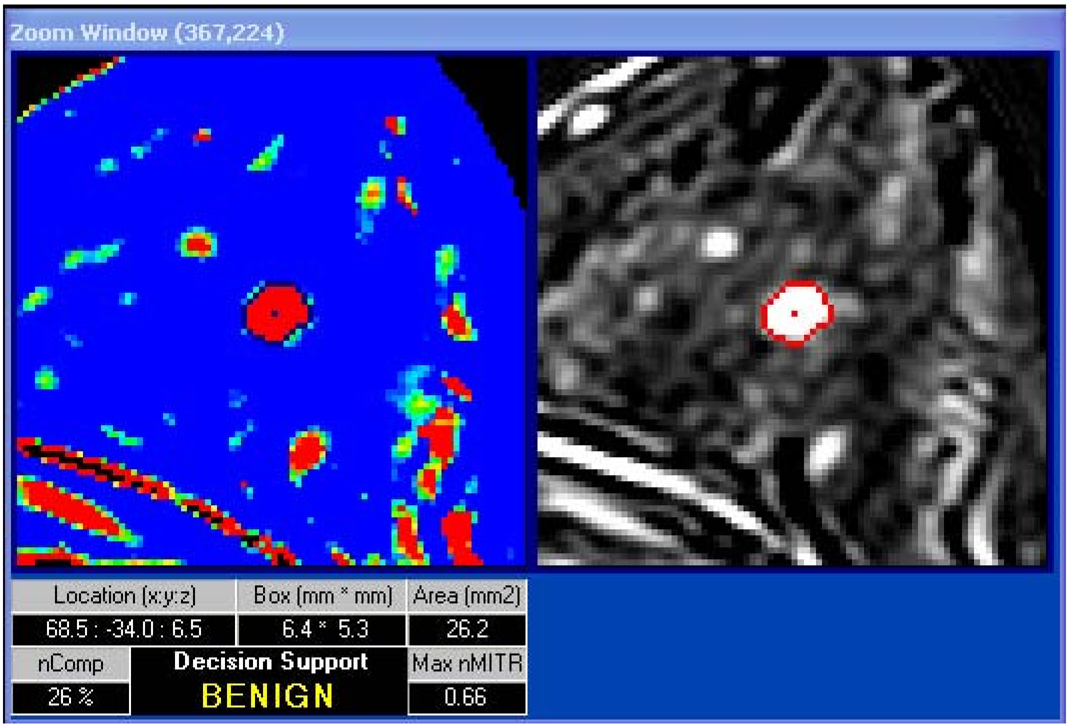

Location (x:y:z)	Box (mm * mm)	Area (mm2)
68.5 : -34.0 : 6.5	6.4 * 5.3	26.2

nComp	Decision Support	Max nMITR
26 %	BENIGN	0.66

(a)

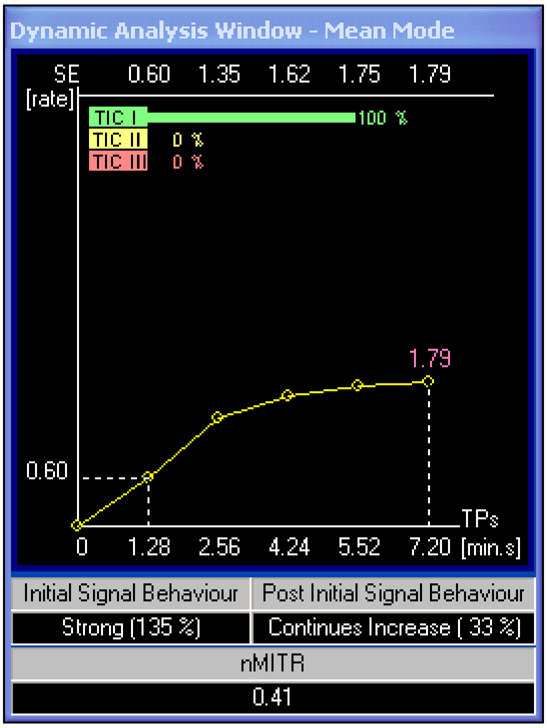

Initial Signal Behaviour	Post Initial Signal Behaviour
Strong (135 %)	Continues Increase (33 %)

nMITR
0.41

(b)

Figure 8.5 (a) The Zoom Window that presents the superimposed nMITR map of the lesion and generated ROI (in navy) and superimposed MIP of the lesion and generated ROI (in blue) scaled by a zoom factor of three and that displays supplied decision support, (b) Dynamic Analysis window that shows the result of enhancement computations.

The software has been tested on a dataset consisting of contrast enhanced MR mammograms from 40 women (age: 32-62 years; mean age: 49 years). The nature of the imaging procedure is explained to all the patients and their consents are secured. 20 benign and 24 malignant lesions have been manually marked on the nMITR maps by two expert radiologists after mutual agreement (approximate lesion center is marked; the whole lesion contour is not delineated). All the findings have been supported either by histopathological examination or by clinical follow-up.

8.2.6 Statistical Analysis

The significances of the features in discrimination of malignancy are evaluated using SPSS 15 (SPSS Inc., USA). The independent samples t-test with either a pooled or separate variance as determined by the Levene's test for equality of variances is performed. Accuracies of the features are calculated from the area under the ROC curve [117].

The classifier was trained with 10 benign and 12 malignant lesions and tested with the remaining 22 lesions. Diagnostic characteristics of the classifier were assessed by *Se* (sensitivity), *Sp* (specificity), *DA* (diagnostic accuracy), *PPV* and *NPV* (positive and negative predictive values) calculated using:

$$Se = \frac{TP}{TP + FN} \tag{8.3a}$$

$$Sp = \frac{TN}{TN + FP} \tag{8.3b}$$

$$DA = Se \times Pr + Sp \times (1 - Pr) \tag{8.3c}$$

$$PPV = \frac{Se \times Pr}{Se \times Pr + (1 - Se) \times (1 - Pr)} \tag{8.3d}$$

$$NPV = \frac{Sp \times (1 - Pr)}{Sp \times (1 - Pr) + (1 - Se) \times Pr} \tag{8.3e}$$

where *TP*, *FN*, *TN* and *FP* are true-positive, false-negative, true-negative and false-positive decisions of the classifier, respectively. *Pr* is the expected prevalence of malignancy in the study dataset.

8.3 Results

DynaMammoAnalyst permits an easy and fast way to explore and analyze breast MR data. Although subtraction images and MIPs are helpful to highlight suspicious enhancing regions, presence of image intensity non-uniformity on these images may lead to faulty detections. To minimize such problems and to improve contrast, the system makes use of color-coded nMITR maps from dynamic data. Interactive TIC plots make it easy to analyze suspicious enhancements and therefore facilitate lesion identification. When the user selects a seed point inside an identified lesion, whole lesion ROI is automatically generated and a number of diagnostic features, valuable for MR-guided interventions and diagnosis, are computed. Moreover, a maximum likelihood classifier is embedded within the software supplies decision support to the user based on computed normalized complexity and maximum nMITR.

Measurements from the nMITR maps in which the lesions have the largest diameter show that there are significant differences between the benign and malignant lesions for normalized complexity (0.27 ± 0.14 and 0.50 ± 0.21, $P = 0.002$, *accuracy*= 0.77) and maximum nMITR (1.27 ± 0.70 and 3.22 ± 1.42, $P < 0.001$, *accuracy*= 0.92). Our results from maximum nMITR and normalized complexity verify the recent studies mentioned previously. Moreover, due to the special technique used, higher significance values are achieved. The classifier was trained with 10 benign and 12 malignant lesions and tested with the remaining 22 lesions. For the test dataset, the classifier achieved 92% sensitivity, 90% specificity, 91% diagnostic accuracy, 92% positive predictive value and 90% negative predictive value.

The usefulness of the developed software is illustrated using three cases. First, a 52 years old woman is considered. Using the slice navigator in the “Slice Explorer” window, visual examination of the images shows that there is a lesion on her right breast. Figures

8.6a and 8.6b shows the generated MIP and nMITR image for the selected slice (slice 14). It is the "representative" slice in which lesion has its largest diameter. Whole lesion ROI automatically generated after supplying a seed point inside the lesion by the user. From this ROI, several descriptive parameters are computed and displayed in the "Zoom" window (Figure 8.6c) and in the "Dynamic Analysis" window (Figure 8.6d). The mean enhancement curve and the percentages of voxels within the ROI with persistent, plateau and wash-out enhancement patterns are plotted in the latter window. The lesion has an ovoid shape and show homogeneous enhancement. Its mean TIC curve shows plateau and the mean nMITR is low. However, the lesion has a high maximum nMITR value of 3.82 and TIC distributions emphasize that 37% of the tissues inside it show wash-out. The decision support given is as malignant and is correct since histopathological examination confirmed that the lesion is an invasive lobular carcinoma.

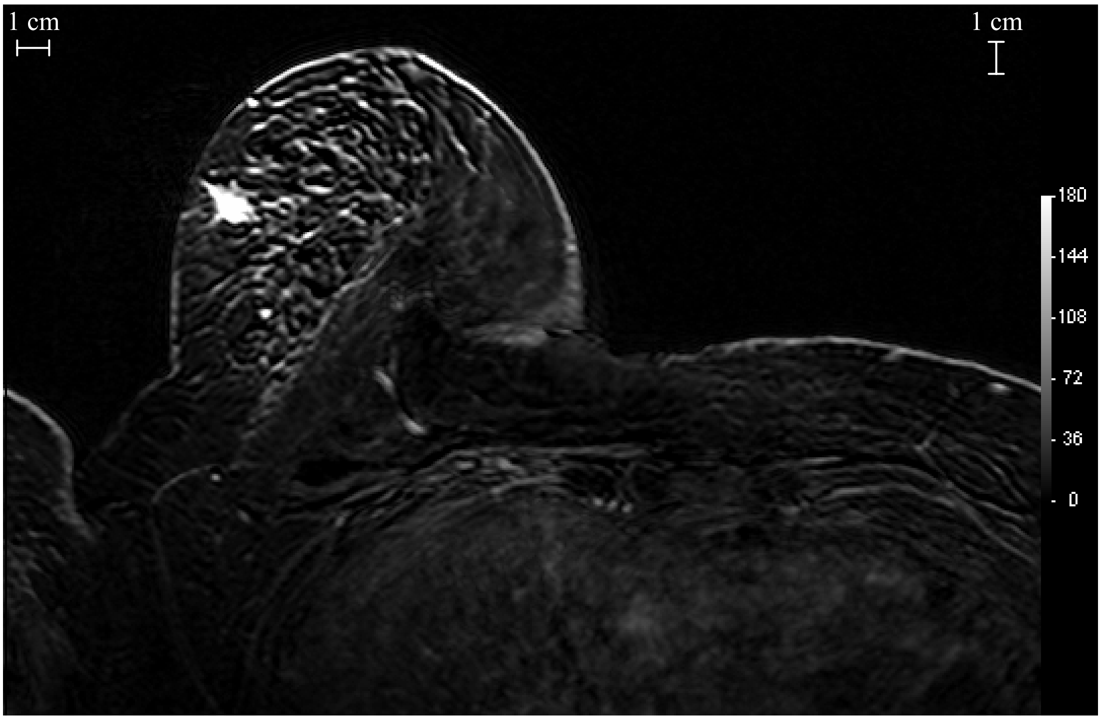

(a)

Figure 8.6 (a) MIP and (b) nMITR image for the representative slice (slice 14) of a lesion of a 52 years old woman on her right breast. (Histopathology: Invasive lobular carcinoma).

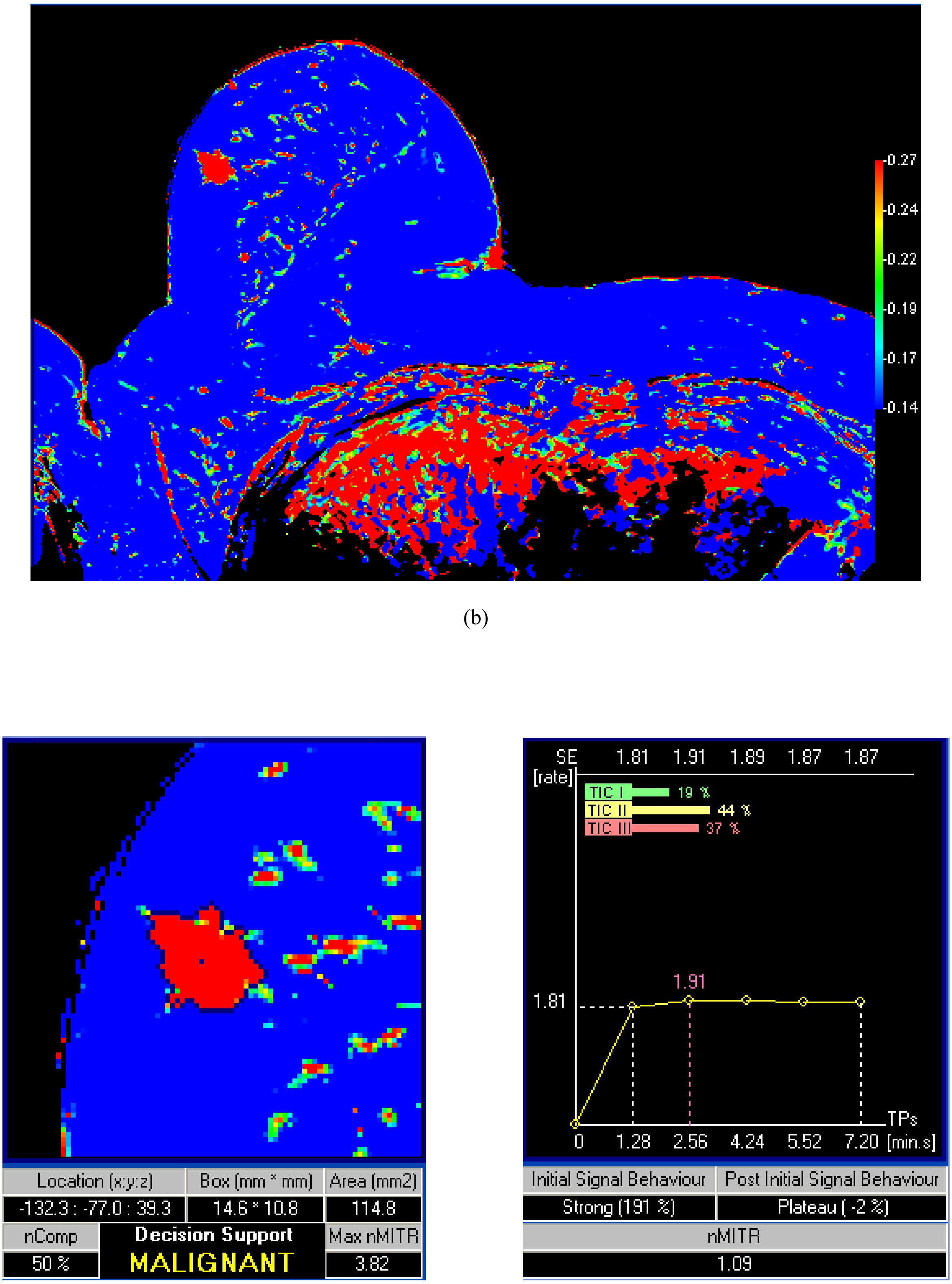

(b)

Location (x:y:z)	Box (mm * mm)	Area (mm2)
-132.3 : -77.0 : 39.3	14.6 * 10.8	114.8
nComp	Decision Support	Max nMITR
50 %	MALIGNANT	3.82

(c)

Initial Signal Behaviour	Post Initial Signal Behaviour
Strong (191 %)	Plateau (-2 %)

nMITR

1.09

(d)

Figure 8.6 Continued.

Figures 8.7a and 8.7b shows the generated MIP and nMITR image for the representative slice (slice 20) of a lesion of a 48 years old woman on her left breast near to the chest-wall. Descriptive parameters computed from the generated whole lesion ROI and displayed in the "Zoom" window and in the "Dynamic Analysis" window are presented in Figures 8.7c and 8.7d. The lesion has an ovoid shape and show homogeneous enhancement. Its mean TIC curve shows continues increase and the mean nMITR is low. The lesion has a low maximum nMITR value of 1.36, however TIC distributions emphasize that 42% of the tissues inside it show plateau or wash-out. The decision support given as benign; and it is correct since histopathological examination verifies that the lesion is a fibroadenoma.

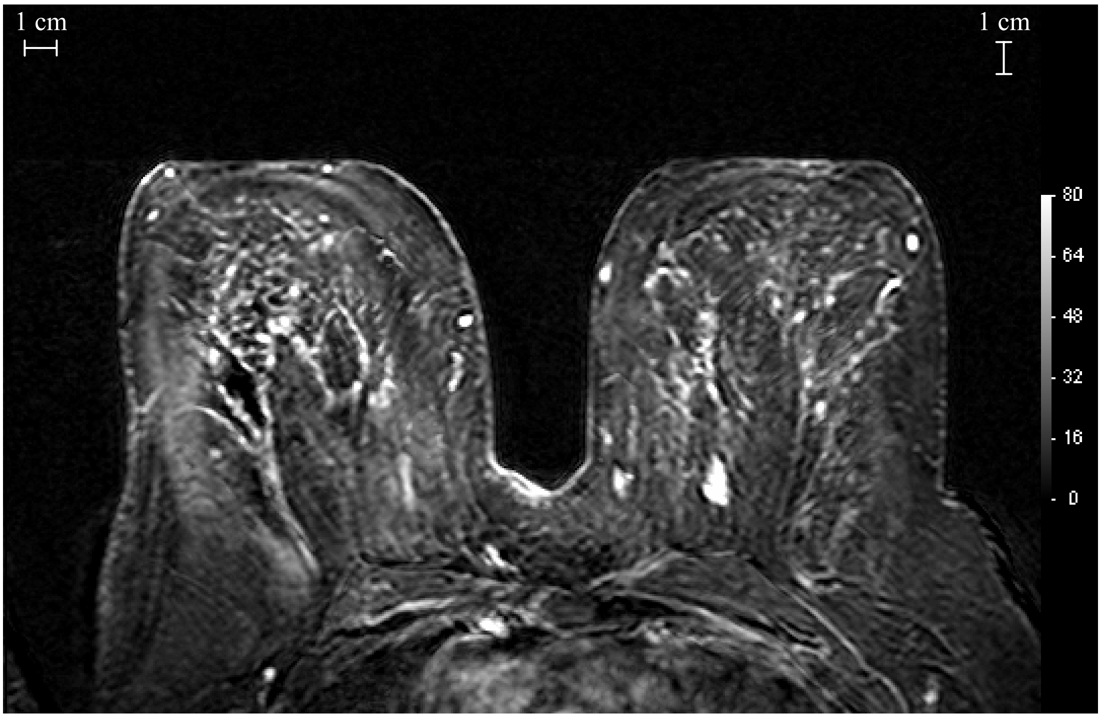

(a)

Figure 8.7 (a) MIP and (b) nMITR image for the representative slice (slice 20) of a lesion of a 48 years old woman on her left breast near to the chest-wall. (Histopathology: Fibroadenoma).

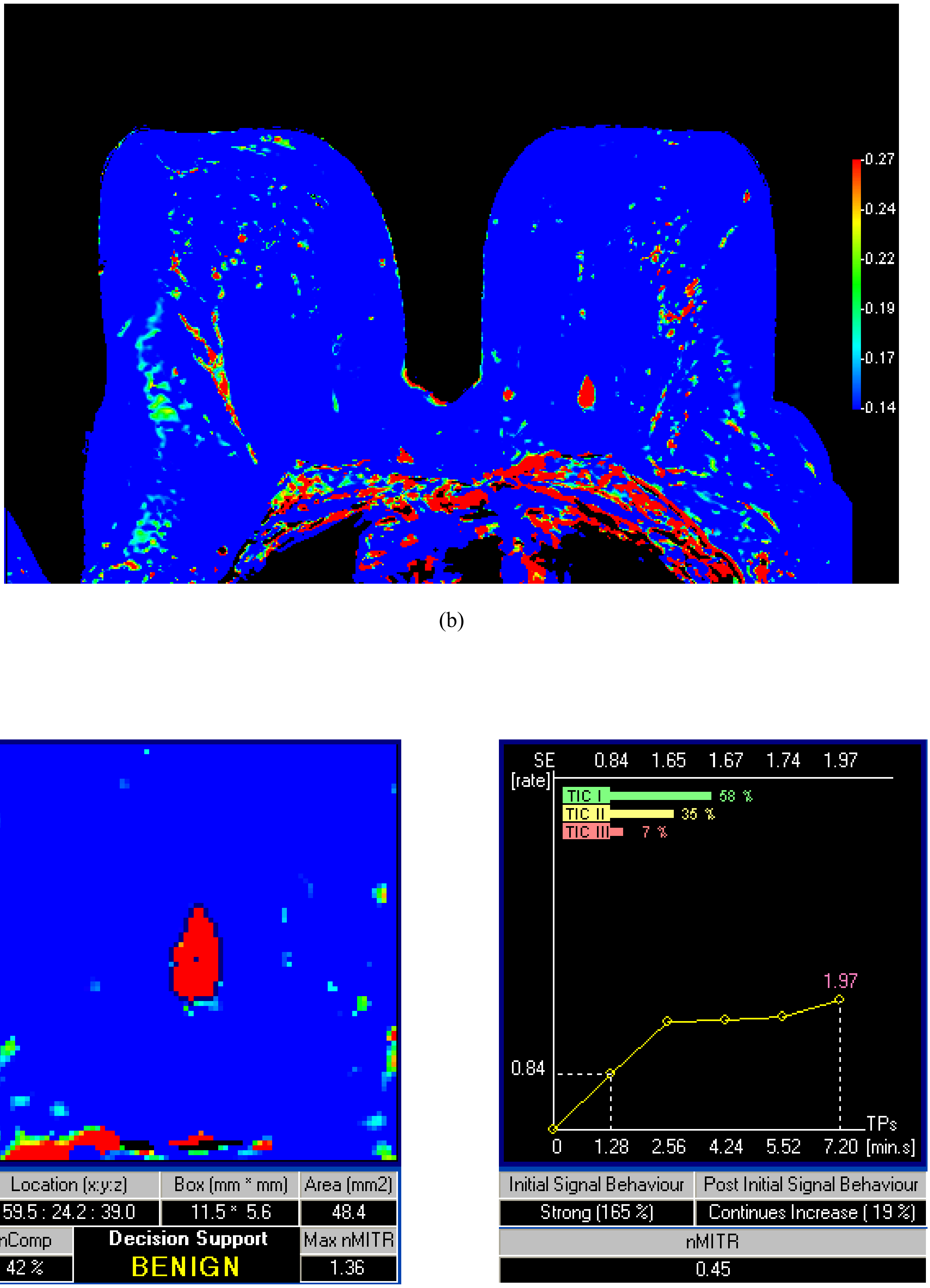

(b)

Location (x:y:z)	Box (mm * mm)	Area (mm2)
59.5 : 24.2 : 39.0	11.5 * 5.6	48.4
nComp	**Decision Support**	Max nMITR
42 %	BENIGN	1.36

Initial Signal Behaviour	Post Initial Signal Behaviour
Strong (165 %)	Continues Increase (19 %)

nMITR
0.45

(c) (d)

Figure 8.7 Contiued

Figures 8.8a and 8.8b shows the generated MIP and nMITR image for the representative slice (slice 22) of a lesion of a 42 years old woman. Descriptive parameters computed from the generated whole lesion ROI and displayed in the “Zoom” window and in the “Dynamic Analysis” window are presented in Figures 8.8c and 8.8d. The lesion has spiculated margins and inhomogeneous enhancement. It is difficult to make a diagnosis only using the mean enhancement computation values. Mean TIC curve shows plateau (not a wash-out) and the mean nMITR is low. However, the lesion has a high maximum nMITR value of 4.37 and TIC distributions prove that 61% of the tissues inside it show wash-out. The decision support is given as malignant; and it is correct since histopathological examination verifies that the lesion is an invasive ductal carcinoma.

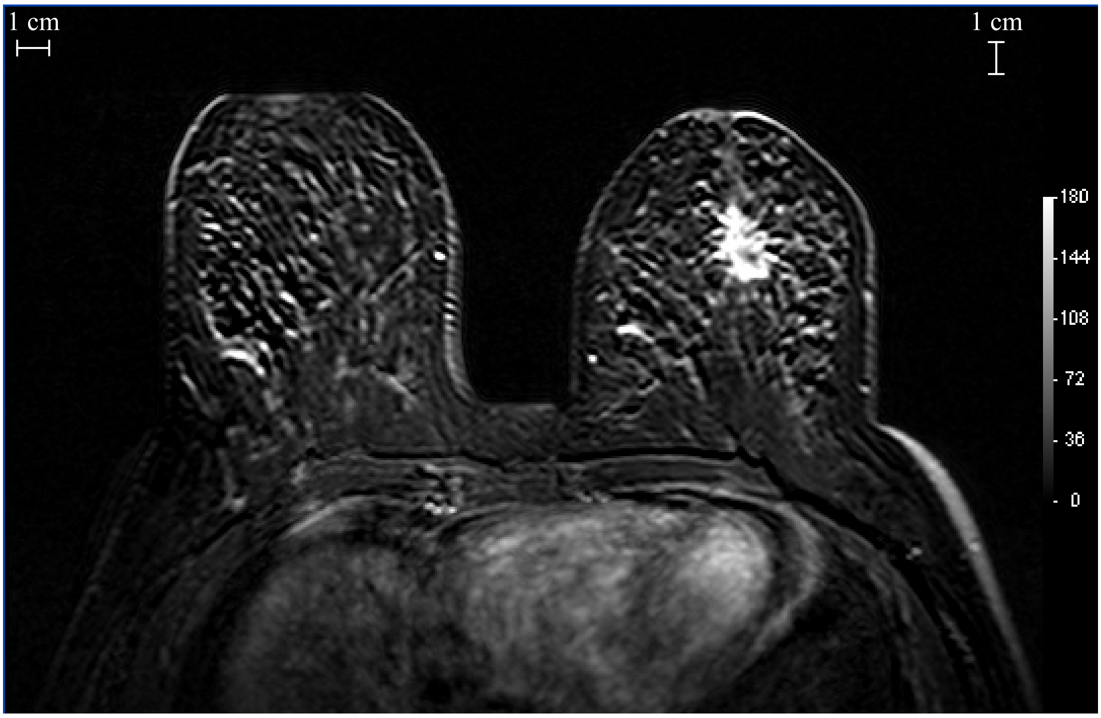

(a)

Figure 8.8 (a) MIP and (b) nMITR image for the representative slice (slice 22) of a lesion of a 42 years old woman (Histopathology: Invasive ductal carcinoma).

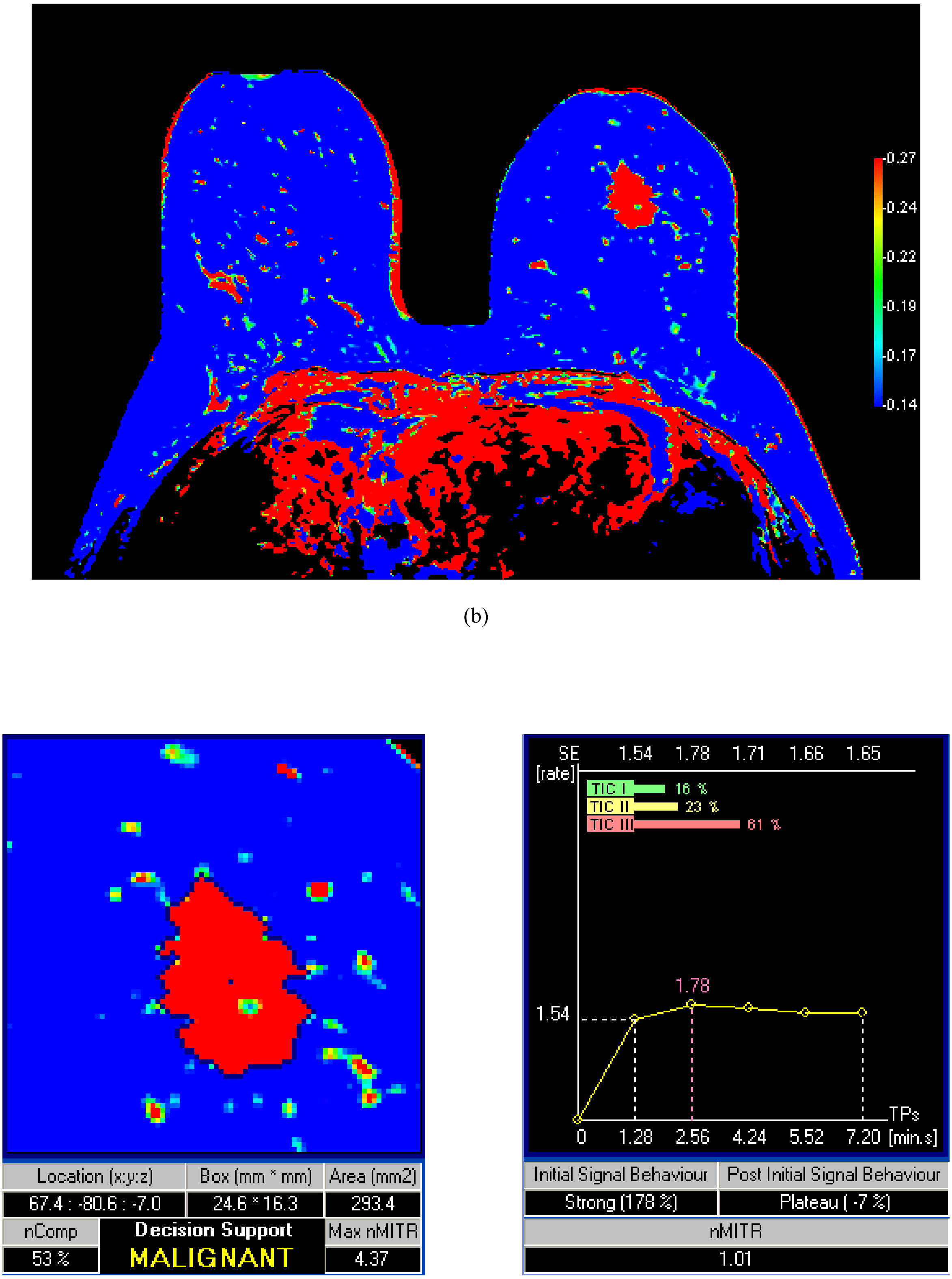

Location (x:y:z)	Box (mm * mm)	Area (mm2)
67.4 : -80.6 : -7.0	24.6 * 16.3	293.4
nComp	**Decision Support**	Max nMITR
53 %	**MALIGNANT**	4.37

Initial Signal Behaviour	Post Initial Signal Behaviour
Strong (178 %)	Plateau (-7 %)

nMITR
1.01

(b)

(c)

(d)

Figure 8.8 Continued.

8.4 Conclusion

MR mammography (MRM) is gaining increased acceptance for detecting breast cancer in its early stages since it offers the highest sensitivity among other breast imaging modalities. In MRM, lesion-obscuring overlapping structures and summation shadows are much less pronounced as there is no need for excessive breast compression during imaging. Moreover, it does not use harmful ionizing radiation and with the help of contrast agents, it provides important tissue information on cross-sectional morphology, as well as functional information on perfusion and capillary leakage.

For accurate assessment of breast cancer however, a large volume of image data must be acquired at high spatial and temporal resolutions with an MR scanner and must be analyzed meticulously. The morphology and enhancement dynamics of every suspicious region must be visually evaluated diligently by placing a small region of interest (ROI) over the early enhancing component of the lesion and tracking its course over time. As these regions can be very small and there may be several deceptively enhanced regions from healthy tissues, manual identification of lesions from acquired images and subtraction images requires intensive attention of an expert radiologist for periods that may exceed 30 minutes. Moreover, the final diagnoses reflect the experience of the examiners and are thus subjective.

DynaMammoAnalyst is a novel decision support software developed by the authors to speed up the examinations and overcome subjectiveness via computation of several enhancement parameters. It facilitates lesion identification, delineation and evaluation by providing improved visualization, segmentation and localization of suspiciously enhancing regions, interactive plots of time-intensity curves and time-intensity curve distributions. It shortens the time required to explore breast MRI data considerably and reduces inter and intra-observer variability by providing decision support for simultaneous quantitative dynamic and morphologic evaluations. DynaMammoAnalyst is able to process breast MR images acquired in different orientations with different resolutions and is able to show images in DICOM format from other modalities such as X-ray mammography and breast ultrasound, supplying adjunct diagnostic information to the radiologist. It requires minimal user interaction and post processing of the images is pleasingly fast.

Improved diagnostic performance in discrimination of malignancy is achieved using morphological and enhancement descriptors extracted from nMITR maps. These maps, generated from dynamic MRM datasets, do not require prior fat suppression or superb homogeneity (as do subtraction images and maximum intensity projections) and moreover, can improve contrast by suppressing enhancements of blood vessels and normal parenchyma that surround the lesions and therefore are especially advantageous during evaluation premenopausal women.

To be self-sufficient, the present software must be empowered with additional functionalities, such as volumetric visualization, diagnostic feature extraction and automated lesion localization. To improve classification accuracy further, the fast localization technique that the authors have recently developed to segment breasts, detect suspiciously enhancing regions and eliminate false-positive detections [124] can be implemented and the maximum likelihood classifier can be replaced with a better classifier. Another potential area that is worthy of exploration is the diagnostic significance of 3D features such as nMITR-entropy and 3D visualizations [116]. Although DynaMammoAnalyst is inherently capable of compensating small motion artifacts due to the averaging nature of the nMITR maps, it does not include a dedicated motion correction scheme. Patient motion may lead to serious diagnostic complications as a result of misalignments of the image sequences during acquisition of dynamic images. Some of the image registration techniques that have been proposed in the literature on motion correction can be used to deal with this difficult problem [102, 103, 104, 105]. We intend to tackle this problem also in the future.

9. CONCLUSIONS

9.1 General

Dynamic Contrast Enhanced Magnetic Resonance Mammography (DCE-MRM) is gaining increased acceptance for detecting breast cancer in its early stages since it offers the highest sensitivity among other breast imaging modalities. In DCE-MRM, lesion-obscuring overlapping structures and summation shadows are much less pronounced as there is no need for excessive breast compression during imaging. Moreover, it does not use harmful ionizing radiation and with the help of contrast agents, it provides important tissue information on cross-sectional morphology, as well as functional information on perfusion and capillary leakage.

For accurate assessment of breast cancer however, a large volume of image data must be acquired at high spatial and temporal resolutions with an MR scanner and must be analyzed meticulously. The morphology and enhancement dynamics of every suspicious region must be visually evaluated diligently by placing a small region of interest (ROI) over the early enhancing component of the lesion and tracking its course over time. As these regions can be very small and there may be several deceptively enhanced regions from healthy tissues, manual identification of lesions from acquired images and subtraction images requires intensive attention of an expert radiologist for periods that may exceed 30 minutes. Moreover, the final diagnoses reflect the experience of the examiners and are subjective. The basic goal in this thesis was, therefore, to develop the foundations for a decision support system that can assist radiologists and relieve their heavy burden of meticulous visual examinations of a large number of images by automatically performing computerized lesion localization and in assisting them in their final malignancy detections.

9.2 Lesion Localization

Lesion localization is a complex and computationally expensive process in which regions that are out of interest and deceptive enhancements must be carefully segmented out to prevent false-positive detections in the vicinity of these regions. In this thesis, a fully automated 3D lesion localization system is developed that does not need user supervision. The system makes use of massively parallel cellular structures with learning capabilities called cellular neural networks (CNNs) that offer alternative solutions to complex image processing applications with their extremely high throughputs. To prevent false-positive detections in the vicinity of regions out of interest such as thoracic cavity, lungs and heart, breast region of interest is first segmented from the pre-contrast images using two cascaded 2D CNNs, specifically designed for this purpose. The first net performs gray level thresholding and the second net is used to erase small objects and to smooth-out sharp corners. For the segmented breast, to be able to identify suspicious enhancements and to remove low deceptively enhanced tissues such as blood vessels, fatty tissue, muscles and normal parenchyma, a 3D nMITR map is generated using a moving ROI of 3×3 voxels and converted into binary form via a carefully selected threshold. The resultant map is next processed with a 3D template of three layers of 12×12 cells using a convolution-like operation that is quite similar to what radiologists do for lesion detection; they mentally use templates based on their experience and evaluations of lesion anatomies. Using the designed template it is possible to detect small lesions. At the end of the template processing, volumes geometrically similar to the template become enhanced. To boost lesions and to eliminate moderately enhanced normal tissues, the convolution result is passed from a threshold that yields a similarity of 47%. A lower value will result in increased false-positive detections due to enhanced blood vessels, while higher values will result in missed lesions. This method was tested with a dataset of 2064 MR mammograms containing 39 marked lesions. Ninety-seven percent of the breasts were segmented properly and all the lesions were detected correctly (detection sensitivity=100%), however, there were some false-positive detections (0.31/lesion, 0.10/slice).

To our knowledge, there are no publications on computerized methods that focus solely on DCE-MRM lesion detection. Bian et al. [13] seem to be working on this topic and in a recent abstract reported their initial results[4]. When tested on dataset consisting of 20 cases with 21 lesions, their method correctly detected 16 of the lesions and on average, there were 9 false positive detections per case. These findings correspond to a detection sensitivity of 76% and a false-positive detection rate per lesion of 857%. In comparison, the performances of our system are better.

Proper segmentation of the breast is vital for the success of the system. There are cases in which segmentation may not be very accurate, especially for fat patients. Since intensities are reduced further away from the breast coil, segmentation may end inappropriately within the axilla at an arbitrary edge, leading to false negative detections. When there is a suspected lesion within the axilla, due to its better coverage, sagittal imaging should be used to minimize problems. During 3D template matching there may be some loss of morphological information. This loss of is tolerable in the current system since it is intended only for localizing lesions. This localization information can later be used as a guide for more accurate lesion segmentation that preserves morphology for malignancy discrimination. Patient motion can lead to serious diagnostic complications as a result of misalignments of the image sequences during acquisition of contrast-enhanced MR mammograms. Several image registration techniques have been proposed that attempt to solve this difficult problem. Although the present system does not include a dedicated motion correction scheme, it is inherently capable of compensating small motion artifacts due to the averaging nature of the nMITR maps.

To improve the work on lesion localization mentioned above, we have experimented with a number of different CNN architectures on an expanded dataset. In one study, to segment the breast region of interest, instead of the two CNN architecture, we tried using four coupled 2D CNNs connected in cascade. The similarity threshold and the 3D template were replaced by a 3D CNN with a fuzzy c-partitioning output function. To minimize false positive detections, a set of decision rules extracted from volume and 3D eccentricity features of the suspicious regions were used to make localize lesions. This method was tested with a dataset that included 7020 MR mammograms with 76 marked mass lesions.

---

[4] We contacted the authors for more information and received the following message in response: "The study you mentioned was presented at the AAPM conference this year and we only have an abstract published so far for that topic".

3600 mammograms with 46 lesions of this set were used for training the system, the remaining data was used for test purposes. The segmentation algorithm performed well with high average precision, high true positive volume fraction and low false positive volume fraction with an overall performance of 0.93±0.05, 0.96±0.04 and 0.03±0.05, respectively (training: 0.93±0.04, 0.94±0.04 and 0.02±0.03; test: 0.93±0.05, 0.97±0.03 and 0.05±0.06). For the training dataset, the maximum lesion detection sensitivity was 100% with false-positive detections of 0.28/lesion, 0.09/slice and 0.65/case; however for the test dataset, the maximum detection sensitivity was 97% with false-positive detections of 0.43/lesion, 0.11/slice and 0.68/case, overall.

The use of CNNs, fuzzy c-partitioning, volume and 3D eccentricity criteria reduces false-positive detections due to artifacts caused by deceptively enhanced blood vessels, nipples and normal parenchyma and artifacts from vascularized tissues in the chest-wall due to over segmentation. We hope that this system will facilitate breast MR examinations, improve localization of lesions, provide important information before surgery, help reduce mortality due to undetected cancer re-occurrence as a result of missed multicentricity and decrease the number of unnecessary biopsies and mastectomies.

A software implementation of the proposed method, using a PC equipped with 2.4GHz processor, 3GB RAM, and Matlab 7.0, requires less than 18 minutes to process a single patient data. Although, this time can be reduced to sub-minute levels, using optimizing compilers, a direct hardware implementation will allow almost “real-time” processing speeds and will certainly open up new clinical applications. For example, quasi-automated MR-guided biopsies may be feasible and additional post-contrast lesion images can be acquired to improve morphological characterizations.

9.3 Malignancy Detection

We studied the effectiveness of a number of morphological and enhancement descriptors of breast lesions derived from nMITR projections for detection of malignancy. To do this, we first developed a method to segment and analyze lesions in three dimensions. The method consisted of four consecutive stages: volume of interest selection, nMITR projection generation using a moving 3×3 mask, three-dimensional lesion segmentation and feature extraction. Diagnostic relevance of enhancement features extracted from the generated nMITR projection was studied in detail. The maximum, the mean, the standard deviation and the entropy of the nMITR were found to be highly significant; the skewness and the kurtosis were found to be insignificant. The nMITR-entropy had the highest significance and the significances of the standard deviation and the maximum were similar. In general, the significance of the parameters studied in this work are found to be greater than those reported in the literature due to the 3D nature of our method, the use of the voxel sampling via moving masks and the use of high resolution images.

Morphological characteristics of lesions contain important diagnostic information for malignancy detection; therefore, a number of morphological descriptors extracted from the generated nMITR projection were studied in detail. 2D convexity, normalized complexity, extent and eccentricity as well as 3D versions of these descriptors and contact surface area ratio (CSAR) were considered. In a majority of previous morphological studies, 2D convexity and complexity measured from a “representative” slice in which the lesion has the largest diameter showed high significances. Our results from convexity, normalized complexity, extent and eccentricity measurements in 2D verify these findings. Moreover, due to the special technique used we achieve higher significance figures. Morphological descriptors introduced in this study, namely, 3D convexity, complexity and extent were found to have higher diagnostic accuracies (ranging between 0.70-0.81) and improved performance when compared with the recent studies that analyze volumetrically segmented lesions. CSAR was found to be the most significant and accurate descriptor (75% sensitivity, 88% specificity, 89% positive predictive value and 74% negative predictive value).

The methods developed in this thesis were used to develop a decision support software to speed up DCE-MRM examinations. This software, called *DynaMammoAnalyst*, requires minimal user guidance, facilitates lesion identification, delineation and evaluation by providing improved visualization, segmentation and localization of suspiciously enhancing regions, interactive plots of time-intensity curves and time-intensity curve distributions and computation of several enhancement parameters.

It can also handle breast MR images acquired in different orientations with different resolutions.

In conclusion, our findings demonstrate that the nMITR maps generated from dynamic MRM datasets are very effective for lesion localization and malignancy detection. They inherently suppress enhancements due to normal parenchyma and blood vessels that surround lesions and have natural tolerance to small field homogeneities. In comparison with subtraction images and maximum intensity projections they can be used in breast evaluations without prior fat suppression. Morphological and enhancement descriptors extracted from nMITR maps, in particular 3D morphological descriptors have significant diagnostic information and can be used for improving performance in discrimination of malignancy. Among these, the contact surface area ratio and the nMITR-entropy, have the higher significances and the higher diagnostic accuracies; they can be computed easily and are easily adaptable to different imaging protocols. The volumetrical segmentation technique for breast lesions based on voxel sampling with a moving mask is very effective and instrumental in improving diagnostic accuracies,

Due to the quantitative and the standardized nature of the techniques introduced in this work and because they are robust, efficient and reliable, we expect that their use in clinical practice, for surgical planning, for decision making, and in predicting the extent of residual disease after neoadjuvant chemotherapy will facilitate breast MR examinations, improve lesion localizations, increase diagnostic reproducibilities, decrease inter- and intra-observer variabilities, improve overall diagnostic performances especially for clinically and mammographically occult lesions, decrease the number of unnecessary biopsies and mastectomies, facilitate detection of multifocality and multicentricity and provide important information before surgery. Since presence of multicentricity is highly correlated with cancer re-occurrence, their use will also result in reductions in mortality due to undetected cancer re-occurrence.

9.4 Contributions

This PhD thesis is a preliminary search into computerized detection of lesions using nMITR maps of DCE-MR mammograms. A major contribution is the lesion localization techniques described in Chapters 4-5 that are based on nMITR maps and CNNs. The effectiveness and the efficiency of these techniques have been verified using a large dataset. The results are very promising and yield high detection sensitivities and result in very low false-positive detections. They can be used to detect multifocality and multicentricity. This is an important issue since presence of multicentricity is highly correlated with cancer re-occurrence.

Another major contribution of this thesis is the malignancy detection techniques described in Chapters 6-7. These techniques are based on morphological and enhancement features computed from volumetrically segmented lesions and can be used to standardize lesion evaluations with minimal user involvement. Being robust, efficient and reliable, they can be used for decision making, for surgical planning and for predicting the extent of residual disease after a neoadjuvant chemotherapy and to and minimize inter- and intra- observer variabilities, to increase diagnostic reproducibility and improve overall diagnostic performance especially for clinically and mammographically occult lesions.

The major efforts of this thesis is the development of a novel decision support software called as DynaMammoAnalyst to speed up the DCE-MRM examinations and overcome subjectiveness via computation of several enhancement parameters. This software is written to facilitate lesion identification, delineation and evaluation by providing improved visualization, segmentation and localization of suspiciously enhancing regions, interactive plots of time-intensity curves and time-intensity curve distributions. It shortens the time required to explore breast MRI data considerably and reduces inter and intra-observer variability by providing decision support for simultaneous quantitative dynamic and morphologic evaluations. It is also able to process breast MR images acquired in different orientations with different resolutions and is able to show images in DICOM format from other modalities such as X-ray mammography and breast ultrasound, supplying adjunct diagnostic information to the radiologist. It requires minimal user interaction and post processing of the images is pleasingly fast. Its use in clinical practice and for surgical planning may result in a decrease in the number of unnecessary mastectomies and a reduction in mortality.

9.5 Recommendations for Future Work

The methods developed in this thesis for lesion localization and malignancy detection are robust, efficient and reliable in terms of observer variability, allows better standardization of the evaluations, and appears promising. However, generalization of the results requires further testing on large number of cases, lesion sizes and subgroups, reproducibility, applicability to other populations and other MRI systems. A multi-center study should be conducted to expand the dataset and design a classification scheme that also considers lesion morphology hoping to further improve the performance of diagnosis by detecting rapidly enhancing fibroadenomas. The following is a list of additional topics waiting further exploration and improvements:

1. Classical optimization techniques or genetic algorithms may be used to compute optimal patient-specific template parameters and thresholds.
2. 3D CNNs can be used for lesion detection to minimize false-positive findings due to deceptive enhancements.
3. Segmentation problems may be further improved through 3D morphological and enhancement analysis.
4. Morphological descriptors of small lesions or large but lobulated lesions alone may not be sufficient to successfully discriminate malignancy. For such cases, new discrimination techniques may be developed using a combination of dynamic and morphological features such as mean margin sharpness and nMITR entropy of a detected lesion volume.
5. During 3D template matching there may be some loss of morphological information. This loss is tolerable if the objective is just localization of lesions. The localization information can later be used as a guide for more accurate lesion segmentation that preserves morphology for malignancy discrimination.
6. The segmentation technique discussed in Section 4.4 can be extended, by a simple modification of the CNN_O so that images acquired in other views can also be handled.

7. The CNNs can be implemented in hardware to cut down the processing time. The images can then be processed in (almost) real-time. This will certainly open up new clinical applications; for example, semi-automated MR-guided biopsies may be feasible and additional post-contrast lesion images can be acquired to improve morphological characterizations.

There are also a number of improvements that can be incorporated to *DynaMammoAnalyst*; it can be empowered with additional functionalities, such as volumetric visualization, diagnostic feature extraction and automated lesion localization. The fast localization technique described in Chapter 6 can be implemented to segment breasts, detect suspiciously enhancing regions and eliminate false-positive detections and the maximum likelihood classifier can be replaced with a better classifier to improve classification accuracy. Another potential area that is worthy of exploration is the diagnostic significance of 3D features such as nMITR-entropy and 3D visualizations. Although DynaMammoAnalyst is inherently capable of compensating small motion artifacts due to the averaging nature of the nMITR maps, it does not include a dedicated motion correction scheme. Patient motion may lead to serious diagnostic complications as a result of misalignments of the image sequences during acquisition of dynamic images. Motion correction schemes can be used to minimize the adverse effect of patient motion.

APPENDIX A. MATLAB FILES

During this Ph.D. study, several procedures have been written in Matlab 7.0 (The MathWorks, Inc., USA) to analyze dynamic 12-bit grayscale image sets transferred from the MR scanner in DICOM format and to numerically implement the developed methods. The m files that perform specific functions are given in the attached compact disk and are explained below.

SegmentCNN.m

This m file segments a breast MR image in DICOM format using two cascade connected cellular neural networks and saves the resultant image in BMP format. The details are given in Chapter 4.

SegmentCNN2.m

This m file segments a breast MR image in DICOM format using four cascade connected cellular neural networks and saves the resultant image in BMP format. The details are given in Chapter 5.

GeneratenMITRmapALL.m

This m file generates 3D nMITR map of the whole imaged volume. To do this, it reads the pre-contrast and post-contrast image files listed in a text file and calculates the relative enhancements and nMITR of the tissues using a 3×3 moving window by calling "computenMITR.m" file. The resultant map is saved into a mat file with an "nMITR" extension.

ComputenMITR.m

This m file computes the nMITR for a given intensity and enhancement course data.

Localize3DTemp.m

This m file reads the file with the nMITR extenstion (created by GeneratenMITRmapALL.m) and the BMP files for all slices generated by SegmentCNN.m. It extracts the 3D nMITR map of the breast and performs 3D template matching to localize lesions in the breast. It outputs a list that includes the detailed information on the detected lesions such as their volumes, starting and ending slices, etc.

Localize3DCNN.m

This m file reads the file with nMITR extenstion and the BMP files for all slices generated by SegmentCNN2.m. It extracts the 3D nMITR map of the breast and performs fuzyy 3D CNN processing to localize lesions reside in the breast. It outputs a list that includes detailed information on the detected objects such as their volumes, 3D eccentricity, starting and ending slices, etc. The detected lesions are marked with “+++” while the deleted volumes are marked with “---”, after applying a false-positive elimination criteria.

SegSuccess.m

This m file performs grey-level conversion (threshold= 255) and hole filling on both images to obtain binary images and calls VFmeasure.m to measure segmentation performance on images generated by the automated segmentation method (using SegmentCNN.m or using SegmentCNN2.m) and by the manual correction saved in BMP format.

VFmeasure.m

This m file computes relative overlap, misclassification rate, precision, true-positive, false-negative, true-negative and false-positive volume fraction measures to quantify the success of breast segmentation using binary images generated by the automated segmentation method and by the manual correction saved in BMP format. The details are given in Chapters 4-5.

GeneratenMITRmap.m

This m file generates 3D nMITR map of a specified volume of interest. To do this, it reads the image files and computes the relative enhancements of the tissues inside the supplied VOI data using a 3×3 moving window. The nMITR value of each tissue is computed by calling “computenMITR.m” file. The resultant map is saved into a mat file with “nMITRvoi” extension.

nMITRStatistics.m

This m file discriminates deceptively enhancing regions and segments the lesion in a 3D nMITR map (generated by GeneratenMITRmap.m) of a roughly marked volume of interest. After segmentation, it computes enhancement descriptors derived from nMITR values of the tissues inside the lesion for malignancy detection. The details are given in Chapter 6.

MorphoAnalyst.m

This m file discriminates deceptively enhancing regions and segments the lesion in a 3D nMITR map (generated by GeneratenMITRmap.m) of a roughly marked volume of interest. After segmentation, it computes morphological descriptors for malignancy detection. The details are given in Chapter 7.

SofSI.m

This m file is called by MorphoAnalyst.m to compute the total areas of contact surfaces and faces or the voxels of a binary 3D image of lesion volume considering the image resolutions.

APPENDIX B. DYNAMAMMOANALYST

The methods developed in this thesis were used to develop a decision support software to speed up DCE-MRM examinations. This software, called DynaMammoAnalyst, requires minimal user guidance, facilitates lesion identification, delineation and evaluation by providing improved visualization, segmentation and localization of suspiciously enhancing regions, interactive plots of time-intensity curves and time-intensity curve distributions and computation of several enhancement parameters. This software is explained in Chapter 8 in detail. A self-executable code of this software *DynaMammoAnalyst.exe* is given in the attached compact disk.

REFERENCES

1. McTiernan, A., M. Gilligan, and C. Redmond, "Assessing individual risk for breast cancer: Risky business," *J Clin Epidemiol*, Vol. 50, pp. 547-556, 1997.

2. Physician Data Query, Screening for breast cancer. Available: http://www.nci.nih.gov/cancerinfo/pdq/screening/breast/healthprofessional/

3. Kuhl, C.K., "The current status of breast MR imaging part I. Choice of technique, image interpretation, diagnostic accuracy and transfer to clinical practice," *Radiolog*y, Vol. 244, pp. 356-378, 2007.

4. Kelcz, F., E. Furman-Haran, D. Grobgeld, and H. Degani, "Clinical testing of high-spatial resolution parametric contras-enhanced MR imaging of the breast," *Am J Roentgenol*, Vol. 179, pp. 1485-1492, 2002.

5. Lehmann, C.D., S. Peacock, W.B. DeMartini, and X. Chen, "A new automated software system to evaluate breast MR examination: Improved specificity without decreased sensitivity," *Am J Roentgenol*, Vol. 187, pp. 51-56, 2006.

6. Parker, G.J.M., J. Suckling, S.F. Tanner, A.R. Padhani, J.E. Husband, and M.O. Leach, "MRIW: Parametric Analysis Software for Contrast-enhanced Dynamic MR Imaging in Cancer," *Radiographics*, Vol. 18, pp. 497-506, 1998.

7. Wiener, J., K.J. Schiling, C. Adami, and N.A. Obuchowski, "Assessment of Suspected Breast cancer by MRI: A prospective clinical trial using a combined kinetic and morphologic analysis," *Am J Roentgenol*, Vol. 184, pp. 878-886, 2005.

8. Zheng, B., Y.H. Chang, and D. Gur, "Computerized detection of masses in digitized mammograms using single-image segmentation and a multilayer topographic feature analysis," *Acad Radiol*, Vol. 2, pp. 959-966, 1995.

9. Sahiner, B., H. Chan, L.M. Hadjiiski, M.A. Helvie, C. Paramagul, J. Ge, J.Wei, and C. Zhou, "Joint two-view information for computerized detection of microcalcifications on mammograms," *Med Phys*, Vol. 33, pp. 2574-2585, 2006.

10. Drukker, K., M.L. Giger, K. Horsch, M.A. Kupinski, and C.J. Vyborny, "Computerized lesion detection on breast ultrasound," *Med Phys*, Vol. 29, pp. 1438-1446, 2002.

11. Reiser, I., R.M. Nishikawa, M.L. Giger, T. Wu, E. Rafferty, R.H. Moore, and D.B. Kopans, "Computerized mass detection for digital breast tomosynthesis directly from the projection images," *Med Phys*, Vol. 33, pp. 482-491, 2006.

12. Nelson, T., J. Boone, J. Seibert, B. Kuhn, A. Kwan, and K. Yang, "Visualization and identification of breast glandular tissue in breast CT volume data," *Med Phys*, Vol. 32, pp. 1897-1898, 2005.

13. Bian, J., W. Chen, G. Newstead, and M. Giger, "Computerized lesion detection on breast MR images," *Med Phys*, Vol. 33, pp. 2195, 2006.

14. Morris, E., and L. Liberman, *Breast MRI Diagnosis and intervention*, Springer, 2005.

15. Nunes, L.W., M.D. Schnall, and S.G. Orel, "Update of breast MR imaging architectural interpretation model," *Radiology*, Vol. 219, pp. 484-494, 2001.

16. Szabo, B.K., M.K. Wilberg, B. Bone, and P. Aspelin, "Application of artificial neural networks to the analysis of dynamic MR imaging features of the breast," *Eur Radiol*, Vol. 14, pp. 1217-1225, 2004.

17. Wedegartner, U., U. Bick, K. Wortler, E. Rummeny, and G. Bongartz, "Differentiation between benign and malignant findings on MR-mammography: usefulness of morphological criteria," *Eur Radiol*, Vol. 11, pp. 1645–1650, 2001.

18. Shahar, K.H., M. Solaiyappan, and D.A. Bluemke, "Quantitative differentiation of breast lesions based on three-dimensional morphology from magnetic resonance imaging," *J Comput Assist Tomogr*, Vol. 26, pp. 1047-1053, 2002.

19. Gilhuijs, K.G.A., E.E. Deurloo, S.H. Muller, J.L. Peterse, and L.J.S Kool, "Breast MR Imaging in women at increased lifetime risk of breast cancer: clinical system for computerized assessment of breast lesions-initial results," *Radiology*, Vol. 225, pp. 907-916, 2002.

20. Tzacheva, A.A., K. Najarian, and J.P. Breockway, "Breast cancer detection in gadolinium-enhanced MR images by static region descriptors and neural networks," *J Magn Reson Imaging*, Vol. 17, pp. 337-342, 2003.

21. Liney, G.P., M. Sreenivas, P. Gibbs, R. Garcia-Alvarez, and L.W. Turnbull, "Breast lesion analysis of shape technique: semiautomated vs. manual morphological description," *J Magn Reson Imaging*, Vol. 23, pp. 493-498, 2006.

22. Kuhl, C.K., P. Mielcareck, S. Klaschik S, C. Leutner, E. Waldermanm, J. Gieseke, and H.H. Schild, "Dynamic breast MR imaging: Are signal time course data useful for differential diagnosis of enhancing lesion?," *Radiology,* Vol. 211, pp. 101-110, 1999.

23. Kinkel, K., T.H. Helbich, L.J. Essermam, et al. "Dynamic high-spatial-resolution MR imaging of suspicious breast lesions: Diagnostic criteria and interobserver variability," *Am J Roentgenol*, Vol. 175, pp. 35-43, 2000.

24. Baum, F, U. Fischer, R. Vosshenrich, and E. Grabbe, "Classification of hypervascularized lesions in CE MR imaging of the breast," *Eur Radiol*, Vol. 12, pp. 1087-1092, 2002.

25. Kelcz, F., G.E. Santyr, G.O. Cron, and SJ Mongin, "Application of a quantitative model to differentiate benign from malignant breast lesions detected by dynamic, gadolinium-enhanced MRI," *J Magn Reson Imaging*, Vol. 6, pp. 743-752, 1996.

26. Mussurakis, S., D.L. Buckley, and A. Horsman, "Dynamic MRI of invasive breast cancer: Assessment of three region-of-interest analysis methods," *J Comput Assist Tomogr*, Vol. 21, pp. 431-438, 1997.

27. Liu, P.F., J.F. Debatin, R.F. Caduff, G. Kacl, E. Gazoli, and G.P. Krestin, "Improved diagnostic accuracy in dynamic contrast enhanced MRI of the breast by combined quantitative and qualitative analysis," *Br J Radiol*, Vol. 71, pp. 501-509, 1998.

28. Helbich, T.H., T.P. Roberts, A. Grossmann, M.F. Wendland et al. "Quantitative gadopentetate-enhanced MRI of breast tumors: Testing of different analytic methods," *Magn Reson Med*, Vol. 44, pp. 915-924, 2000.

29. Lucht, R.E.A., M.V. Knopp, and G. Brix, "Classification of signal-time curves from dynamic MR mammography by neural networks," *Magn Reson Imaging*, Vol. 19, pp. 51-57, 2001.

30. Chen, W., M.L. Giger, L. Lan, and U. Bick, "Computerized interpretation of breast MRI: Investigation of enhancement-variance dynamics," *Med. Phys*, Vol. 31, pp. 1076–1082, 2004.

31. Flickenger ,F.W., J.F. Allison, R.M. Sherry, and J.C. Wright, "Differentiation of benign from malignant breast masses by time intensity evaluation of contrastenhanced MRI," *Magn Reson Imaging*, Vol. 11, pp. 617-620, 1993.

32. Liney, G.P., P. Gibbs, C. Hayes, M.O. Leach and L.W. Turnbull, "Dynamic contrast-enhanced MRI in the differentiation of breast tumors: user-defined versus semi-automated region-of-interest analysis," *J Magn Reson Imaging*, Vol. 10, pp. 945-949, 1999.

33. Gibbs, P., and L.W. Turnbull, "Textural analysis of contrast-enhanced MR images of the breast," *Magn Reson Med*, Vol. 50, pp. 92-98, 2003.

34. Gibbs, P., G.P. Liney, M. Lowry, P.J. Kneeshaw, and L.W. Turnbull, "Differentiation of benign and malignant sub-1 cm breast lesions using dynamic contrast enhanced MRI," *The Breast*, Vol. 12, pp. 115-121, 2004.

35. Kneeshaw, P.J., M. Lowry, D. Manton, A. Hubbard, P.J. Drew, and L.W. Turnbull, "Differentiation of benign from malignant breast disease associated with screening detected microcalcifications using dynamic contrast enhanced magnetic resonance imaging," *The Breast*, Vol. 15, pp. 29-38, 2006.

36. Subramanian, K.R., J.P. Brockway, and W.B. Carruthers, "Interactive detection and visualization of breast lesions from dynamic contrast enhanced breast MRI volumes," *Comput Med Imaging Graph*, Vol. 28, pp. 435-444, 2004.

37. Breast Anatomy. Available: http://training.seer.cancer.gov/ss_module01_breast/unit02_sec01_anatomy.html

38. Tavassoli F.A., *Pathology of the breast*, Appleton & Lange, Connecticut, 1992.

39. Hughes, L.E., "Classification of benign breast disorders: The ANDI classification based on physiological processes within the normal breast," *Br Med Bulletin*, Vol. 47, pp. 251-257, 1991.

40. Benign Breast Diseases. Available: http://www.tennesseebreastcenter.com/

41. Rosen, P.P., and H.A. Oberman, "Tumors of the Mammary Gland. Atlas of Tumor Pathology", 3rd Series, Fascicle 7, Armed Forces Institute of Pathology, Washington, D.C., 1993.

42. Tabar, L., B. Vitak, H.H. Chen, M.F. Yen, S.W. Duffy, and R.A. Smith, "Beyond randomized controlled trials: organized mammographic screening substantially reduces breast carcinoma mortality," *Cancer*, Vol. 91, pp. 1724-1731, 2001.

43. Morimoto, T., M. Sasa, T. Yamaguchi, H. Kondo, H. Akaiwa, and Y. Sagara, "Breast cancer screening by mammography in women aged under 50 years in Japan," *Anticancer Res*, Vol. 20, pp. 3689-3694., 2000.

44. Miller, A.B., "The role of screening in the fight against breast cancer," *World Health Forum*, Vol. 13, pp. 277-285, 1992.

45. Kopans, D.B., “The positive predictive value of mammography,” *Am J Roentgenol*, Vol. 158, pp. 521-526, 1992.

46. Huyn, P.T., A.M. Jarolinek, and S. Daye, “The false-negative mammogram,” *Radiographics*, Vol. 18, pp. 1137-1154, 1998.

47. Rahbar, G., A.C. Sie, G.C. Hansen, J.S. Prince, and M.L. Melany, “Benign versus malignant solid breast masses: US Differentiation,” *Eur Radiol*, Vol. 213, pp. 889-894, 1999.

48. Khalkhali, I., I. Mena I, and L. Diggles, “Review of imaging techniques for the diagnosis of breast cancer: a new role of prone scintimammography using technetium-99m sestamibi,” *Eur J Nucl Med*, Vol. 21, pp. 357-362, 1994.

49. Schirrmeister, H., T. Kuhn, A. Guhlmann, C. Santjohanser, T. Horster, K. Nussle et al., “Fluorine-18 2-deoxy-2-fluoro-D-glucose PET in the preoperative staging of breast cancer: comparison with the standard staging procedures,” *Eur J Nucl Med.*, Vol. 28, pp. 351-358, 2001.

50. Martin, G., R. Martin, M.J. Brieva, and L. Santamaria, “Electrical impedance scanning in breast cancer imaging: correlation with mammographic and histologic diagnosis,” *Eur Radiol*, Vol. 12, pp. 1471-1478, 2002.

51. Wersebe, A., K. Siegmann K, U. Krainick, N. Fersis, U. Vogel, C.D. Claussen, and M. Müller-Schimpfle, “Diagnostic potential of targeted electrical impedance scanning in classifying suspicious breast lesions,” *Invest Radiol*, Vol. 37, pp. 65-72, 2002.

52. Orel, S.G., and M. Schnall, “MR imaging of the breast for the detection, diagnosis and staging of breast cancer,” *Radiology*, Vol. 220, pp. 13-30, 2001.

53. Merchant, T.E., G.R: Thelissen, P.W. deGraaf, C.W. Nieuwenhuizen, H.C. Kievit, and W. Den Otter, “Application of a mixed imaging sequence for MR imaging characterization of human breast disease,” *Acta Radiologica*, Vol. 34, pp. 356-361, 1993.

54. Kaiser, W.A., and E. Zeitker, “MR imaging of the breast: Fast imaging sequences with and without Gd–DTPA (preliminary observations),” *Radiology*, Vol. 170, pp. 681-687, 1989.

55. Turkat, T.J., B.D.Klein, R.L. Polan, and R.H. Richman, “Dynamic MR Mammography: a technique for potentially reducing the biopsy rate for benign breast disease,” *J Magn Reson Imaging*, Vol. 4, pp. 563–568, 1994.

56. Heywang, S.H., D. Hahn, H. Schmidt, I. Krischke, W. Eiermann, R. Bassermann, and J. Lissner, “MR imaging of the breast using Gd-DTPA,” *J Comput Assist Tomogr*, Vol. 10, pp. 615-620, 1986.

57. Heywang, S.H., R. Bassermann, G. Fenzl, W. Nathat, D. Hahn, R. Beck, I. Krischke, and W. Eiermann, “MRI of the breast: histopathologic correlation,” *Eur J Radiol*, Vol. 7, pp. 175-182, 1987.

58. Heywang, S.H., A. Wolf, E. Pruss, T. Hilbertz, W. Eiermann, W. Permanetter, “MR imaging of the breast with Gd–DTPA: use and limitations,” *Radiology*, Vol. 171, pp. 95-103, 1989.

59. Weinreb, J.C., and G. Newstead, “MR imaging of the breast,” *Radiology*, Vol. 196, pp. 593-610, 1995.

60. Davis, P.L., and K.S. McCarty, "Sensitivity of enhanced MRI for detection of breast cancer: new, multicentric, residual and recurrent," *Eur Radiol*, Vol. 7, pp. 289-298, 1997.

61. Morris, E.A., "Breast cancer imaging with MRI," *Radiol Clin North America*, Vol. 40, pp. 443- 466, 2002.

62. Fisher, U., and U. Brinck, *Practical MR Mammography*, Thieme, 2004.

63. Orel, S.G., M. Schnall, V.A. LiVolsi, and R.H. Troupin, "Suspicious breast lesions: MR imaging with radiologic-pathologic correlation," *Radiology*, Vol. 190, pp. 485-93, 1994.

64. Heywang, S.H., D. Dershaw, and I. Schree, *Diagnostic Breast Imaging: Mammography, Sonography, Magnetic Resonance Imaging and Interventional Procedures*, Thieme Stutgart, New York, 1997.

65. Ercolani, P., G. Valeri, and F. Amici, "Dynamic MRI of Breast," *Radiology*, Vol. 27, pp. 265-271, 1998.

66. Konyer, N.B., E.A. Ramsay, M.J. Bronskill, and D.B. Plewes, "Comparison of MR imaging breast coils," *Radiology*, Vol. 222, pp. 830-834, 2002.

67. CP Breast Array Coil. Available: http://www.medical.siemens.com/

68. Rubens, D., S. Totterman, and A.K. Chacko, "Gadopentatate dimeglumine-enhanced chemical-shift MR imaging of the breast," *Am J Roentgenol*, Vol. 157, pp. 267-70, 1991.

69. Kenney, P.J., W.T. Sobol, J.K. Smith, and D.E. Morgan, "Computed model of gadolinium enhanced MRI of breast disease," *Eur J Radiol*, Vol. 24, pp. 109-119, 1997.

70. Koenig, S.H., C. Baglin C, and R.D. Brown, "Magnetic field dependences of solvent proton relaxation induced by Gd 3+ and Mn 2+ complexes," *Mag Reson Med*, Vol. 1, pp. 496, 1984.

71. Bottomley, P.A., C.J. Hardy, R.E. Arsersindeg, and G. Allen-Moore, "A review of 1H NMR relaxation in pathology: Are T1 and T2 diagnostic?," *Med Phys*, Vol. 14, pp. 1-37, 1987.

72. Piccoli, C.W., "Contrast enhanced breast MRI: factors affecting sensitivity and specificity," *Eur Radiol*, Vol. 7, pp. 281-289, 1997.

73. Hendrick, R.E., "Breast MRI: Using physics to maximize its sensitivity and specificity to breast cancer," *Handouts of the 46th AAPM Annual Meeting*, 1994.

74. Coulthard, A., and A.J. Potterton, "Pitfalls of breast MRI", *British J Radiol*, Vol. 72, pp. 665-671, 2003.

75. Siegmann, K.C., M. Muller-Schimpfle, F. Schick, C.T. Remy, N. Fersi, C. Gorriz, and C.D. Claussen, "MR imaging-detected breast lesions: histopathologic correlation of lesion characteristics and signal intensity data," *Am J Roentgenol*, Vol. 178, pp. 1403-1409, 2002.

76. Leach, O.M., "Application of magnetic resonance imaging to angiogenesis in breast cancer," *Breast Cancer Res*, Vol. 3, pp. 22-27, 2001.

77. Frouge C., J.M. Guinebretiere, G. Contesso, R.D. Paola, and M. Blery, "Correlation between contrast enhancement in dynamic magnetic resonance imaging of breast and tumor angiogenesis," *Invest Radiol*, Vol. 29, pp. 1043-1052, 1994.

78. Degani, H., V. Gusis, D. Weinstein, S. Fields, and S. Strano, "Mapping pathophysiological features of breast tumors by MRI at high spatial resolution," *Nat Med*, Vol. 3, pp. 780-782, 1997.

79. Tuncbilek, N., E. Unlu, H.M. Karakas, B. Cakir, and F. Ozyilmaz, "Evaluation of tumor angiogenesis with contrast-enhanced MR Mammography," *Breast Journal*, Vol. 9, pp. 403-4011, 2003.

80. Ichikawa, T, K. Ohtomo, G. Uchiyama, H. Fujimoto, and K. Nasu, "Contrast-Enhanced dynamic MR of adrenal masses: classification of characteristic enhancement patterns," *Clinical Radiology*, Vol. 50, pp. 295-300, 1995.

81. Lee, C.H., "Problem solving MR imaging of the breast," *Radiol Clin N Am*, Vol. 42, pp. 919, 2004.

82. Kuhl, C.K., H.H. Schild, and N. Morakkabati, "Dynamic bilateral contrast-enhanced MR imaging of the breast: Trade–off between spatial and temporal resolution," *Radiology*, Vol. 236, pp. 789, 2005.

83. Kuhl, C.K., H.G. Bieling, G. Lutterbey, T. Sommer, E. Keller, and H.H. Schild, "Standardization and acceleration of quantitative analysis of dynamic MR mammographies via parametric images and automatized ROI definition," Rofo, Vol. 164, pp. 475-482, 1996.

84. Deurloo, E.E., S.H. Muller, J.L. Peterse, A.P.E. Bernard, and K.G.A. Gilhuijs, "Clinically and Mammographically occult breast lesion on MR images: Potential effect of computerized assessment on clinical reading," *Radiology*, Vol. 234, pp. 693-701, 2005.

85. Chen, W., L.G. Maryellen, and B. Ulrich, "A fuzzy c-means (FCM)-based approach for computerized segmentation of breast lesions in dynamic contrast-enhanced MR images," *Acad Radiol*, Vol. 13, pp. 63-72, 2006.

86. Hayton, P., M. Brady, Tarassenko and N. Moore, "Analysis of dynamic MR breast images using a model of contrast enhancement," *Medical Imag Anal*, Vol. 3, pp. 207-224, 1997.

87. Twellmann, T., O. Lichte, and T.W. Nattkemper, "An adaptive tissue characterization network for model-free visualization of dynamic contrast-enhanced magnetic resonance image data," *IEEE Trans Med Imaging*, Vol. 24, pp. 1256-1266, 2005.

88. Yang, L., T. Yang, K.R. Crounse, and L.O. Chua, "Implementation of binary mathematical morphology using discrete-time cellular neural networks," *Proceedings of the IEEE International Workshop on CNNs and Their Applications*, pp. 7, 1996.

89. Brugge, M.H., R.J. Krol, J.A.G. Nijhuis, and L. Spaanemburg, "Design of discrete-time cellular neural networks based on mathematical morphology," *Proceedings of the IEEE International Workshop on CNNs and Their Applications*, pp. 1, 1996.

90. Harrer, H., J.A. Nossek, and R. Stelzl, "An analog implementation of discrete-time CNNs," *IEEE Trans Neural Networks*, Vol. 3, pp. 466-476, 1992.

91. Rekeczky, C., A. Tahy, V. Zoltan, and T. Roska, "CNN-based spatio-temporal nonlinear filtering and endocardial boundary detection in echocardiography," *Int J Circ Theor Appl*, Vol. 27, pp. 171, 1999.

92. Zarandy, A., F. Werblin, T. Roska and L.O. Chua, “Novel types of analogic CNN algorithms for recognizing bank-notes,” *Proceedings of the IEEE International Workshop on CNNs and Their Applications*, pp. 273, 1994.

93. Girodana, D., R. Leonardi, F. Maiorana, G. Critaldi, and M.L. Distefano, “Automatic landmarking of cephalograms by cellular neural networks,” in *Artificial Intelligence in Medicine*, p. 333. Springer Berlin, 2005.

94. Shitong, W., and W. Min, “A new detection algorithm (NDA) based on fuzzy cellular neural networks for white blood cell detection,” *IEEE Trans Inf Technol Biomed*, Vol. 10, pp. 5-10, 2006.

95. Aizenberg, I., N. Aizenberg, J. Hiltner, C. Moraga, and E. Meyer zu Bexten, “Cellular neural networks and computational intelligence in medical image processing,” *Image Vis Comput*, Vol. 19, pp. 177-183, 2001.

96. Zarandy, A., “The art of CNN template design”, *Int J Circ Theor Appl*, Vol. 27, pp. 5-23, 1999.

97. Chua, L.O., *Cellular neural Networks and Visual Computing: Foundation and Primer*, Cambridge University Press, 2001.

98. Zarandy, A., T. Roska, G. Liszka, H. Hegyesi, L. Kek, and C. Rekeczky, “Design of analogic CNN algorithm for mammogram analysis,” *Proceedings of the IEEE International Workshop on CNNs and Their Applications,* pp. 18, 1994.

99. Song, T., C. Gasparovic, N. Anderasen, J. Bockholt, M. Jamshidi, RR. Lee, and M. Huang, “A hybrid tissue segmentation approach for brain MR images,” *Med Biol Eng Comput*, Vol. 44, pp. 242-249, 2006.

100. Udupa, J.K., V.R. LeBlanc, Y. Zhuge, C. Imirlinska, H. Schmidt, L.M. Currie, B.E. Hirsch, and J. Woodburn, “A framework for evaluating image segmentation algorithms,” *Comput Med Imag Grap.*, Vol. 30, pp. 75-87, 2006.

101. Bovik, C.A., *Handbook of Image and Video Processing*, Elsevier Science & Technology Books, 2005.

102. Rueckert, D., L. Sonoda, C. Hayes, D.L. Hill, M.O. Leach, and D.J. Hawkes, “Nonrigid registration using free-form deformations: application to breast MR images,” *IEEE Trans Med Imaging,* Vol. 18, pp. 712-721, 1999.

103. Reichenbach, J.R., J. Hopfe, M.E. Bellemann, and W.A. Kaiser, “Development and validation of an slgorithm for registration of serial 3D MR breast data sets,” *Magn Reson Mater Phy*, Vol. 14, pp. 249-257, 2002.

104. Rohlfing, T., C.R. Maurer, D.A. Bluemke, and M.A. Jacobs, “Volume-preserving nonrigid registration of MR breast images using free-form deformation with an incompressibility constraint,” *IEEE Trans Med Imaging*, Vol. 22, pp. 730-741, 2003.

105. Sivaramakrishna, R., “3D breast image registration-a review”, *Technol Cancer Res Treat*, Vol. 4, pp. 39-48, 2005.

106. Pavic, D., M.A. Koomen, C.M. Kuzmiak, Y.H. Lee, and E.D. Pisano, “The role of magnetic resonance imaging in diagnosis and management of breast cancer,” *Technol Cancer Res Treat*, Vol. 3, pp. 527-541, 2004.

107. Kuhl, C.K. and H.H. Schild, “Dynamic image interpretation of MRI of the breast,” *J Magn Reson Imaging*, Vol. 12, pp. 965-974, 2000.

108. Chua, L.O., and L. Yang, “Cellular neural networks: Theory,” *IEEE Trans Circuits Syst*, Vol. 32, pp. 1257-1272, 1988.

109. Crounse, K.R., and L.O. Chua, “Methods for image processing and pattern formation in cellular neural networks: a tutorial,” *IEEE T Circuits-I*, Vol. 42, pp. 583-601, 1995.

110. Brugge, M.H., *Morphological design of discrete-time cellular neural networks*, PhD Thesis, University of Groningen, Groningen, Nederlands, 2005.

111. Zhang, X., G. McLennan, E.A. Hoffman, and M. Sonka, “Automated detection of small-size pulmonary nodules based on helical CT images,” in *Information Processing in Medical Imaging*, pp. 664-676, Springer Berlin, 2005.

112. Zarandy, A., A. Stoffels, T. Roska, and L.O. Chua, “Morphological Operators on the CNN Universal Machine,” *Proceedings of the IEEE International Workshop on CNNs and Their Applications*, pp. 151, 1996.

113. Wenzhu, L., Y. Jianhua, L. Chao, S. Prindiville, and C. Chow, “DCE-MRI segmentation and motion correction based on active contour model and forward mapping,” *Proceedings of the 7th ACIS International Conference on Software Engineering, Artificial Intelligence, Networking, and Parallel/Distributed Computing*, pp. 208, 2006.

114. Cheng, H.D., J.R. Chen, and J. Li, “Threshold selection based on fuzzy c-partition entropy approach,” *Pattern Recogn*, Vol. 31, pp. 857-870, 1998.

115. Mamistvalov, A.G., “n-dimensional moment invariants and conceptual mathematical theory of recognition n-dimensional solids,” *IEEE T Pattern Anal*, Vol. 20, pp. 819-831, 1998.

116. Ertas, G., H.O. Gulcur, and M. Tunaci, “Improved lesion detection in MR mammography: Three-dimensional segmentation, moving voxel sampling, and normalized maximum intensity–time ratio entropy,” *Acad Radiol*, Vol. 14, pp. 151-161, 2007.

117. Obuchowski, N., “Receiver operating characteristic curves and their use in radiology,” *Radiology*, Vol. 229, pp. 3-8, 2003.

118. Goo, J.M., J.W. Lee, H.J. Lee, S. Kim, J.H. Kim, and J.G. Im, “Automated lung nodule detection at low-dose CT: Preliminary Experience,” *Korean Journal of Radiology*, Vol. 4, pp. 211-216, 2003.

119. Bribiesca, E., “A measure of compactness for 3D shapes,” *Computers & Mathematics with Applications*, Vol. 40, pp. 1275-1284, 2000.

120. Greiner, M., D. Pfeiffer, and R.D. Smith, “Principals and practical application of the receiver operating characteristic analysis for diagnostic tests,” *Preventive Veterinary Medicine*, Vol. 45, pp. 23-41, 2000.

121. Orel, S.G., “Differentiating Benign from malignant enhancing lesions identified at MR imaging of the breast: Are time-signal intensity curves an accurate predictor,” *Radiology*, Vol. 211, pp. 5-7, 1999.

122. Snow, R.D., Dyess D.L., Harpen M.D., Kreisberg C.N., Tucker J.A., “Dynamic magnetic resonance imaging in evaluating suspicious breast lesions: Correlation with pathologic findings,” *Southern Medical Journal*, Vol. 91, pp. 527-531, 1998.

123. Tuncbilek, N., H.M. Karakas, and O. Okten, “Dynamic magnetic resonance imaging in determining histopathological prognostic factors of invasive breast cancers,” *Eur J Radiol*, Vol. 53, pp. 199-205, 2005.

124. Ertas, G., H.O. Gulcur, O. Osman, O.N. Ucan, M. Tunacı, and M. Dursun, “Breast MR segmentation and lesion detection with cellular neural networks and 3D template matching,” *Comput Med Biol*, doi: 10.1016/j.compbiomed.2007.08.001, 2007.

VITA

Gökhan ERTAŞ was born in Istanbul in 1976. He received B.S. degree from Erciyes University in Electronic Engineering in 1998. He started M.S. studies at the Biomedical Engineering Institute of Bogazici University, Istanbul, in 1998 and completed M.S. thesis on "Feature Extraction from Mamographic Mass Shapes and Development of a Mammogram Database" in 2001. He started Ph.D studies in the same year at the same institute of Bogazici University.

He is a member of Institute of Electrical and Electronics Engineers and Engineering in Medicine and Biology Society (IEEE-EMBS), European Society for Magnetic Resonance in Medicine and Biology (ESMRMB) and Turkish Society of Magnetic Resonance. His interest areas include the development of new methods for computerized detection and diagnosis of breast MR lesions.

A list of publications that came out of the dissertation work is presented below.

In international journals

1. Ertas, G., H.Ö. Gülçür, and M. Tunacı, "An interactive dynamic analysis and decision support software for MR mammography," *Comput Med Imag Graph 2007*, submitted.
2. Ertas, G., H.Ö. Gülçür, and M. Tunacı, "Normalized maximum intensity time ratio maps and morphological descriptors for assessment of malignancy in MR Mammography," *Med Phys 2007*, accepted.
3. Ertas, G., H.Ö. Gülçür, M. Tunacı, and O. Osman, "Computerized Lesion Localization in MR Mammography: 3D nMITR Maps, Multilayer Cellular Neural Networks and Fuzzy c-Partitioning," *Med Phys 2007*, in press.
4. Ertas, G., H.Ö. Gülçür, M. Tunacı, O.N. Ucan, O. Osman, and M. Dursun, "Breast MR segmentation and lesion detection with cellular neural networks and 3D template matching," *Comput Biol Med 2007*, in press.
5. Ertas, G., H.Ö. Gülçür, M. Tunacı, "Improved lesion detection in MR Mammography: three-dimensional segmentation, moving voxel sampling, and normalized maximum intensity–time ratio entropy," *Acad Radiol 2007*, 14:151-161.

6. Ertas, G., H.Ö. Gülçür, M. Tunacı, and M. Dursun, “Performance comparison of quantitative circularity features of lesions detected in breast MR images,” *Proceedings of the 23rd Annual Meeting of ESMRMB*, Warsaw, Poland, 2006. (published as a special issue of *Magn Reson Mater Phy,* Vol.19, pp. 317, 2006).

7. Ertas, G., H.Ö. Gülçür, M. Tunacı, and M. Dursun, “k-means based segmentation of breast region on MR mammograms,” *Proceedings of the 23rd Annual Meeting of ESMRMB*, Warsaw, Poland, 2006.(published as a special issue of *Magn Reson Mater Phy 2006,* , Vol.19, pp. 317, 2006).

8. Ertas, G., M. Ozkan, and H.Ö. Gülçür, “Parametric mapping of dynamic breast MR images using contrast enhancement curves,” *Proceedings of the European Congress of Radiology,* Vienna, Austria, 2004. (published as a special issue of *Eur Radiol,* Supplement 2, Vol. 14, pp. 285, 2004).

9. Ertas, G., M. Dursun, M. Tunacı, H.Ö. Gülçür, and C. Öztürk, “En fazla yoğunluk zaman oranı görüntüsüyle MR mammogramlardaki tümörlerin bilgisayarla ayrıştırılması,” *Proceedings of the Türk Radyoloji Derneği 25. Ulusal Radyoloji Kongresi*, Antalya, Turkey, 2004. (published as a special issue of *Tanısal ve Girişimsel Radyoloji Dergisi,* Vol. 10, pp. 64, 2004).

In international proceedings

1. Ertas, G., H.Ö. Gülçür, M. Tunacı, and M. Dursun, “DynaMammoAnalyst: Simultaneous dynamic and morphologic analysis software for MR mammography,” *Proceedings of the ISMRM-ESMRMB Joint Annual Meeting,* Berlin, Germany, 2007.

2. Ertas, G., H.Ö. Gülçür, M. Tunacı, and M. Dursun, “Extraction of lesion features from contrast-enhanced MR mammograms using initial and post-initial enhancements,” *Proceedings of the ISMRM-ESMRMB Joint Annual Meeting*, Berlin, Germany, 2007.

3. Kaleli F., N Aydın, G. Ertas, and H.Ö. Gülçür, “An adaptive approach to the segmentation of DCE-MR images of the breast: comparison with classical thresholding algorithms,” *Proceedings of the IEEE Symposium on Computational Intelligence in Image and Signal Processing*, Hawaii, USA, 2007.

4. Ertas, G., M. Ozkan, and H.Ö. Gülçür, “Modeling Signal-Intensity Time Data in Contrast Enhanced Dynamic Breast MRI,” *Proceedings of the ISIK2003 Workshop on New Challenges in Biomedical Engineering*, Istanbul, Turkey, 2003.

In national proceedings

1. Ertas, G., M. Dursun, H.O. Gulcur, and M. Tunaci, “Detection of polluted enhancement curves in dynamic breast MR imaging using pharmacokinetic modeling,”

Proceedings of the BIYOMUT2006 Biyomedikal Mühendisliği Ulusal Toplantısı, Istanbul, Turkey, 2006.

2. Ertas, G., O. Osman, M. Dursun, H.O. Gulcur, M. Tunaci, and O. N. Uçan, "Cellular neural network based segmentation of breast region on MR images," *Proceedings of the BIYOMUT2006 Biyomedikal Mühendisliği Ulusal Toplantısı*, Istanbul, Turkey, 2006.

3. Ertas, G., H.O. Gulcur, O.S. Dogruluk, M. Dursun, and M. Tunaci, "Correction of intensity variations on breast MR images using spatial filtering," *Proceedings of the BIYOMUT2006 Biyomedikal Mühendisliği Ulusal Toplantısı*, Istanbul, Turkey, 2006.

4. Ertas, G., and H.O. Gulcur, "Success of histogram based methods in segmentation of T1-weighted breast MR images," *Proceedings of the BIYOMUT2005 Biyomedikal Mühendisliği Ulusal Toplantısı*, Istanbul, Turkey, 2005.

5. Ertas, G., M. Dursun, H.O. Gulcur, and M. Tunaci, "Quantitative evaluation of breast MR masses using maximum intensity-time ratio projections," *Proceedings of the BIYOMUT2005 Biyomedikal Mühendisliği Ulusal Toplantısı*, Istanbul, Turkey, 2005.

6. Dogruluk, O.S., G. Ertas, and H.O. Gulcur, "Detection of dominant inhomogeneity regions in breast MR imaging," *Proceedings of the BIYOMUT2005 Biyomedikal Mühendisliği Ulusal Toplantısı*, Istanbul, Turkey, 2005.

7. Ertas, G., M. Dursun, M. Tunaci, and H.O. Gulcur, "Computerized analysis of contrast enhanced MR mammograms and maximum intensity-time ratio modulated image formation," *Proceedings of the BIYOMUT2004 Biyomedikal Mühendisliği Ulusal Toplantısı*, Istanbul, Turkey, 2004.